

A Reexamination of Phosphorus and Chlorine Depletions in the Diffuse Interstellar Medium*

ADAM M. RITCHEY,¹ J. M. BROWN,² S. R. FEDERMAN,² AND PAULE SONNENTRUCKER³

¹*Eureka Scientific, 2452 Delmer Street, Suite 100, Oakland, CA 96402, USA*

²*Department of Physics and Astronomy, University of Toledo, Toledo, OH 43606, USA*

³*European Space Agency Office, Space Telescope Science Institute, 3700 San Martin Dr., Baltimore, MD 21218, USA*

ABSTRACT

We present a comprehensive examination of interstellar P and Cl abundances based on an analysis of archival spectra acquired with the Space Telescope Imaging Spectrograph of the Hubble Space Telescope and the Far Ultraviolet Spectroscopic Explorer. Column densities of P II, Cl I, and Cl II are determined for a combined sample of 107 sight lines probing diffuse atomic and molecular gas in the local Galactic interstellar medium (ISM). We reevaluate the nearly linear relationship between the column densities of Cl I and H₂, which arises from the rapid conversion of Cl⁺ to Cl⁰ in regions where H₂ is abundant. Using the observed total gas-phase P and Cl abundances, we derive depletion parameters for these elements, adopting the methodology of Jenkins. We find that both P and Cl are essentially undepleted along sight lines showing the lowest overall depletions. Increasingly severe depletions of P are seen along molecule-rich sight lines. In contrast, gas-phase Cl abundances show no systematic variation with molecular hydrogen fraction. However, enhanced Cl (and P) depletion rates are found for a subset of sight lines showing elevated levels of Cl ionization. An analysis of neutral chlorine fractions yields estimates for the amount of atomic hydrogen associated with the H₂-bearing gas in each direction. These results indicate that the molecular fraction in the H₂-bearing gas is at least 10% for all sight lines with $\log N(\text{H}_2) \gtrsim 18$ and that the gas is essentially fully molecular at $\log N(\text{H}_2) \approx 21$.

Keywords: interstellar medium — interstellar abundances — diffuse interstellar clouds — interstellar dust

1. INTRODUCTION

Dust plays an important role in the evolution of galaxies due to the impact it has on the physics and chemistry of the interstellar medium (ISM). However, questions remain regarding the dominant dust production mechanisms, both in the present day Milky Way and in galaxies at high redshift. Efficient dust production occurs in the extended outer atmospheres of evolved stars (e.g., [Gobrecht et al. 2016](#)) and in the cooling ejecta of supernovae (SNe; e.g., [Sarangi & Cherchneff 2015](#)).

However, the timescale for dust production by stars is longer than the timescale for destruction of the grains by SN shocks ([Dwek & Scalzo 1980](#); [Jones et al. 1994](#); [Slavin et al. 2015](#)). Moreover, the large observed depletions of refractory elements in cold, diffuse clouds (where $\sim 95\%$ of the Mg and Si atoms and $\sim 99\%$ of the Fe atoms are locked up in grains; e.g., [Jenkins 2009](#)) are inconsistent with the levels of condensation expected for material returned to the ISM by evolved stars and SNe (e.g., [Dwek 2016](#)). These considerations have generally been interpreted as indications that dust grains must grow through the accretion of refractory elements in cold diffuse interstellar clouds.

Direct constraints on the growth of dust grains in the diffuse ISM come from detailed knowledge of the depletions of different elements from the gas-phase and how those depletions change with changing environmental conditions. [Jenkins \(2009\)](#) compiled information on interstellar depletions for 17 elements along 243 sight lines

Corresponding author: Adam M. Ritchey
ritchey.astro@gmail.com

* Based on observations made with the NASA/ESA *Hubble Space Telescope* and the *Far Ultraviolet Spectroscopic Explorer* mission, obtained from the MAST data archive at the Space Telescope Science Institute. STScI is operated by the Association of Universities for Research in Astronomy, Inc., under NASA contract NAS5-26555.

sampling diffuse atomic and molecular gas in the solar vicinity. [Jenkins \(2009\)](#) developed a unified framework for examining gas-phase element depletions predicated on the empirical observation that, while different elements exhibit different degrees of depletion, the depletions of most elements tend to increase in a systematic way as the overall strength of depletions increases from one sight line to the next. [Ritchey et al. \(2018\)](#) extended that framework to include several rare neutron-capture elements (and the light element B) yielding a more complete picture of gas-phase depletions for elements with low-to-moderate condensation temperatures.

To quantify the overall strength of the depletions seen in a given direction, [Jenkins \(2009\)](#) defined the sight line depletion strength factor F_* . Sight lines showing strong depletions (such as those that characterize relatively dense and/or cold H_2 -rich gas in the Galactic disk where grain growth occurs via cold accretion) have depletion factors near $F_* = 1$, while sight lines showing only very modest depletions (characteristic of warm and/or low-density H_2 -poor gas where substantial grain growth has not yet occurred or where the grains have been destroyed or disrupted by shocks) have values of F_* closer to zero. The observed depletions at $F_* = 0$ are probably the best representation that we have of the composition of grain cores that emerge from evolved low and high-mass stars and core-collapse SNe.

Most elements with low-to-moderate condensation temperatures ($T_C \lesssim 800$ K) have depletions at $F_* = 0$ that are consistent with zero (see Figure 21 in [Ritchey et al. 2018](#)). For elements with higher condensation temperatures, a fairly well-defined trend emerges of increasing depletion with increasing T_C , particularly for Ga, Ge, Cu, Mn, Cr, Fe, Ni, and Ti. [Ritchey et al. \(2018\)](#) suggest that this trend constitutes a dust condensation sequence and that the temperature where the sequence seems to terminate (~ 800 K) is related to the dust formation temperature. This idea is corroborated by observations of dust shells around asymptotic giant branch (AGB) stars, which are found to have temperatures in the range 800 to 1100 K ([Gail et al. 2013](#)). However, while the trend of increasing depletion with increasing T_C seems convincing for the elements mentioned above, there are also glaring exceptions to the trend for the elements Si and Mg but especially for Cl, As, and P. These latter three elements appear to have gas-phase abundances at $F_* = 0$ that are significantly higher than the corresponding solar values, which seems particularly unusual since the elements have moderate-to-high condensation temperatures.

One possible factor that could be influencing the unusual Cl and P depletions is that the column density

measurements for the dominant singly-ionized species may not be very accurate. All of the Cl II measurements (and over half of the P II results) compiled by [Jenkins \(2009\)](#) are from observations obtained by the Copernicus satellite (e.g., [Jenkins et al. 1986](#)). More precise measurements of interstellar column densities may be derived from spectra acquired using the higher resolution and/or higher sensitivity instruments of the Hubble Space Telescope (HST) and Far Ultraviolet Spectroscopic Explorer (FUSE).

An even more important factor in the case of P depletions is that the transition oscillator strengths (f -values) used by [Jenkins \(2009\)](#) and others to derive P II column densities are in need of revision. [Jenkins \(2009\)](#) adopted theoretical P II f -values originally obtained by [Hibbert \(1988\)](#). However, more precise experimentally-determined f -values for the important $\lambda 1152$ and $\lambda 1301$ transitions are now available ([Federman et al. 2007](#); [Brown et al. 2018](#)). These new experimental results indicate that the P II column densities obtained from the $\lambda 1152$ and $\lambda 1301$ transitions should be revised downward by 0.045 dex and 0.188 dex, respectively, in agreement with recent theoretical calculations ([Tayal 2003](#); [Froese Fischer et al. 2006](#)). Furthermore, these more recent theoretical efforts suggest that a downward revision of ~ 0.4 dex is required for column densities derived using the older [Hibbert \(1988\)](#) value for P II $\lambda 1532$ (e.g., [Lebouteiller et al. 2005](#); [Jenkins 2009](#)).

A major contributing factor to the unusual Cl depletions reported by [Jenkins \(2009\)](#) is that he considered only Cl II column densities when deriving total Cl abundances, ignoring any contribution from Cl I. However, because Cl^+ reacts rapidly with H_2 to form HCl^+ , which leads (eventually) to Cl^0 and H^0 , Cl will be predominantly neutral in regions where H_2 is abundant ([Jura 1974](#); [Jura & York 1978](#)). Indeed, there are a number of sight lines where previous studies indicate that $N(\text{Cl I}) > N(\text{Cl II})$ (e.g., [Harris & Bromage 1984](#); [Jenkins et al. 1986](#); [Moomey et al. 2012](#)) and these sight lines tend to have high molecular hydrogen fractions. Since these same sight lines will likely have high values of F_* as well, the depletion trend for Cl calculated by [Jenkins \(2009\)](#) is too steep and the extrapolated value of $[\text{Cl}/\text{H}]$ at $F_* = 0$ is too high.

In this investigation, we seek to present a definitive analysis of interstellar P and Cl depletions based on high-quality archival HST and FUSE data. The selection of sight lines and the steps involved in processing the archival data are described in Section 2. The procedures used to obtain column densities of P II, Cl I, and Cl II for the sight lines in our survey are explained in Section 3. In Section 4.1, we reexamine the relation-

ships that exist between various Cl and H species. In Section 4.2, the column densities derived in Section 3 are used to evaluate the depletion trends for P and Cl, with some additional insights discussed in Section 4.3. In Section 4.4, we use the observed neutral chlorine fractions to estimate the amount of atomic hydrogen associated with the molecular gas in each direction. The implications of our results are discussed in Section 5. Our summary and conclusions are presented in Section 6. Two appendices compile a set of chlorine measurements from Copernicus observations and present an analysis of fluorine depletions from the literature.

2. OBSERVATIONS AND DATA PROCESSING

Since the ionization potential of P I (10.5 eV) is below that of neutral hydrogen (13.6 eV), most P in neutral, diffuse clouds is singly ionized. The same would be true of Cl, since its first ionization potential is 13.0 eV, except that Cl^+ reacts exothermically with H_2 , which leads to the conversion of Cl^+ to Cl^0 in regions where H_2 is optically thick (e.g., Neufeld & Wolfire 2009). Thus, while P II column densities are sufficient for studies of interstellar P abundances, column densities of both Cl I and Cl II are required for an evaluation of total interstellar Cl abundances.

Most previous studies of interstellar P have relied on either the P II $\lambda 1152$ transition or the $\lambda 1301$ transition. However, the former is often strongly saturated and the

latter may be blended with the wing of the nearby strong O I $\lambda 1302$ absorption feature. Fewer studies make use of the weak P II $\lambda 1532$ absorption line, which is unblended and typically unaffected by saturation, yet still strong enough to yield reliable measurements for most sight lines. Similarly, while the Cl I $\lambda 1347$ line is almost always present in stellar spectra probing diffuse molecular gas, this feature is very often affected by saturation in the line core, making reliable column density determinations difficult. The nearby Cl I line at 1379.5 Å is much weaker and yet (again) is often strong enough to be reliably measured.

Since the goal of our survey is to accurately deduce the depletion characteristics of Cl and P, minimizing the associated uncertainties, we use measurements of the P II $\lambda 1532$ and Cl I $\lambda 1379$ absorption features, from high or medium resolution STIS spectra, wherever possible. We include measurements of the P II $\lambda 1301$ line only in cases where there is no apparent blending with O I $\lambda 1302$. The strong Cl I $\lambda 1347$ line is included in our survey. However, in most cases, a weaker Cl I line (typically $\lambda 1379$) is used to help constrain the total column density. For some sight lines, we use observations of the Cl I $\lambda 1004$, $\lambda 1094$, or $\lambda 1097$ transition, available from FUSE data, to constrain the total Cl I column density (see Section 3.2). The column density of Cl II is derived from observations of the Cl II line at 1071.0 Å, available from FUSE spectra.

Table 1. Stellar Data for the Combined Sample

Star	Name	Sp. Type	V	$E(B-V)$	l	b	d^a	z
			(mag)	(mag)	(deg)	(deg)	(kpc)	(kpc)
HD 108	...	O8fp	7.40	0.43	117.93	+1.25	$1.93^{+0.08}_{-0.09}$	+0.042
HD 1383	...	B1II	7.63	0.47	119.02	−0.89	$2.50^{+0.18}_{-0.13}$	−0.039
HD 3827	...	B0.7V	7.95	0.02	120.79	−23.23	$1.67^{+0.14}_{-0.15}$	−0.658
HD 12323	...	ON9.2V	8.92	0.23	132.91	−5.87	$2.44^{+0.23}_{-0.22}$	−0.250
HD 13268	...	ON8.5IIIn	8.18	0.36	133.96	−4.99	$1.77^{+0.09}_{-0.07}$	−0.154
HD 13745	V354 Per	O9.7IIIn	7.90	0.46	134.58	−4.96	$2.28^{+0.15}_{-0.09}$	−0.197
HD 14434	...	O5.5Vnfp	8.49	0.48	135.08	−3.82	$2.24^{+0.10}_{-0.09}$	−0.150
HD 15137	...	O9.5II-IIIn	7.86	0.35	137.46	−7.58	$2.05^{+0.17}_{-0.13}$	−0.271
HD 23478	...	B3IV	6.67	0.27	160.76	−17.42	$0.249^{+0.004}_{-0.003}$	−0.074
HD 24190	...	B2Vn	7.45	0.30	160.39	−15.18	$0.375^{+0.005}_{-0.005}$	−0.098
HD 24534	X Per	O9.5III	6.72	0.59	163.08	−17.14	$0.596^{+0.017}_{-0.014}$	−0.176
HD 25443	...	B0.5III	6.77	0.54	143.68	+7.35	$1.13^{+0.07}_{-0.06}$	+0.145
HD 37903	...	B1.5V	7.83	0.35	206.85	−16.54	$0.394^{+0.003}_{-0.004}$	−0.112

Table 1 continued

Table 1 (*continued*)

Star	Name	Sp. Type	V	$E(B-V)$	l	b	d^a	z
			(mag)	(mag)	(deg)	(deg)	(kpc)	(kpc)
HD 41161	...	O8Vn	6.76	0.21	164.97	+12.89	$1.43^{+0.12}_{-0.10}$	+0.319
HD 46223	...	O4Vf	7.28	0.54	206.44	-2.07	$1.39^{+0.05}_{-0.06}$	-0.050
HD 52266	...	O9.5IIIn	7.23	0.29	219.13	-0.68	$1.35^{+0.06}_{-0.07}$	-0.016
HD 53975	...	O7.5Vz	6.50	0.21	225.68	-2.32	$1.12^{+0.07}_{-0.06}$	-0.045
HD 63005	...	O7Vf	9.13	0.27	242.47	-0.93	$3.72^{+0.60}_{-0.50}$	-0.060
HD 66788	...	O8V	9.83	0.22	245.43	+2.05	$3.31^{+0.32}_{-0.30}$	+0.119
HD 72754	FY Vel	B2I:pe	8.88	0.36	266.83	-5.82	$1.62^{+0.05}_{-0.05}$	-0.165
HD 73882	NX Vel	O8.5IV	7.19	0.70	260.18	+0.64	$0.737^{+0.031}_{-0.030}$	+0.008
HD 75309	...	B1IIp	7.84	0.29	265.86	-1.90	$1.82^{+0.12}_{-0.13}$	-0.060
HD 79186	GX Vel	B5Ia	5.00	0.40	267.36	+2.25	$1.81^{+0.34}_{-0.23}$	+0.071
HD 88115	...	B1.5IIn	9.36	0.16	285.32	-5.53	$2.53^{+0.16}_{-0.17}$	-0.243
HD 89137	...	ON9.7IIIn	7.97	0.27	279.69	+4.45	$2.44^{+0.20}_{-0.14}$	+0.189
HD 90087	...	O9.2III	8.92	0.28	285.16	-2.13	$2.19^{+0.11}_{-0.12}$	-0.082
HD 91597	...	B1IIIne	9.92	0.30	286.86	-2.37	$3.90^{+0.26}_{-0.24}$	-0.161
HD 91651	...	ON9.5IIIn	9.52	0.28	286.55	-1.72	$1.85^{+0.07}_{-0.07}$	-0.055
HD 91824	...	O7Vfz	8.14	0.24	285.70	+0.07	$1.83^{+0.08}_{-0.08}$	+0.002
HD 91983	...	B1III	8.55	0.29	285.88	+0.05	$2.40^{+0.15}_{-0.14}$	+0.002
HD 92554	...	O9.5IIn	10.15	0.39	287.60	-2.02	$4.04^{+0.31}_{-0.28}$	-0.142
HD 93129	...	O2If*	6.90	0.48	287.41	-0.57	$2.41^{+0.10}_{-0.10}$	-0.024
HD 93205	V560 Car	O3.5V	7.75	0.38	287.57	-0.71	$2.25^{+0.12}_{-0.11}$	-0.028
HD 93222	...	O7III f	8.10	0.36	287.74	-1.02	$2.41^{+0.14}_{-0.15}$	-0.043
HD 93843	...	O5III f	7.33	0.27	288.24	-0.90	$2.37^{+0.19}_{-0.14}$	-0.037
HD 94493	...	B1Ib	7.59	0.23	289.01	-1.18	$2.15^{+0.14}_{-0.12}$	-0.044
HD 97175	...	B0.5III	9.20	0.18	294.53	-9.17	$2.48^{+0.18}_{-0.14}$	-0.396
HD 99857	...	B0.5Ib	7.49	0.35	294.78	-4.94	$1.80^{+0.08}_{-0.07}$	-0.155
HD 99890	...	B0IIIn	9.26	0.24	291.75	+4.43	$2.53^{+0.18}_{-0.17}$	+0.195
HD 100199	...	B0IIIn	8.17	0.30	293.94	-1.49	$1.73^{+0.14}_{-0.11}$	-0.045
HD 101190	...	O6IVf	7.33	0.37	294.78	-1.49	$2.36^{+0.13}_{-0.12}$	-0.061
HD 103779	...	B0.5Iab	7.22	0.21	296.85	-1.02	$2.02^{+0.10}_{-0.08}$	-0.036
HD 104705	DF Cru	B0Ib	9.11	0.23	297.45	-0.34	$1.94^{+0.16}_{-0.15}$	-0.011
HD 108639	...	B0.2III	8.57	0.37	300.22	+1.95	$1.98^{+0.10}_{-0.11}$	+0.067
HD 109399	...	B0.7II	7.67	0.21	301.71	-9.88	$2.33^{+0.13}_{-0.14}$	-0.400
HD 114886	...	O9III	6.89	0.40	305.52	-0.83	$1.83^{+0.95}_{-0.78}$	-0.026
HD 115455	...	O8III f	7.97	0.47	306.06	+0.22	$1.80^{+0.09}_{-0.07}$	+0.007
HD 116852	...	O8.5II-III f	8.47	0.21	304.88	-16.13	$3.42^{+0.39}_{-0.32}$	-0.949
HD 121968	...	B1V	10.26	0.07	333.97	+55.84	$3.94^{+0.91}_{-0.63}$	+3.26
HD 122879	...	B0Ia	6.50	0.36	312.26	+1.79	$2.22^{+0.16}_{-0.13}$	+0.069
HD 124314	...	O6IVnf	6.64	0.53	312.67	-0.42	$1.61^{+0.11}_{-0.10}$	-0.012
HD 137595	...	B3Vn	7.49	0.25	336.72	+18.86	$0.751^{+0.021}_{-0.022}$	+0.243
HD 144965	...	B2Vne	7.11	0.35	339.04	+8.42	$0.258^{+0.002}_{-0.002}$	+0.038

Table 1 continued

Table 1 (*continued*)

Star	Name	Sp. Type	V	$E(B-V)$	l	b	d^a	z
			(mag)	(mag)	(deg)	(deg)	(kpc)	(kpc)
HD 147683	V760 Sco	B4V+B4V	7.05	0.39	344.86	+10.09	$0.290^{+0.002}_{-0.002}$	+0.051
HD 147888	ρ Oph D	B3V	6.74	0.47	353.65	+17.71	$0.124^{+0.006}_{-0.006}$	+0.038
HD 147933	ρ Oph A	B2V	5.05	0.45	353.69	+17.69	$0.137^{+0.003}_{-0.003}$	+0.042
HD 148422	...	B1Ia	8.65	0.29	329.92	-5.60	$4.18^{+0.52}_{-0.31}$	-0.408
HD 148937	...	O6f?p	6.71	0.65	336.37	-0.22	$1.15^{+0.03}_{-0.03}$	-0.004
HD 151805	...	B1Ib	8.86	0.43	343.20	+1.59	$1.51^{+0.07}_{-0.06}$	+0.042
HD 152590	V1297 Sco	O7.5Vz	9.29	0.48	344.84	+1.83	$1.68^{+0.08}_{-0.06}$	+0.053
HD 156359	...	B0Ia	9.72	0.14	328.68	-14.52	$8.98^{+3.14}_{-2.11}$	-2.25
HD 157857	...	O6.5IIIf	7.78	0.43	12.97	+13.31	$2.22^{+0.20}_{-0.13}$	+0.511
HD 163522	...	B1Ia	8.43	0.19	349.57	-9.09	$4.01^{+0.56}_{-0.47}$	-0.633
HD 165246	...	O8Vn	7.60	0.38	6.40	-1.56	$1.19^{+0.04}_{-0.05}$	-0.032
HD 165955	...	B3Vn	9.59	0.15	357.41	-7.43	$1.47^{+0.12}_{-0.09}$	-0.190
HD 167402	...	B0Ib	9.03	0.21	2.26	-6.39	$4.94^{+0.83}_{-0.73}$	-0.550
HD 168076	...	O4IIIf	8.25	0.78	16.94	+0.84	$1.65^{+1.51}_{-0.67}$	+0.024
HD 168941	...	O9.5IVp	9.37	0.24	5.82	-6.31	$4.00^{+0.60}_{-0.53}$	-0.440
HD 170740	...	B2IV-V	5.72	0.48	21.06	-0.53	$0.225^{+0.005}_{-0.005}$	-0.002
HD 177989	...	B0III	9.34	0.23	17.81	-11.88	$2.41^{+0.20}_{-0.19}$	-0.496
HD 178487	...	B0Ib	8.69	0.35	25.78	-8.56	$2.85^{+0.36}_{-0.25}$	-0.425
HD 179407	...	B0.5Ib	9.44	0.28	24.02	-10.40	$4.44^{+0.69}_{-0.47}$	-0.802
HD 185418	...	B0.5V	7.49	0.50	53.60	-2.17	$0.692^{+0.010}_{-0.009}$	-0.026
HD 190918	V1676 Cyg	O9.7Iab+WN4	6.75	0.45	72.65	+2.07	$1.78^{+0.07}_{-0.07}$	+0.064
HD 191877	...	B1Ib	6.27	0.21	61.57	-6.45	$1.73^{+0.11}_{-0.13}$	-0.194
HD 192035	RX Cyg	B0III-IVn	8.22	0.34	83.33	+7.76	$1.65^{+0.06}_{-0.06}$	+0.223
HD 192639	...	O7.5Iab	7.11	0.66	74.90	+1.48	$1.81^{+0.07}_{-0.06}$	+0.047
HD 195455	...	B0.5III	9.20	0.10	20.27	-32.14	$2.35^{+0.35}_{-0.24}$	-1.25
HD 195965	...	B0V	6.97	0.25	85.71	+5.00	$0.790^{+0.023}_{-0.025}$	+0.069
HD 198478	55 Cyg	B3Ia	4.86	0.57	85.75	+1.49	$1.84^{+0.35}_{-0.22}$	+0.048
HD 198781	...	B0.5V	6.45	0.35	99.94	+12.61	$0.915^{+0.022}_{-0.027}$	+0.200
HD 201345	...	ON9.2IV	7.76	0.15	78.44	-9.54	$1.83^{+0.15}_{-0.11}$	-0.303
HD 202347	...	B1.5V	7.50	0.17	88.22	-2.08	$0.764^{+0.023}_{-0.019}$	-0.028
HD 203374	...	B0IVpe	6.67	0.53	100.51	+8.62	$2.04^{+1.42}_{-0.76}$	+0.306
HD 203938	...	B0.5IV	7.08	0.74	90.56	-2.23	$2.96^{+2.26}_{-1.35}$	-0.115
HD 206267	...	O6Vf	5.62	0.53	99.29	+3.74	$0.790^{+0.172}_{-0.112}$	+0.052
HD 206773	...	B0Vpe	6.87	0.45	99.80	+3.62	$0.888^{+0.016}_{-0.014}$	+0.056
HD 207198	...	O8.5II	5.94	0.62	103.14	+6.99	$0.978^{+0.034}_{-0.027}$	+0.119
HD 207308	...	B0.5V	7.49	0.53	103.11	+6.82	$0.906^{+0.017}_{-0.013}$	+0.108
HD 207538	...	O9.7IV	7.30	0.64	101.60	+4.67	$0.830^{+0.013}_{-0.013}$	+0.068
HD 208440	...	B1V	7.91	0.28	104.03	+6.44	$0.877^{+0.019}_{-0.018}$	+0.098
HD 209339	...	O9.7IV	8.51	0.36	104.58	+5.87	$0.936^{+0.028}_{-0.024}$	+0.096
HD 210809	...	O9Iab	7.56	0.31	99.85	-3.13	$3.66^{+0.52}_{-0.34}$	-0.200

Table 1 *continued*

Table 1 (*continued*)

Star	Name	Sp. Type	V	$E(B-V)$	l	b	d^a	z
			(mag)	(mag)	(deg)	(deg)	(kpc)	(kpc)
HD 210839	λ Cep	O6.5Infp	5.05	0.57	103.83	+2.61	$0.833^{+0.066}_{-0.049}$	+0.038
HD 212791	V408 Lac	B3ne	8.02	0.17	101.64	−4.30	$0.893^{+0.019}_{-0.016}$	−0.067
HD 218915	...	O9.2Iab	7.20	0.30	108.06	−6.89	$2.97^{+0.33}_{-0.25}$	−0.357
HD 219188	...	B0.5IIIn	7.06	0.13	83.03	−50.17	$2.10^{+0.25}_{-0.27}$	−1.61
HD 220057	...	B3IV	6.94	0.23	112.13	+0.21	$0.385^{+0.004}_{-0.004}$	+0.001
HD 224151	V373 Cas	B0.5II-III	6.00	0.44	115.44	−4.64	$1.89^{+0.13}_{-0.10}$	−0.153
HDE 232522	...	B1II	8.70	0.27	130.70	−6.71	$3.46^{+0.41}_{-0.44}$	−0.404
HDE 303308	...	O4.5Vfc	8.17	0.45	287.59	−0.61	$2.17^{+0.09}_{-0.10}$	−0.023
HDE 308813	...	O9.7IVn	9.73	0.34	294.79	−1.61	$2.43^{+0.11}_{-0.09}$	−0.068
BD+35 4258	...	B0.5Vn	9.46	0.25	77.19	−4.74	$2.21^{+0.14}_{-0.11}$	−0.182
BD+53 2820	...	B0IVn	9.96	0.29	101.24	−1.69	$3.57^{+0.25}_{-0.17}$	−0.105
CPD−59 2603	V572 Car	O7Vnz	8.81	0.46	287.59	−0.69	$2.63^{+0.16}_{-0.14}$	−0.032
CPD−59 4552	...	B1III	8.24	0.38	303.22	+2.47	$2.04^{+0.07}_{-0.06}$	+0.088
CPD−69 1743	...	B0.5IIIn	9.64	0.30	303.71	−7.35	$3.20^{+0.19}_{-0.16}$	−0.410

^aDistances are based on Gaia EDR3 parallax measurements (Bailer-Jones et al. 2021).

2.1. Processing of the STIS Data

Archival STIS spectra acquired using either the medium-resolution echelle grating (E140M) or the high-resolution grating (E140H) at central wavelength settings that cover the relevant P II and/or Cl I lines were obtained from the Mikulski Archive for Space Telescopes (MAST). We focus only on sight lines with reliable column densities of H I and H₂ published in the literature (e.g., Jenkins 2019). An additional requirement for the Cl analysis is that each sight line must have FUSE observations available.¹ The final P and Cl samples differ from one another slightly due to the constraints placed on measuring the various absorption features (as discussed above). Basic information regarding the background stars associated with the 107 sight lines that constitute the final combined sample is presented in Table 1. The wavelengths and adopted oscillator strengths for the interstellar lines of interest to our survey are provided in Table 2.

¹ An exception is made in the case of HD 147933 (ρ Oph A), which was not observed with FUSE but does have high-resolution STIS spectra covering the Cl I λ 1347 transition. Mooney et al. (2012) obtained Cl I and Cl II column densities for this sight line using Copernicus observations. However, the total Cl abundance derived from their analysis is unusually low. We therefore reexamine the Copernicus data toward ρ Oph A, in conjunction with the newer high-resolution STIS spectra, in order to re-evaluate the Cl I and Cl II column densities in this direction.

After downloading the pipeline-processed archival files from MAST, the STIS data were further reduced in a manner analogous to that described in Ritchey et al. (2011, 2018). Multiple exposures of a given target acquired with the same echelle grating were co-added to increase the signal-to-noise (S/N) ratio in the final spectrum. When a feature of interest appeared in adjacent echelle orders with sufficient continua on both sides of the line, the overlapping portions of the two orders were averaged together. Portions of the co-added spectrum surrounding interstellar lines of interest (typically 2 Å wide) were cut from the data. These smaller spectral segments were then normalized by fitting the continuum regions with a low-order polynomial function.

In most cases, the process of normalizing the continuum was straightforward. The P II λ 1532 line and the Cl I λ 1347 and λ 1379 lines are relatively isolated and are easily distinguished from the underlying stellar spectra. However, as already mentioned, the P II λ 1301 line is positioned very close to the strong O I λ 1302 resonance feature. (The difference in wavelength between the two transitions amounts to 68 km s^{−1}.) Thus, great care had to be taken in choosing an appropriate normalization for the P II λ 1301 line. Any cases where the P II line was inextricably blended with O I were rejected. We considered the spectrum to be “blended” if there was no obvious continuum region between the P II feature and the core of the O I line. Of the 107 sight lines in our combined sample, only 48 were deemed to have unblended

Table 2. Atomic Data

Species	λ_0 (Å)	f	Ref.
P II	1152.818	0.272	1
	1301.874	0.0196	2
	1532.533	0.00737	3
Cl I	1004.678	0.0473	4
	1094.769	0.0385	4
	1097.369	0.0088	5
	1347.240	0.153	5
	1379.528	0.00269	6
Cl II	1071.036	0.0142	7

References—(1) [Federman et al. \(2007\)](#), (2) [Brown et al. \(2018\)](#), (3) this work, (4) [Alkhayat et al. \(2019\)](#), (5) [Schectman et al. \(1993\)](#), (6) [Oliver & Hibbert \(2013\)](#), (7) [Schectman et al. \(2005\)](#).

P II $\lambda 1301$ absorption lines. Furthermore, in many of the “unblended” cases, the P II feature is superimposed onto the gently sloping damping wing of the O I line. Thus, in these cases, the continuum being fit is not the stellar continuum but the Lorentzian damping wing of the O I resonance line.

2.2. Processing of the FUSE Data

All FUSE exposures for the sight lines in our survey were downloaded from the MAST archive. For each detector segment, multiple exposures of a given target were cross-correlated in wavelength space and then co-added by taking the weighted mean of the measured intensities.² The overlapping portions of different detector segments that covered lines of interest to our survey were then cross-correlated and co-added in the same manner. In this way, we produced high S/N ratio spectra for the Cl II $\lambda 1071$ line and also, in some cases, for the Cl I $\lambda 1004$, $\lambda 1094$, and $\lambda 1097$ transitions.

A major complication when dealing with FUSE spectra are the numerous absorption features arising from electronic transitions within the Lyman and Werner bands of H₂. Most concerning for this investigation is that the $R(4)$ line of the H₂ (3–0) Lyman band at

² The registration and co-addition of FUSE data was accomplished using IDL routines within the LTOOLS package, available at the following URL: https://archive.stsci.edu/fuse/analysis/idl_tools.html.

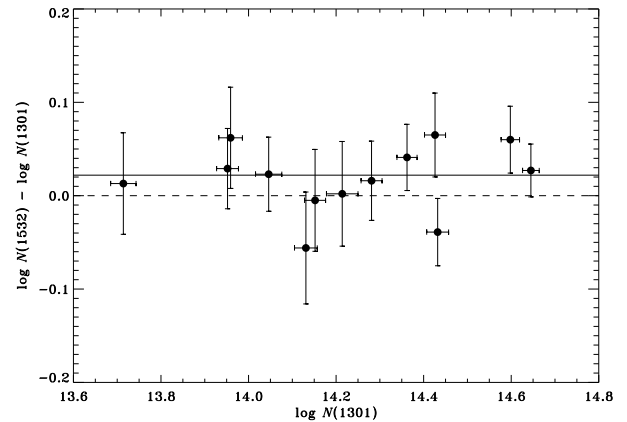


Figure 1. Logarithmic difference in the column densities obtained from the P II $\lambda 1301$ and $\lambda 1532$ lines when the theoretical f -value from [Froese Fischer et al. \(2006\)](#) is adopted for the $\lambda 1532$ transition and the experimental f -value from [Brown et al. \(2018\)](#) is adopted for P II $\lambda 1301$. The weighted mean of the difference (0.022 dex, as indicated by the solid horizontal line) yields an empirical f -value for the P II $\lambda 1532$ transition of 0.00737.

1070.9 Å is very close to the Cl II line at 1071.0 Å. (The velocity separation between the two lines is only 38 km s^{−1}.) The difficulty in distinguishing the two features is compounded by the relatively low resolution of the FUSE spectra ($\Delta v \approx 18$ km s^{−1}). The stellar continuum surrounding the H₂ lines in the vicinity of the Cl II $\lambda 1071$ feature is easy to identify in most cases. The same continuum fitting procedure used for the STIS data provided adequate solutions for the normalization of the FUSE spectra. A more specialized procedure was required to deblend the absorption features associated with the H₂ and Cl II lines near 1071 Å. This procedure is described in more detail in Section 3.2.2.

3. RESULTS ON COLUMN DENSITIES

In order to obtain column densities for P II, Cl I, and Cl II for the sight lines in our survey, we employed the technique of multi-component Voigt profile fitting using the code ISMOD ([Sheffer et al. 2008](#)). The profile fitting routine treats the column density N , Doppler broadening parameter b , and velocity v of each component as a free parameter and seeks to minimize the root mean square (rms) deviations between the observed spectrum and the synthetic one. In the following subsections we describe in more detail the specific procedures used to fit the P II, Cl I, and Cl II lines, each of which presented us with a unique challenge.

3.1. Phosphorus Column Densities

For our analysis of P II column densities, we adopt the experimentally determined oscillator strength for the

P II $\lambda 1301$ transition recently published by [Brown et al. \(2018\)](#). Their f -value for P II $\lambda 1301$ indicates that a downward revision of 0.188 dex should be applied to column densities derived using the older [Hibbert \(1988\)](#) f -value (which is the one recommended by [Morton 2003](#)). The [Brown et al. \(2018\)](#) f -value for P II $\lambda 1301$ is consistent with more recent theoretical determinations ([Tayal 2003](#); [Froese Fischer et al. 2006](#)), which indicate that the f -value for P II $\lambda 1532$ is also in need of substantial

revision. The theoretical calculations of [Tayal \(2003\)](#) and [Froese Fischer et al. \(2006\)](#) suggest that a reduction in column density of ~ 0.4 dex is needed for results based on the [Hibbert \(1988\)](#) f -value for P II $\lambda 1532$. Since no recent experimental result is available for P II $\lambda 1532$, we derived an empirical f -value for this transition based on high-resolution STIS spectra.

Table 3. Phosphorus Column Densities

Star	$W_{\lambda}(1301)$ (mÅ)	$\log N(1301)$	$W_{\lambda}(1532)$ (mÅ)	$\log N(1532)$	$\log N(\text{P II})^a$
HD 108	32.6 ± 2.1	14.49 ± 0.03	14.49 ± 0.03
HD 1383	40.0 ± 3.1	14.56 ± 0.04	14.56 ± 0.04
HD 12323	28.4 ± 2.0	14.45 ± 0.04	14.45 ± 0.04
HD 13268	39.9 ± 4.5	14.52 ± 0.05	14.52 ± 0.05
HD 13745	44.1 ± 5.1	14.53 ± 0.05	14.53 ± 0.05
HD 14434	52.2 ± 4.6	14.75 ± 0.04	14.75 ± 0.04
HD 15137	31.7 ± 1.9	14.44 ± 0.03	14.44 ± 0.03
HD 23478	18.8 ± 0.5	13.95 ± 0.02	11.9 ± 1.0	13.96 ± 0.04	13.95 ± 0.02
HD 24190	28.1 ± 0.4	14.15 ± 0.02	17.2 ± 2.0	14.13 ± 0.05	14.15 ± 0.02
HD 24534	19.6 ± 0.2	14.05 ± 0.03	13.3 ± 0.7	14.05 ± 0.03	14.05 ± 0.02
HD 25443	64.5 ± 1.8	14.70 ± 0.03	14.70 ± 0.03
HD 37903	16.9 ± 0.5	13.88 ± 0.02	13.88 ± 0.02
HD 41161	49.9 ± 1.2	14.35 ± 0.02	14.35 ± 0.02
HD 46223	44.1 ± 1.0	14.61 ± 0.03	14.61 ± 0.03
HD 52266	50.3 ± 0.6	14.46 ± 0.03	14.46 ± 0.03
HD 53975	41.8 ± 0.8	14.27 ± 0.02	14.27 ± 0.02
HD 63005	27.3 ± 2.2	14.47 ± 0.04	14.47 ± 0.04
HD 66788	31.6 ± 3.3	14.39 ± 0.04	14.39 ± 0.04
HD 72754	34.8 ± 2.2	14.33 ± 0.04	14.33 ± 0.04
HD 73882	33.9 ± 1.6	14.22 ± 0.03	14.22 ± 0.03
HD 79186	51.6 ± 2.4	14.46 ± 0.03	14.46 ± 0.03
HD 88115 ^b	33.3 ± 1.8	14.15 ± 0.03	14.15 ± 0.03
	29.2 ± 2.8	14.23 ± 0.05	16.1 ± 4.2	14.12 ± 0.10	14.20 ± 0.05
HD 89137	40.2 ± 1.8	14.27 ± 0.03	14.27 ± 0.03
HD 90087	45.3 ± 0.8	14.36 ± 0.02	30.1 ± 1.7	14.38 ± 0.03	14.37 ± 0.02
HD 91597	47.5 ± 4.1	14.67 ± 0.04	14.67 ± 0.04
HD 91651	35.3 ± 3.3	14.41 ± 0.04	14.41 ± 0.04
HD 91824	50.6 ± 0.9	14.38 ± 0.02	14.38 ± 0.02
HD 91983	55.5 ± 2.1	14.44 ± 0.02	14.44 ± 0.02
HD 92554	44.2 ± 6.7	14.57 ± 0.06	14.57 ± 0.06

Table 3 continued

Table 3 (*continued*)

Star	$W_{\lambda}(1301)$	$\log N(1301)$	$W_{\lambda}(1532)$	$\log N(1532)$	$\log N(\text{P II})^a$
	(mÅ)		(mÅ)		
HD 93222	49.8 ± 1.3	14.59 ± 0.01	14.59 ± 0.01
HD 93843	24.7 ± 2.3	14.30 ± 0.04	14.30 ± 0.04
HD 94493	48.6 ± 1.8	14.35 ± 0.02	14.35 ± 0.02
HD 97175	28.8 ± 2.2	14.19 ± 0.04	14.19 ± 0.04
HD 99857	37.7 ± 2.4	14.54 ± 0.04	14.54 ± 0.04
HD 99890	30.1 ± 3.9	14.41 ± 0.05	14.41 ± 0.05
HD 100199	29.9 ± 2.8	14.39 ± 0.04	14.39 ± 0.04
HD 101190 ^b	25.0 ± 2.9	14.31 ± 0.05	14.31 ± 0.05
	24.7 ± 0.8	14.31 ± 0.02	14.31 ± 0.02
HD 103779	29.3 ± 1.8	14.36 ± 0.03	14.36 ± 0.03
HD 104705	28.6 ± 0.9	14.34 ± 0.02	14.34 ± 0.02
HD 108639	46.5 ± 2.3	14.57 ± 0.02	14.57 ± 0.02
HD 114886	38.0 ± 2.4	14.48 ± 0.03	14.48 ± 0.03
HD 116852	12.2 ± 2.0	14.06 ± 0.07	14.06 ± 0.07
HD 121968	12.4 ± 0.6	13.71 ± 0.03	7.1 ± 0.8	13.71 ± 0.05	13.71 ± 0.02
HD 122879	45.6 ± 2.0	14.63 ± 0.03	14.63 ± 0.03
HD 124314	73.2 ± 1.3	14.60 ± 0.02	51.9 ± 3.2	14.64 ± 0.03	14.61 ± 0.02
HD 137595	29.0 ± 1.0	14.13 ± 0.03	15.2 ± 2.0	14.05 ± 0.05	14.11 ± 0.02
HD 144965	18.1 ± 1.0	13.95 ± 0.04	13.95 ± 0.04
HD 147683	31.6 ± 1.3	14.21 ± 0.04	19.7 ± 1.9	14.19 ± 0.04	14.21 ± 0.03
HD 147888	24.7 ± 0.3	14.26 ± 0.05	14.26 ± 0.05
HD 147933	25.6 ± 0.5	14.32 ± 0.05	14.32 ± 0.05
HD 148422	48.9 ± 3.9	14.68 ± 0.04	14.68 ± 0.04
HD 148937	81.2 ± 1.3	14.65 ± 0.02	54.5 ± 2.5	14.65 ± 0.02	14.65 ± 0.01
HD 151805	58.8 ± 5.7	14.70 ± 0.04	14.70 ± 0.04
HD 152590	28.4 ± 2.4	14.45 ± 0.05	14.45 ± 0.05
HD 157857	43.6 ± 1.1	14.42 ± 0.03	14.42 ± 0.03
HD 163522	31.9 ± 2.9	14.40 ± 0.04	14.40 ± 0.04
HD 165955	20.4 ± 2.5	14.21 ± 0.05	14.21 ± 0.05
HD 167402	30.8 ± 3.2	14.38 ± 0.04	14.38 ± 0.04
HD 168941	19.5 ± 2.7	14.18 ± 0.06	14.18 ± 0.06
HD 170740	28.4 ± 1.4	14.36 ± 0.05	14.36 ± 0.05
HD 177989	17.0 ± 0.6	14.10 ± 0.02	14.10 ± 0.02
HD 178487	42.2 ± 3.0	14.55 ± 0.03	14.55 ± 0.03
HD 179407	37.6 ± 4.0	14.54 ± 0.05	14.54 ± 0.05
HD 185418	43.3 ± 0.7	14.43 ± 0.04	14.43 ± 0.04
HD 190918	50.5 ± 3.0	14.60 ± 0.03	14.60 ± 0.03
HD 191877	41.6 ± 1.2	14.30 ± 0.02	14.30 ± 0.02
HD 192035	50.9 ± 1.8	14.57 ± 0.05	33.5 ± 3.3	14.50 ± 0.05	14.53 ± 0.04
HD 195455	14.4 ± 1.3	13.73 ± 0.04	13.73 ± 0.04

Table 3 continued

Table 3 (*continued*)

Star	$W_{\lambda}(1301)$ (mÅ)	$\log N(1301)$	$W_{\lambda}(1532)$ (mÅ)	$\log N(1532)$	$\log N(\text{P II})^a$
HD 195965	39.9 ± 1.6	14.28 ± 0.02	24.6 ± 2.0	14.27 ± 0.03	14.28 ± 0.02
HD 198478	57.1 ± 2.5	14.78 ± 0.06	14.78 ± 0.06
HD 198781	38.4 ± 1.1	14.24 ± 0.02	14.24 ± 0.02
HD 201345	18.6 ± 2.2	14.14 ± 0.05	14.14 ± 0.05
HD 202347	21.2 ± 1.1	13.96 ± 0.03	13.6 ± 1.5	14.00 ± 0.05	13.97 ± 0.02
HD 203374 ^b	57.6 ± 1.1	14.47 ± 0.02	14.47 ± 0.02
	54.9 ± 1.5	14.49 ± 0.03	35.6 ± 2.7	14.47 ± 0.04	14.48 ± 0.02
HD 203938	47.3 ± 2.2	14.57 ± 0.05	14.57 ± 0.05
HD 206267	57.9 ± 1.4	14.52 ± 0.03	14.52 ± 0.03
HD 206773	46.0 ± 1.0	14.40 ± 0.03	14.40 ± 0.03
HD 207308	41.9 ± 1.3	14.44 ± 0.05	29.4 ± 1.3	14.43 ± 0.03	14.43 ± 0.03
HD 207538	54.9 ± 0.9	14.56 ± 0.04	36.5 ± 1.4	14.52 ± 0.03	14.53 ± 0.02
HD 209339	48.4 ± 1.1	14.43 ± 0.03	29.2 ± 1.6	14.37 ± 0.03	14.40 ± 0.02
HD 210809	43.3 ± 4.7	14.60 ± 0.05	14.60 ± 0.05
HD 210839	59.2 ± 1.0	14.49 ± 0.03	14.49 ± 0.03
HD 218915	25.9 ± 1.1	14.28 ± 0.02	14.28 ± 0.02
HD 219188	19.2 ± 0.4	13.91 ± 0.02	13.91 ± 0.02
HD 220057	26.4 ± 1.2	14.21 ± 0.05	14.21 ± 0.05
HD 224151	53.4 ± 1.8	14.43 ± 0.02	36.8 ± 3.2	14.47 ± 0.04	14.44 ± 0.02
HDE 308813	27.8 ± 3.0	14.35 ± 0.05	14.35 ± 0.05
BD+35 4258	29.7 ± 3.9	14.35 ± 0.05	14.35 ± 0.05
BD+53 2820	37.5 ± 5.2	14.58 ± 0.06	14.58 ± 0.06
CPD−59 2603 ^b	53.4 ± 1.9	14.64 ± 0.02	14.64 ± 0.02
	51.7 ± 2.2	14.78 ± 0.04	14.78 ± 0.04
CPD−59 4552	60.4 ± 2.5	14.51 ± 0.03	14.51 ± 0.03
CPD−69 1743	35.5 ± 4.7	14.50 ± 0.06	14.50 ± 0.06

^aFinal P II column density. In cases where both P II lines are measured, the final column density is obtained from the error weighted mean of the two results.

^bFirst line gives results from E140H data; second line gives results from E140M data.

There are thirteen sight lines in our sample that have high-resolution STIS spectra covering both P II transitions ($\lambda 1301$ and $\lambda 1532$) and have a $\lambda 1301$ profile that is not significantly blended with O I $\lambda 1302$. For these sight lines, we first fit the P II $\lambda 1301$ profile using the f -value from Brown et al. (2018). We then adopted the component structure found from the $\lambda 1301$ line to fit the $\lambda 1532$ profile using the f -value from Froese Fischer et al. (2006), which is $f(1532) = 0.00701$. The weighted mean of the (logarithmic) differences in the column densities derived from the $\lambda 1301$ and $\lambda 1532$ transitions is 0.022 ± 0.012 dex (see Figure 1). From

this result, we obtain an empirical f -value for the P II $\lambda 1532$ transition of 0.00737, very similar to the theoretical results of Tayal (2003) and Froese Fischer et al. (2006).

Our empirical f -value is adopted for the remaining sight lines in our sample with observations of P II $\lambda 1532$. (For the sight lines used in the derivation of the empirical f -value, the column densities obtained from the $\lambda 1532$ transition were adjusted downward by 0.022 dex.) The equivalent widths and column densities derived from profile synthesis fits to the P II $\lambda 1301$ and $\lambda 1532$ transitions are presented in Table 3 for the 92 sight lines in our final P sample. Errors in equivalent width account

for uncertainties due to noise in the spectra and uncertainties in continuum placement. The column density uncertainties include an additional term that depends on the degree of saturation in the absorption profile. In cases where both P II transitions were analyzed, final P II column densities were obtained from a weighted mean of the individual results.

For four of the sight lines in our sample (HD 88115, HD 101190, HD 203374, and CPD-59 2603), we were able to independently derive P II column densities from medium-resolution and high-resolution STIS spectra. Both results are included in Table 3. In three out of the four cases, the two independent results agree with one another within the uncertainties. However, for CPD-59 2603, the P II column densities derived from fits to the E140H and E140M spectra disagree at the 3.1σ level. Since the equivalent widths from the two fits are consistent with one another, the difference in column density is likely related to uncertainties regarding the degree of saturation in the line profile. Indeed, the fit to the medium resolution spectrum results in a smaller b -value for the dominant absorption component (1.3 versus 2.4 km s^{-1}) yielding a higher column density. The b -values are better constrained in fits to the higher resolution spectra. Thus, for the depletion analysis, we adopt the results from the E140H data for each of the four sight lines discussed here.

Examples of our fits to the P II $\lambda 1532$ and $\lambda 1301$ lines are presented in Figures 2 and 3. In each case, we provide both the unnormalized spectrum with the adopted continuum fit and the normalized spectrum with the derived profile synthesis fit. For each of the examples shown, the component structure obtained from the fit to the stronger P II $\lambda 1301$ feature was adopted in the fit to the $\lambda 1532$ line (as described above).

In Table 4, we present a comparison between the P II column densities that we obtain and the column densities reported in the literature for sight lines studied previously by [Lebouteiller et al. \(2005\)](#) and [Cartledge et al. \(2006\)](#). All of the previous results on $N(\text{P II})$ given in Table 4 have been adjusted to be consistent with the set of f -values adopted in this investigation (see Table 2). Also note that the P II column densities from [Lebouteiller et al. \(2005\)](#) shown in Table 4 are the ones that those authors obtain from STIS observations of the P II $\lambda 1532$ line. The [Cartledge et al. \(2006\)](#) column densities were derived from STIS observations of the P II $\lambda 1301$ line. Our values for $\log N(\text{P II})$ shown in Table 4 refer to the final P II column densities from Table 3. In some cases, these final values were obtained from the weighted mean of the results from the $\lambda 1301$ and $\lambda 1532$ lines.

Table 4. Comparison with Previous Studies: P II

Star	$\log N(\text{P II})$		
	This Work	Previous Result ^a	Ref.
HD 24534	14.05 ± 0.02	14.03 ± 0.05	1
HD 37903	13.88 ± 0.02	13.91 ± 0.04	2
HD 72754	14.33 ± 0.04	14.27 ± 0.04	2
HD 79186	14.46 ± 0.03	14.55 ± 0.06	2
HD 91824	14.38 ± 0.02	14.38 ± 0.03	2
HD 91983	14.44 ± 0.02	14.44 ± 0.04	2
HD 93222	14.59 ± 0.01	14.43 ± 0.01	1
HD 99857	14.54 ± 0.04	14.25 ± 0.02	1
HD 104705	14.34 ± 0.02	14.15 ± 0.04	1
HD 121968	13.71 ± 0.02	13.63 ± 0.09	1
HD 124314	14.61 ± 0.02	14.57 ± 0.24	1
HD 152590	14.45 ± 0.05	14.46 ± 0.02	2
HD 157857	14.42 ± 0.03	14.43 ± 0.04	2
HD 177989	14.10 ± 0.02	14.08 ± 0.07	1
HD 185418	14.43 ± 0.04	14.45 ± 0.03	2
HD 198478	14.78 ± 0.06	14.50 ± 0.03	2
HD 198781	14.24 ± 0.02	14.24 ± 0.04	2
HD 201345	14.14 ± 0.05	14.23 ± 0.06	2
HD 202347	13.97 ± 0.02	13.94 ± 0.07	1
HD 206773	14.40 ± 0.03	14.42 ± 0.04	2
HD 218915	14.28 ± 0.02	14.14 ± 0.09	1
HD 220057	14.21 ± 0.05	14.15 ± 0.03	2
HD 224151	14.44 ± 0.02	14.48 ± 0.09	1

^aAll previous results have been adjusted to be consistent with the set of f -values adopted in this investigation (see Table 2).

References—(1) [Lebouteiller et al. \(2005\)](#), (2) [Cartledge et al. \(2006\)](#).

Most of the previous results on $N(\text{P II})$ for the sight lines shown in Table 4 are consistent with our values at approximately the 1σ level. For HD 198478, however, the [Cartledge et al. \(2006\)](#) value is lower than ours by 4.3σ . [Cartledge et al. \(2006\)](#) report an equivalent width for the $\lambda 1301$ line toward HD 198478 (47.0 ± 1.4) that is lower than our equivalent width (57.1 ± 2.5). However, the difference in equivalent width is considerably smaller than the difference in column density (0.28 dex). The discrepancy seems to be caused, therefore, by a combination of continuum placement uncertainties and differences in the optical depth correction (via the b -value) for the dominant P II absorption component.

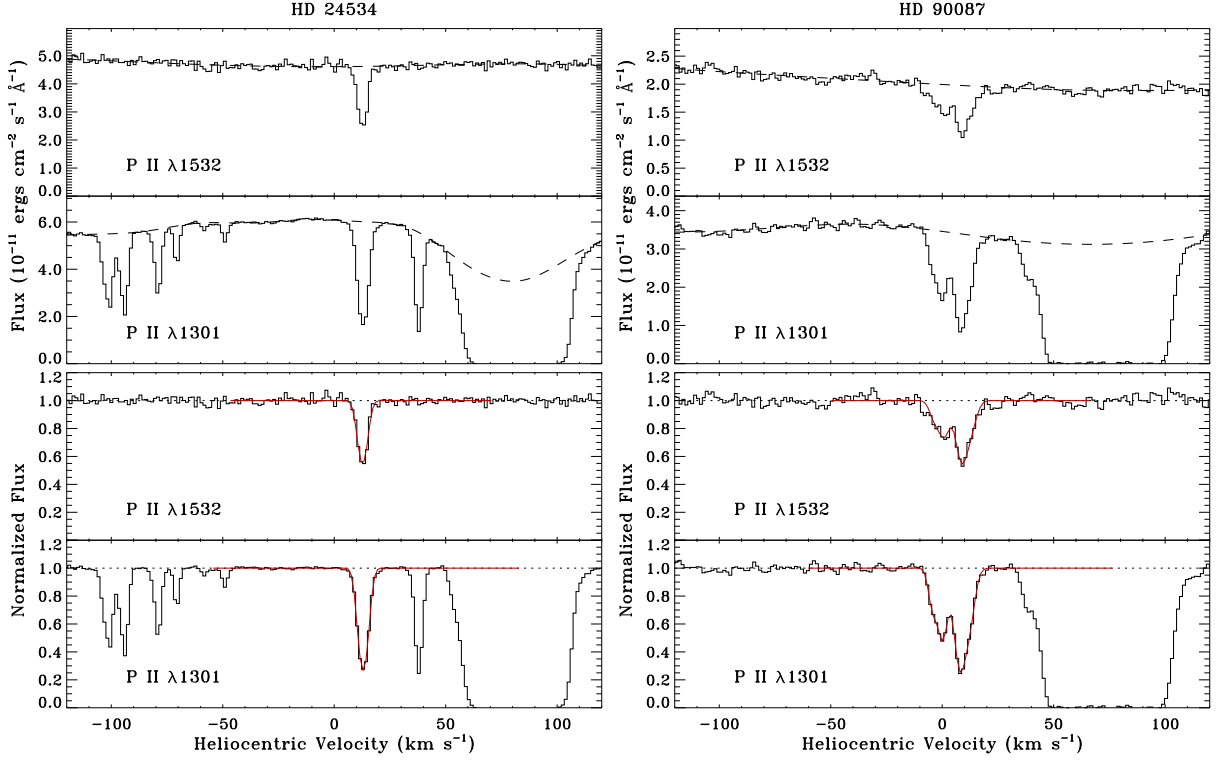


Figure 2. High-resolution STIS spectra in the vicinity of the P II $\lambda 1532$ and $\lambda 1301$ lines toward HD 24534 (left panels) and HD 90087 (right panels). Upper panels show the unnormalized spectra with dashed lines indicating the adopted continuum fits. Lower panels show the normalized spectra with solid red lines representing fits to the P II absorption profiles.

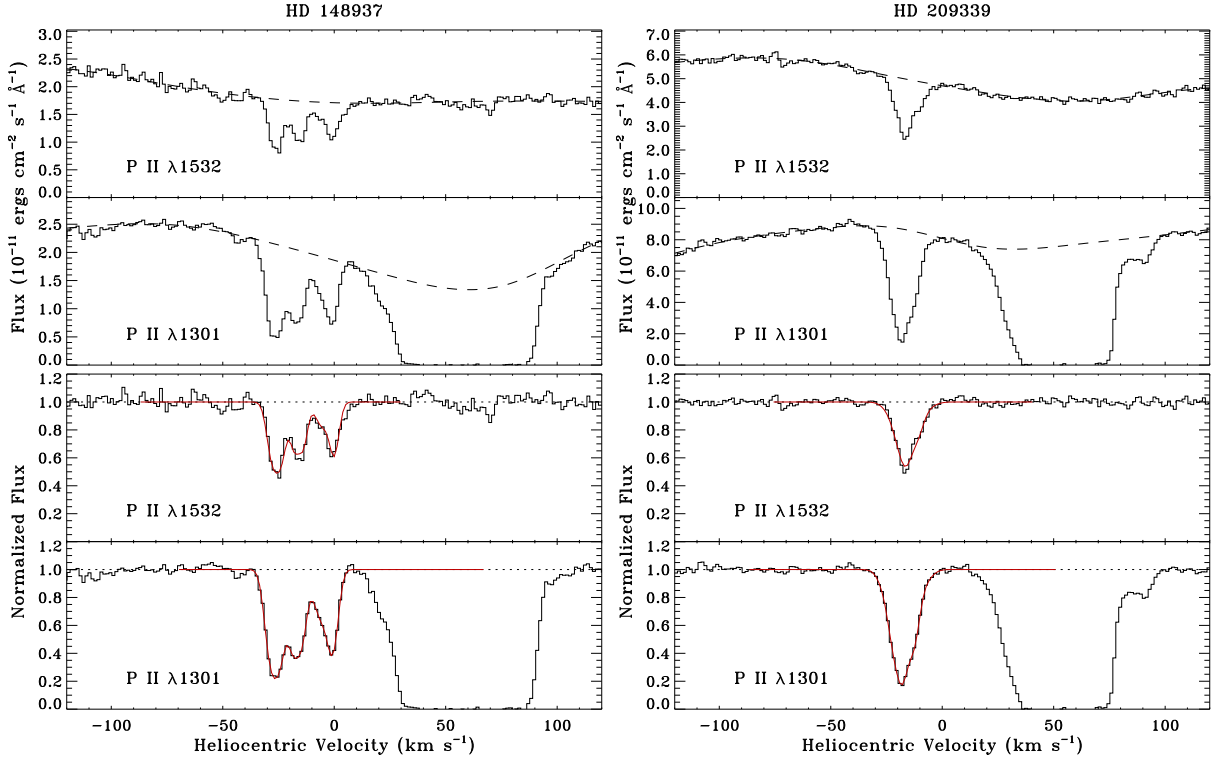


Figure 3. Same as Figure 2 except toward HD 148937 (left panels) and HD 209339 (right panels).

Similarly, there are three cases where the P II column density from [Lebouteiller et al. \(2005\)](#) is significantly lower than our value. The P II column densities reported by [Lebouteiller et al. \(2005\)](#) for the sight lines to HD 93222, HD 99857, and HD 104705 are lower than our values by 8.9σ , 6.9σ , and 4.3σ , respectively. While [Lebouteiller et al. \(2005\)](#) do not provide equivalent widths with their column density determinations, the continua surrounding the P II $\lambda 1532$ lines in these directions are fairly easy to discern. One exception is that, in our fit to the $\lambda 1532$ line toward HD 99857, we include very weak components at negative velocities, which are seen in the $\lambda 1301$ line but are difficult to discern at $\lambda 1532$. [Lebouteiller et al. \(2005\)](#) apparently assumed that these features were part of the continuum. In general, we typically include many more velocity components in our profile synthesis fits than [Lebouteiller et al. \(2005\)](#) do in theirs. For HD 93222, HD 99857, and HD 104705, we include 6, 8, and 5 components, respectively, while [Lebouteiller et al. \(2005\)](#) include 3, 1, and 3 components. Generally speaking, more components will typically result in smaller b -values and potentially larger column densities. However, this does not seem to explain the significant discrepancies in the P II column densities noted for these three sight lines. If we simply integrate the apparent optical depth profiles of the $\lambda 1532$ lines, a procedure which should yield a lower limit to the true P II column density

(see, e.g., [Savage & Sembach 1991](#)), we find values of $\log N(\text{P II}) = 14.58 \pm 0.02$ toward HD 93222, 14.47 ± 0.02 toward HD 99857, and 14.34 ± 0.02 toward HD 104705. These values are consistent with the results we obtain from profile fitting but are considerably higher than the column densities reported by [Lebouteiller et al. \(2005\)](#).

3.2. Chlorine Column Densities

3.2.1. Neutral Chlorine

Neutral chlorine column densities were obtained (in most cases) from simultaneous profile synthesis fits to the Cl I $\lambda 1347$ line from STIS spectra and one other weaker line. If STIS observations were available covering the Cl I $\lambda 1379$ feature, then this line served as the weaker line in the simultaneous fit. Along many sight lines, the strong Cl I $\lambda 1347$ feature shows weak absorption components displaced in velocity relative to the main, optically-thick absorption component. In such cases, the $\lambda 1379$ line will typically only show absorption from the main component but the line is optically thin (i.e., on the linear portion of the curve of growth). A simultaneous fit to both features therefore allows us to probe the full velocity structure of the Cl I absorption and also provides us with an accurate value for the total column density along the line of sight.

Table 5. Chlorine Column Densities

Star	$W_\lambda(1347)$ (mÅ)	Line ^a	W_λ^a (mÅ)	$\log N(\text{Cl I})$	$W_\lambda(1071)$ (mÅ)	$\log N(\text{Cl II})$	$\log N(\text{Cl}_{\text{tot}})$
HD 108	116.5 ± 0.7	1379	12.5 ± 1.6	14.47 ± 0.04	20.1 ± 3.4	14.28 ± 0.07	14.69 ± 0.04
HD 1383	121.9 ± 0.9	1379	8.4 ± 2.4	14.31 ± 0.05
HD 3827	8.8 ± 1.0	12.57 ± 0.04	7.0 ± 1.9	13.72 ± 0.11	13.75 ± 0.10
HD 12323	79.1 ± 1.4	1379	6.2 ± 1.4	14.17 ± 0.05	10.1 ± 2.9	13.93 ± 0.11	14.36 ± 0.05
HD 13268	132.9 ± 2.0	1379	12.5 ± 2.5	14.48 ± 0.05
HD 13745	122.8 ± 2.3	1379	8.1 ± 2.3	14.28 ± 0.04
HD 14434	124.3 ± 3.1	1379	16.9 ± 3.5	14.64 ± 0.05
HD 15137	107.5 ± 0.8	1097	12.0 ± 6.4	14.14 ± 0.04	13.9 ± 5.6	14.06 ± 0.15	14.40 ± 0.07
HD 23478	35.0 ± 0.2	1379	8.0 ± 0.4	14.33 ± 0.02	< 9.5	< 13.82	...
HD 24190	54.8 ± 0.4	1379	7.0 ± 0.9	14.25 ± 0.04	9.4 ± 1.7	13.87 ± 0.07	14.40 ± 0.04
HD 24534	31.9 ± 0.1	1379	10.9 ± 0.1	14.51 ± 0.02	4.6 ± 2.3	13.55 ± 0.17	14.55 ± 0.03
HD 37903	25.5 ± 0.3	1097	4.7 ± 3.1	13.79 ± 0.08	12.4 ± 3.9	14.04 ± 0.12	14.23 ± 0.09
HD 41161	94.8 ± 0.7	1004	28.2 ± 2.9	13.92 ± 0.02	15.1 ± 4.5	14.06 ± 0.11	14.29 ± 0.07
HD 46223	89.5 ± 0.5	1379	13.3 ± 0.6	14.53 ± 0.02	20.1 ± 4.8	14.23 ± 0.09	14.71 ± 0.04

Table 5 continued

Table 5 (*continued*)

Star	$W_\lambda(1347)$ (mÅ)	Line ^a	W_λ^a (mÅ)	$\log N(\text{Cl I})$	$W_\lambda(1071)$ (mÅ)	$\log N(\text{Cl II})$	$\log N(\text{Cl}_{\text{tot}})$
HD 52266	56.4 ± 0.6	1004	19.2 ± 9.1	13.79 ± 0.04	18.8 ± 10.6	14.20 ± 0.19	14.35 ± 0.15
HD 53975	40.7 ± 0.4		...	13.46 ± 0.02	12.4 ± 7.2	13.97 ± 0.20	14.09 ± 0.16
HD 63005	65.7 ± 1.1	1379	4.7 ± 1.8	14.04 ± 0.06	12.5 ± 3.6	14.06 ± 0.11	14.35 ± 0.07
HD 66788	67.9 ± 1.4	1379	2.2 ± 1.7	13.70 ± 0.03	17.8 ± 5.0	14.15 ± 0.11	14.28 ± 0.08
HD 72754	39.8 ± 0.8		...	13.74 ± 0.05
HD 73882	55.9 ± 0.7	1379	13.6 ± 1.2	14.62 ± 0.04	20.1 ± 7.5	14.25 ± 0.14	14.77 ± 0.05
HD 75309	53.3 ± 0.6	1097	6.2 ± 3.8	13.86 ± 0.05	12.8 ± 3.1	14.02 ± 0.10	14.25 ± 0.06
HD 88115	24.6 ± 0.7		...	13.19 ± 0.04	12.8 ± 1.2	14.09 ± 0.04^b	14.14 ± 0.04
HD 89137	49.9 ± 0.6	1094	19.9 ± 3.1	13.90 ± 0.05	14.9 ± 3.3	14.07 ± 0.09	14.29 ± 0.06
HD 90087	58.9 ± 0.6		...	13.65 ± 0.04	20.3 ± 1.6	14.23 ± 0.03	14.34 ± 0.03
HD 91597	46.2 ± 2.2	1379	$< 6.4^c$	13.45 ± 0.03	31.3 ± 3.0	14.50 ± 0.04	14.54 ± 0.04
HD 91651	52.1 ± 1.4		...	13.52 ± 0.02
HD 91824	67.7 ± 1.2		...	13.80 ± 0.05	15.4 ± 3.2	14.07 ± 0.08	14.26 ± 0.06
HD 91983	64.4 ± 1.0		...	13.79 ± 0.05	17.1 ± 5.6	14.13 ± 0.12	14.29 ± 0.09
HD 92554	51.8 ± 2.8	1379	$< 9.6^c$	13.51 ± 0.03	46.4 ± 7.1	14.70 ± 0.06	14.72 ± 0.06
HD 93129	96.9 ± 0.3	1379	10.0 ± 0.6	14.39 ± 0.02
HD 93205	66.0 ± 0.7	1379	4.2 ± 1.3	13.98 ± 0.06
HD 93222	48.6 ± 0.6	1379	2.0 ± 0.8	13.65 ± 0.04
HD 93843	56.5 ± 0.8		...	13.55 ± 0.03
HD 94493	52.6 ± 0.8		...	13.54 ± 0.03	22.5 ± 2.8	14.26 ± 0.05	14.33 ± 0.04
HD 97175	27.7 ± 0.9		...	13.41 ± 0.04	13.4 ± 4.6	14.08 ± 0.13	14.16 ± 0.11
HD 99857	68.1 ± 0.5	1097	8.2 ± 4.9	13.99 ± 0.06	16.7 ± 3.2	14.32 ± 0.08^b	14.49 ± 0.06
HD 99890	70.7 ± 0.2	1379	2.3 ± 0.3	13.70 ± 0.03	20.6 ± 3.4	14.21 ± 0.07	14.33 ± 0.05
HD 100199	70.7 ± 1.1	1379	13.0 ± 1.5	14.54 ± 0.04
HD 101190	66.2 ± 0.5	1379	10.6 ± 0.4	14.45 ± 0.02
HD 104705	53.4 ± 0.5	1379	4.5 ± 0.7	14.04 ± 0.05
HD 108639	75.5 ± 0.7	1379	4.1 ± 1.0	13.98 ± 0.05
HD 109399	53.7 ± 0.9		...	13.56 ± 0.04	15.4 ± 3.2	14.11 ± 0.08	14.22 ± 0.07
HD 114886	106.9 ± 0.9	1379	7.8 ± 1.3	14.26 ± 0.05
HD 115455	91.5 ± 1.1		...	13.89 ± 0.03
HD 116852	34.1 ± 0.3		...	13.44 ± 0.04	7.4 ± 1.1	13.97 ± 0.07^b	14.08 ± 0.06
HD 121968	6.9 ± 0.3	1379	$< 0.7^c$	12.57 ± 0.03	10.7 ± 1.7	13.96 ± 0.07	13.98 ± 0.06
HD 137595	59.3 ± 0.7	1379	8.2 ± 0.9	14.35 ± 0.04	4.6 ± 2.1	13.53 ± 0.16	14.41 ± 0.04
HD 144965	40.4 ± 0.7	1094	13.2 ± 3.1	13.63 ± 0.04	< 6.8	< 13.67	...
HD 147683	51.1 ± 0.5	1379	10.3 ± 0.7	14.46 ± 0.03	10.4 ± 7.8	13.92 ± 0.24	14.57 ± 0.07
HD 147888	25.8 ± 0.3	1097	5.3 ± 3.4	13.85 ± 0.08	19.2 ± 4.0	14.43 ± 0.09	14.53 ± 0.08
HD 147933 ^d	26.8 ± 0.2	1097	4.1 ± 3.7	13.71 ± 0.08	15.6 ± 3.8	14.31 ± 0.10	14.41 ± 0.09
HD 148422	84.9 ± 1.6	1379	7.2 ± 1.9	14.23 ± 0.05
HD 148937	120.8 ± 0.6	1379	13.2 ± 1.3	14.51 ± 0.03
HD 151805	81.0 ± 1.9	1379	6.6 ± 2.4	14.20 ± 0.05

Table 5 continued

Table 5 (continued)

Star	$W_\lambda(1347)$ (mÅ)	Line ^a	W_λ^a (mÅ)	$\log N(\text{Cl I})$	$W_\lambda(1071)$ (mÅ)	$\log N(\text{Cl II})$	$\log N(\text{Cl}_{\text{tot}})$
HD 152590	71.5 ± 0.3	1379	6.7 ± 1.7	14.22 ± 0.05	18.3 ± 4.3	14.19 ± 0.09	14.51 ± 0.05
HD 156359	7.4 ± 1.1	1379	$< 4.1^c$	12.59 ± 0.06	9.7 ± 3.0	13.93 ± 0.12	13.95 ± 0.11
HD 157857	76.6 ± 0.6	1097	9.4 ± 5.3	14.04 ± 0.05	7.0 ± 4.0	13.72 ± 0.20	14.21 ± 0.08
HD 163522	52.2 ± 1.9	1379	$< 6.2^c$	13.51 ± 0.03
HD 165246	39.2 ± 0.3	1094	18.4 ± 4.1	13.99 ± 0.06	20.7 ± 1.6	14.32 ± 0.04^b	14.49 ± 0.03
HD 165955	30.2 ± 1.5	1379	$< 4.8^c$	13.23 ± 0.03	15.5 ± 2.7	14.13 ± 0.07	14.18 ± 0.06
HD 167402	35.4 ± 1.0	1379	5.3 ± 1.3	14.13 ± 0.07	12.7 ± 4.5	13.98 ± 0.13	14.37 ± 0.07
HD 168076	128.7 ± 1.8	1379	18.0 ± 2.5	14.72 ± 0.04	41.8 ± 17.1	14.60 ± 0.15	14.97 ± 0.07
HD 168941	44.5 ± 1.0	1379	7.1 ± 1.1	14.27 ± 0.05	11.3 ± 2.9	13.95 ± 0.10	14.44 ± 0.05
HD 177989	56.9 ± 0.6	1379	4.8 ± 0.5	14.09 ± 0.04	3.7 ± 2.5	13.42 ± 0.22	14.18 ± 0.06
HD 178487	71.9 ± 1.5	1379	8.7 ± 1.3	14.34 ± 0.05	< 16.7	< 14.07	...
HD 179407	72.6 ± 1.8	1379	8.0 ± 2.6	14.30 ± 0.06	< 21.5	< 14.17	...
HD 185418	67.5 ± 0.4	1097	16.9 ± 2.4	14.38 ± 0.04	< 14.7	< 14.01	...
HD 190918	115.2 ± 1.3	1379	7.6 ± 1.4	14.25 ± 0.04	29.6 ± 3.5	14.38 ± 0.05	14.62 ± 0.03
HD 191877	69.1 ± 0.5	1097	6.2 ± 0.8	13.85 ± 0.03	8.1 ± 1.1	13.78 ± 0.06	14.12 ± 0.03
HD 192035	62.0 ± 2.3	1379	8.4 ± 1.5	14.40 ± 0.06	10.6 ± 4.0	13.93 ± 0.14	14.52 ± 0.06
HD 192639	67.6 ± 0.4	1097	14.3 ± 1.7	14.27 ± 0.04	18.0 ± 3.6	14.22 ± 0.08	14.54 ± 0.04
HD 195455	9.6 ± 0.8		...	12.62 ± 0.03	4.3 ± 3.7	13.49 ± 0.27	13.55 ± 0.24
HD 195965	67.8 ± 0.9	1379	5.1 ± 1.4	14.08 ± 0.06	5.4 ± 0.8	13.59 ± 0.06	14.20 ± 0.05
HD 201345	53.3 ± 0.6		...	13.54 ± 0.03	16.2 ± 1.7	14.12 ± 0.04	14.22 ± 0.03
HD 202347	62.5 ± 0.7	1379	3.3 ± 2.2	13.88 ± 0.04
HD 203374	89.1 ± 0.6	1379	10.4 ± 2.0	14.44 ± 0.05	23.8 ± 2.2	14.29 ± 0.04	14.67 ± 0.04
HD 203938	68.6 ± 0.6	1379	20.1 ± 1.3	14.80 ± 0.03	< 38.3	< 14.42	...
HD 206267	76.2 ± 0.6	1097	9.4 ± 1.2	14.04 ± 0.04	12.9 ± 3.2	14.00 ± 0.10	14.32 ± 0.05
HD 206773	73.1 ± 0.5	1097	12.4 ± 1.5	14.19 ± 0.04	12.0 ± 2.3	13.97 ± 0.08	14.40 ± 0.04
HD 207198	77.1 ± 0.4	1097	12.3 ± 3.7	14.17 ± 0.04	13.8 ± 7.3	14.04 ± 0.18	14.41 ± 0.09
HD 207308	67.5 ± 0.7	1379	15.6 ± 1.1	14.64 ± 0.03	18.3 ± 7.1	14.23 ± 0.14	14.78 ± 0.05
HD 207538	74.9 ± 0.9	1379	14.4 ± 0.6	14.67 ± 0.03	13.9 ± 5.6	14.05 ± 0.15	14.77 ± 0.04
HD 208440	90.5 ± 0.7	1097	9.5 ± 1.8	14.04 ± 0.03	17.1 ± 2.8	14.14 ± 0.07	14.39 ± 0.04
HD 209339	73.5 ± 0.5	1097	7.7 ± 1.3	13.94 ± 0.03	13.5 ± 1.6	14.03 ± 0.05	14.29 ± 0.03
HD 210809	109.6 ± 0.7	1379	4.1 ± 2.4	13.97 ± 0.02
HD 210839	106.2 ± 0.7	1097	12.4 ± 2.3	14.16 ± 0.04	11.8 ± 3.4	14.01 ± 0.11^b	14.39 ± 0.05
HD 212791	62.2 ± 1.0		...	13.65 ± 0.03	11.4 ± 5.5	13.93 ± 0.17	14.11 ± 0.12
HD 218915	77.3 ± 0.4	1379	6.2 ± 1.0	14.16 ± 0.04
HD 219188	40.0 ± 0.3		...	13.45 ± 0.03	11.1 ± 2.2	13.95 ± 0.08	14.07 ± 0.06
HD 220057	40.1 ± 0.7	1097	6.4 ± 1.6	13.89 ± 0.05	6.1 ± 2.6	13.68 ± 0.16	14.10 ± 0.07
HDE 232522	82.2 ± 0.2	1379	5.8 ± 0.5	14.13 ± 0.03
HDE 303308	78.8 ± 0.7	1379	8.5 ± 1.9	14.32 ± 0.05
HDE 308813	76.0 ± 2.1	1379	7.8 ± 2.0	14.30 ± 0.05
BD+35 4258	66.5 ± 2.0	1379	4.4 ± 2.0	14.02 ± 0.06	26.3 ± 4.1	14.35 ± 0.06	14.52 ± 0.05

Table 5 continued

Table 5 (*continued*)

Star	$W_{\lambda}(1347)$	Line ^a	W_{λ} ^a	$\log N(\text{Cl I})$	$W_{\lambda}(1071)$	$\log N(\text{Cl II})$	$\log N(\text{Cl}_{\text{tot}})$
	(mÅ)		(mÅ)		(mÅ)		
BD+53 2820	104.1 ± 2.7	1379	3.6 ± 3.3	13.91 ± 0.04
CPD-59 2603	58.9 ± 0.7	1379	8.5 ± 1.3	14.33 ± 0.05
CPD-59 4552	82.9 ± 1.4		...	13.95 ± 0.04
CPD-69 1743	40.1 ± 2.1	1379	$< 7.1^c$	13.53 ± 0.04

^a Identification and equivalent width of the weak Cl I line used to constrain a simultaneous profile synthesis fit with the $\lambda 1347$ line.

^b A small upward correction has been made to the Cl II column density in this direction to account for blending between the Cl II profile and the nearby H₂ feature.

^c A 3σ upper limit is provided because the equivalent width determined in the fit is less than the associated uncertainty.

^d Data on Cl I $\lambda 1097$ and Cl II $\lambda 1071$ toward HD 147933 (ρ Oph A) are obtained from Copernicus observations.

Our Cl I fits employed the same profile fitting routine as was used to fit the P II lines, except that the two Cl I absorption profiles were fitted simultaneously. This means that the column densities, b -values, and velocities of the individual components included in the fits to the two profiles are necessarily identical, but the best fitting values of the parameters are still determined iteratively through an rms-minimizing approach. The equivalent widths and total Cl I column densities derived through our profile synthesis fits are provided in Table 5 for a total of 98 sight lines. Examples of our simultaneous fits to the Cl I $\lambda 1379$ and $\lambda 1347$ lines are presented in Figures 4 and 5. In a few cases, the $\lambda 1379$ line, although included in the simultaneous fit, is not significantly detected (i.e., the derived equivalent width is smaller than the associated uncertainty). An example of this is provided by the line of sight to HD 121968 (Figure 5). In these situations, we list 3σ upper limits to the equivalent width of the $\lambda 1379$ line in Table 5.

There are 19 sight lines included in Table 5 for which the Cl I $\lambda 1379$ line is not available in the archival STIS data, but the $\lambda 1347$ feature is weak enough that optical depth effects should not be a major concern. In each of these cases, the relative intensity of the $\lambda 1347$ line does not drop below ~ 0.05 and the strongest absorption component retains a Gaussian shape. In other words, the shape of the profile does not appear to be distorted by saturation in the line core. For these 19 sight lines, a profile synthesis fit to the $\lambda 1347$ line alone yielded the total Cl I column density.

There are also a significant number of sight lines where there are no observations covering the Cl I $\lambda 1379$ line and where the $\lambda 1347$ line is much too strong to fit on its own. For many of these sight lines, we use obser-

vations of the Cl I $\lambda 1004$, $\lambda 1094$, or $\lambda 1097$ transition, available from FUSE spectra, to help constrain the Cl I column density. Experimentally determined f -values for the Cl I transitions at 1004.7 \AA and 1094.8 \AA were recently reported by Alkhayat et al. (2019). These f -values, from beam-foil experiments, are in good agreement with the empirical f -values derived for these transitions by Sonnentrucker et al. (2006). A secure experimental f -value is also available for the Cl I $\lambda 1097$ transition (Schectman et al. 1993).

The Cl I $\lambda 1097$ transition is the weakest of the three FUSE transitions mentioned above. We therefore prefer to use this transition to constrain the Cl I column density provided that the line can be reliably measured. In cases where the $\lambda 1097$ line is too weak to detect or is affected by noise in the spectrum, we chose one of the other two lines instead, whichever appeared to provide the most reliable measurement. We then performed a simultaneous profile synthesis fit using the $\lambda 1347$ line from STIS data and whichever FUSE transition was chosen to constrain the total column density. Since the FUSE wavelength scale is known to be rather poorly calibrated, we first corrected the velocity scale of the FUSE spectrum so that the centroid velocity of the Cl I absorption feature was consistent with the (weighted mean) velocity of the $\lambda 1347$ line before proceeding with the simultaneous fit. The velocity shift applied to the FUSE spectrum was calculated either directly from the Cl I $\lambda 1347$ line or from the S I $\lambda 1295$ transition if the $\lambda 1347$ line was too heavily saturated. The S I $\lambda 1295$ transition (from high-resolution STIS spectra) also provided initial values for the component parameters (i.e., the relative velocities, b -values, and component fractions) in cases where the Cl I $\lambda 1347$ line was extremely optically thick. Examples of our simultaneous profile synthesis fits to the Cl I

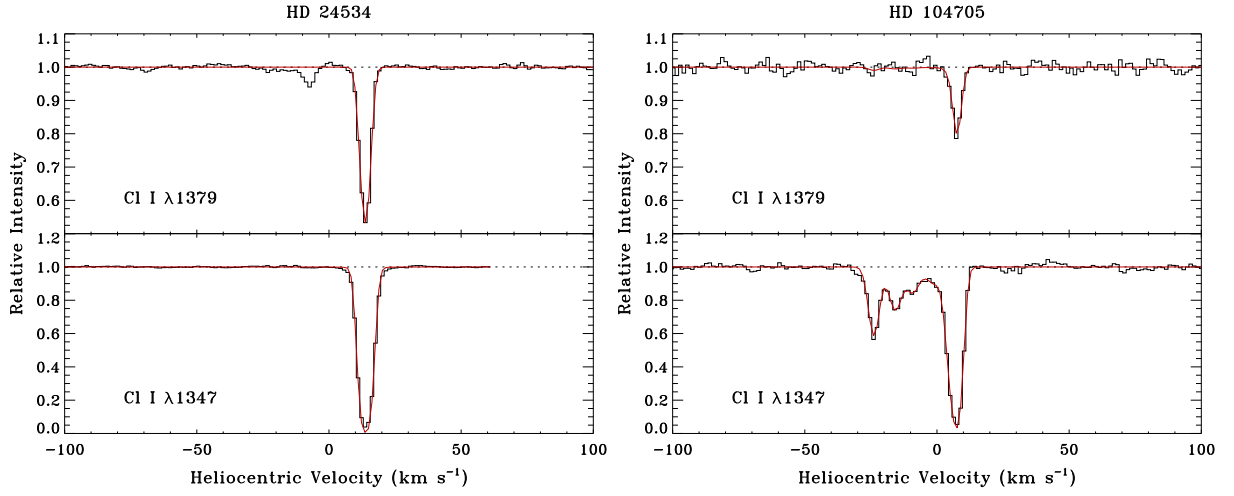


Figure 4. High-resolution STIS spectra in the vicinity of the Cl I $\lambda 1379$ and $\lambda 1347$ lines toward HD 24534 (left panels) and HD 104705 (right panels). Solid red lines represent simultaneous profile synthesis fits to the two Cl I lines in each direction.

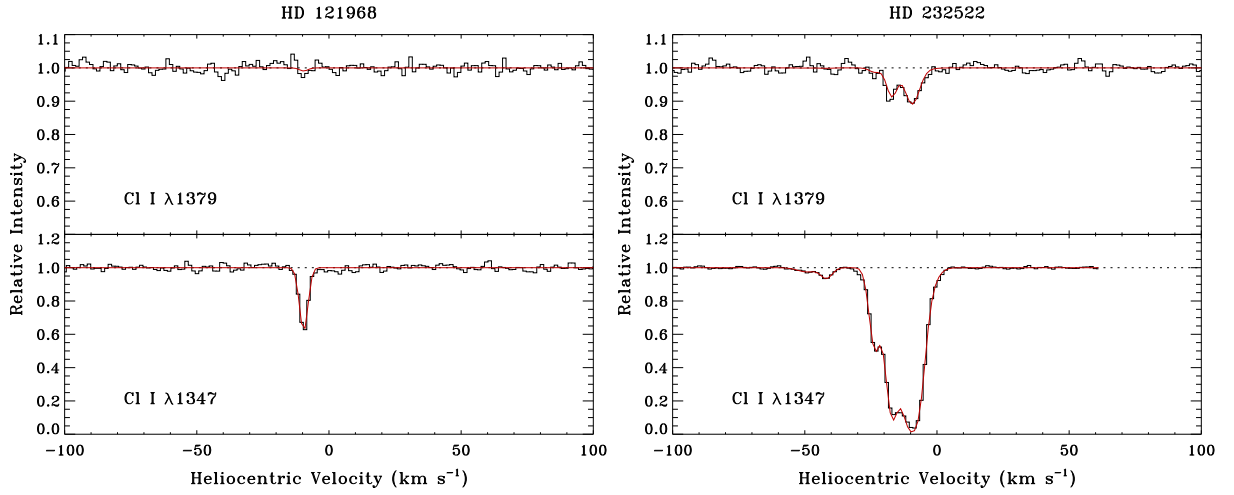


Figure 5. Same as Figure 4 except toward HD 121968 (left panels) and HD 232522 (right panels).

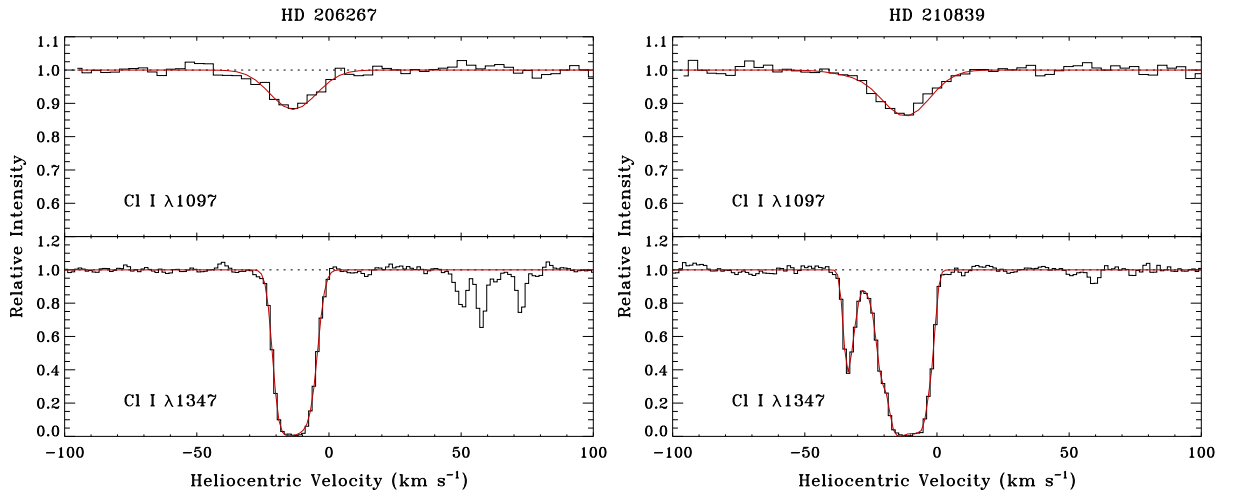


Figure 6. Simultaneous profile synthesis fits to the Cl I $\lambda 1347$ and $\lambda 1097$ lines toward HD 206267 (left panels) and HD 210839 (right panels). The $\lambda 1347$ data are from high-resolution STIS spectra, while the $\lambda 1097$ spectra are from FUSE observations.

$\lambda 1347$ line from STIS spectra and the $\lambda 1097$ feature from FUSE data are provided in Figure 6. The resulting total Cl I column densities are included in Table 5.

3.2.2. Singly Ionized Chlorine

Analysis of the Cl II $\lambda 1071$ feature, obtained from FUSE observations, is complicated by the presence of a nearby H₂ absorption line (as described in Section 2.2). The velocity separation between the Cl II $\lambda 1071$ line and the H₂ (3–0) $R(4)$ line is only 38 km s^{−1}, with the H₂ feature positioned to the blue of the Cl II line. Thus, if the Cl II absorption profile includes components that are blueshifted by ~ 40 km s^{−1} (relative to the main absorption component), then the Cl II profile will be severely blended with H₂ absorption from the main component. Unfortunately, many of the sight lines in our Cl I sample show components that are blueshifted with respect to the main absorption complex (both in the Cl I $\lambda 1347$ line and in lines from dominant ions, such as P II $\lambda 1301$). Typically, sight lines that exhibit multiple absorption complexes at different velocities are those that probe material in a distant spiral arm (such as the Sagittarius-Carina spiral arm or the Perseus spiral arm). In these cases, the absorption complexes at relatively low velocity correspond to material in the “local arm”, whereas the absorption complexes displaced to negative velocities correspond to material in the more distant arm. (One example of this is provided by the Cl I $\lambda 1347$ line toward HD 104705 shown in Figure 4. The absorption near $v_{\odot} \approx -25$ km s^{−1} is associated with diffuse molecular gas in the Sagittarius-Carina spiral arm.)

We do not attempt to derive Cl II column densities along any sight lines where it is likely that the Cl II absorption profile is severely blended with H₂ absorption. In order to determine whether a given sight line exhibits blended absorption, we examined both the Cl I $\lambda 1347$ profile and the P II $\lambda 1301$ and/or $\lambda 1532$ profile. (The H₂ absorption probably closely follows the Cl I absorption, while the Cl II profile should be more similar to that of P II.) We looked for sight lines where most of the absorption was positioned at velocities less than ~ 20 km s^{−1} relative to the deepest part of the absorption profile. Sight lines with prominent absorption complexes located more than ~ 20 km s^{−1} from the main component were rejected.

For sight lines that passed this initial inspection, we still needed to “deblend” the Cl II and H₂ absorption lines. Due to the low resolution of the FUSE spectrograph (~ 18 km s^{−1}), the wings of the Cl II and H₂ lines will be blended even if the intrinsic spread in absorption is rather narrow. To deblend the two features, we started with a simple Voigt profile fit consisting of

two components, one component for the H₂ line and one component for the Cl II feature. We then used the parameters derived for the H₂ component to create a synthetic spectrum that was divided into the observed spectrum, thereby removing the absorption associated with H₂. Any remaining absorption was then attributed to Cl II $\lambda 1071$.

We then proceeded to fit the Cl II $\lambda 1071$ feature with our usual profile fitting routine. However, because the low resolution of the FUSE spectra makes it impossible to discern individual components, we adopted a profile template for the component structure of the Cl II $\lambda 1071$ line based on either the P II $\lambda 1532$ line or the Ge II $\lambda 1237$ feature. Both of these lines (which are available from STIS observations) are expected to have an equivalent width that is comparable to (but somewhat larger than) that of Cl II $\lambda 1071$. Given the difference in the cosmic abundances of P and Cl, and taking into account the different wavelengths and f -values of the two transitions, the expected equivalent width ratio between the $\lambda 1071$ and $\lambda 1532$ lines is $W_{1071}/W_{1532} \approx 0.6$ (assuming optically thin absorption and no differences in depletion). Similarly, the expected ratio between the Cl II $\lambda 1071$ and Ge II $\lambda 1237$ lines is $W_{1071}/W_{1237} \approx 0.5$. By using P II $\lambda 1532$ or Ge II $\lambda 1237$ as a template, we can therefore be reasonably well assured that our fits to the Cl II $\lambda 1071$ feature include all of the absorption components that are likely to be detectable.

For many of our sight lines, profile fitting results were already available for P II $\lambda 1532$. Thus, these served as the basis for fitting the Cl II $\lambda 1071$ feature. In cases where observations of the P II $\lambda 1532$ line were not available, the Ge II $\lambda 1237$ line was used instead. Component structures for Ge II were obtained either from new analyses of the Ge II $\lambda 1237$ line or from the component results published in Ritchey et al. (2018). The relative velocities, b -values, and component fractions (obtained from P II or Ge II) were held fixed in the fit to the Cl II $\lambda 1071$ line. The only free parameters were the total Cl II column density and an overall velocity offset. The equivalent widths and total Cl II column densities derived from these fits are provided in Table 5. Examples of our fits to the H₂ and Cl II features near 1071 Å are presented in Figures 7–9. In these figures, the smooth black curve represents the Voigt profile fit used to deblend and remove the H₂ line, while the red curve indicates the final profile synthesis fit to the Cl II feature. Total chlorine column densities, where $N(\text{Cl}_{\text{tot}}) = N(\text{Cl I}) + N(\text{Cl II})$, are also provided in Table 5.

There are five sight lines where a relatively weak negative velocity absorption component (or group of components) appears in the P II or Ge II absorption pro-

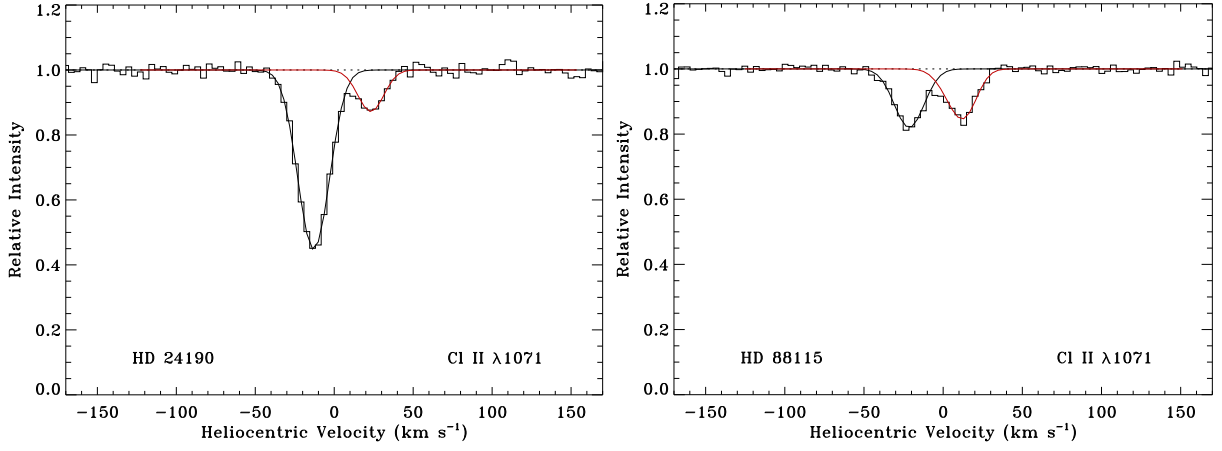


Figure 7. FUSE spectra in the vicinity of the Cl II $\lambda 1071$ line toward HD 24190 (left panel) and HD 88115 (right panel). Solid red lines represent profile synthesis fits to the Cl II feature. The smooth black curves show the Voigt profile fits used to deblend and remove the H₂ lines.

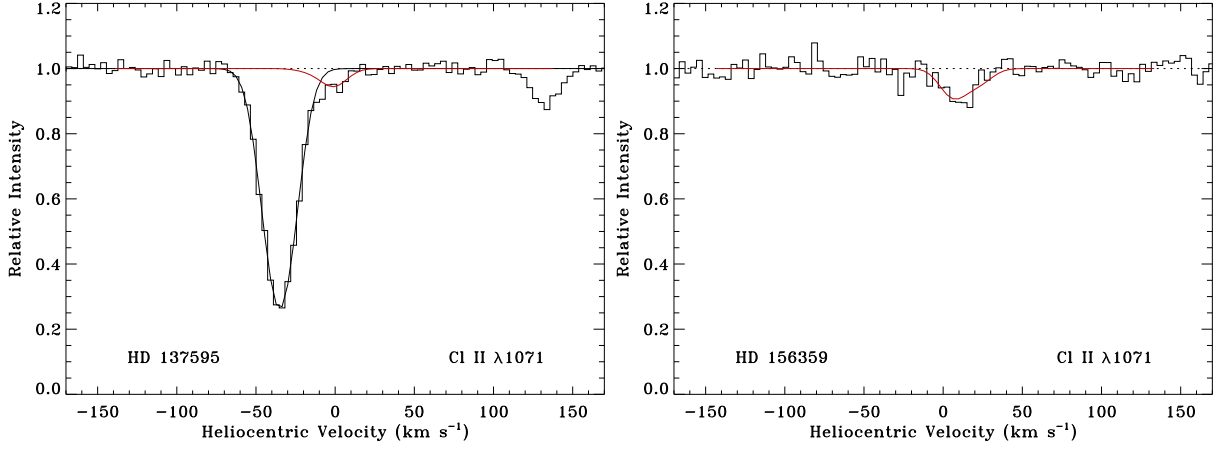


Figure 8. Same as Figure 7 except toward HD 137595 (left panel) and HD 156359 (right panel). Note that the H₂ (3–0) *R*(4) line is not detected toward HD 156359.

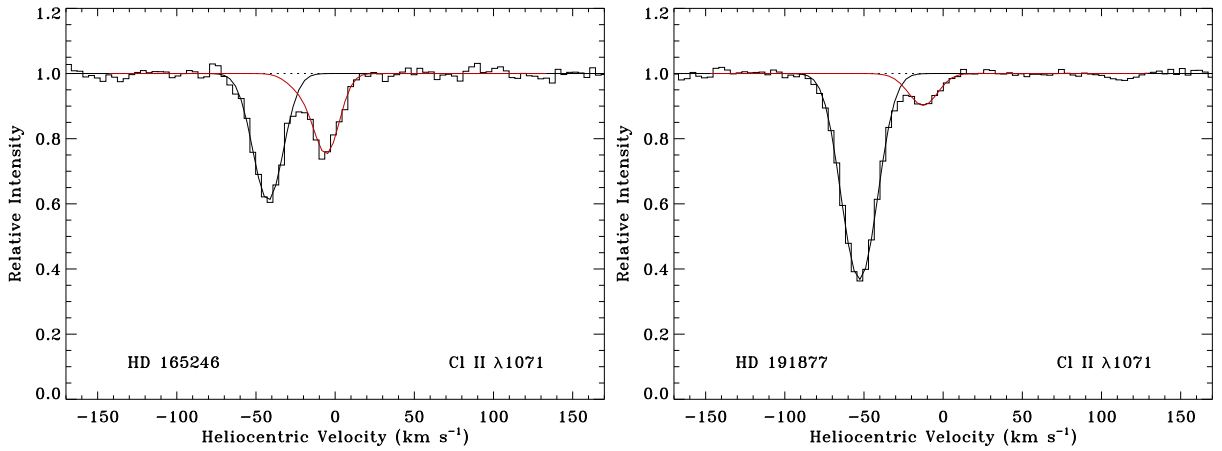


Figure 9. Same as Figure 7 except toward HD 165246 (left panel) and HD 191877 (right panel).

file (at a velocity more than $\sim 20 \text{ km s}^{-1}$ from the main component), but the column density associated with the blueshifted absorption is no more than 20% of the total line-of-sight column density. These cases were initially rejected for exhibiting blended H_2 and Cl II absorption. Ultimately, however, we decided to fit the unblended portion of the Cl II absorption and apply a correction to the resulting column density to account for the “missing” absorption. The magnitude of the correction factor was determined from the fractional column density of the P II or Ge II components not included in the profile fit. These correction factors amounted to upward revisions in the total Cl II column density of 0.08 dex for HD 88115, 0.10 dex for HD 99857, 0.06 dex for HD 116852, 0.02 dex for HD 165246, and 0.05 dex for HD 210839. In most of these cases, the applied correction is comparable to the uncertainty in the Cl II column density obtained from the profile fit.

For six sight lines (HD 23478, HD 144965, HD 178487, HD 179407, HD 185418, and HD 203938), we are unable to derive a Cl II column density, not because the $\text{Cl II } \lambda 1071$ feature is blended with H_2 absorption, but because the Cl II line is not significantly detected. These may be cases where nearly all of the chlorine is in neutral form. We therefore calculated 3σ upper limits to the equivalent width and column density of the $\text{Cl II } \lambda 1071$ feature based on an assumed component structure (from the observed P II line). These limits are provided in Table 5. Unfortunately, none of the derived Cl II upper limits are low enough that the Cl II column density can

be neglected in deriving a total chlorine abundance. We therefore do not provide total Cl column densities for these sight lines.

3.3. Atomic and Molecular Hydrogen Column Densities

Column densities of atomic and molecular hydrogen for the sight lines in our combined phosphorus and chlorine sample were obtained either from Jenkins (2019) or from the values tabulated in Jenkins (2009). These values are provided in Table 6 along with the total hydrogen column densities, $N(\text{H}_{\text{tot}}) = N(\text{H I}) + 2N(\text{H}_2)$, and molecular hydrogen fractions, $f(\text{H}_2) = 2N(\text{H}_2)/N(\text{H}_{\text{tot}})$. For the line of sight to HD 165955, Jenkins (2009) reports a molecular hydrogen column density of $\log N(\text{H}_2) = 16.53 \pm 0.04$. This value was originally derived by Cartledge et al. (2004). However, based on the Cl I column density we obtain for this sight line, $\log N(\text{Cl I}) = 13.23 \pm 0.03$, and the correlations discussed in the next section, the reported value of $N(\text{H}_2)$ toward HD 165955 appears to be much too low. We therefore undertook our own analysis of the FUSE data in this direction to determine a more accurate value for the molecular hydrogen column density. From an analysis of the $J = 0$ and 1 lines of the H_2 (1–0), (2–0), (3–0), and (4–0) bands³, we find $\log N(\text{H}_2) = 19.09 \pm 0.07$. A representative fit to the (4–0) band is presented in Figure 10.

Table 6. Atomic and Molecular Hydrogen Column Densities

Star	$\log N(\text{H I})$	$\log N(\text{H}_2)$	$\log N(\text{H}_{\text{tot}})$	$\log f(\text{H}_2)$	F_*^{a}	Ref.
HD 108	21.38 ± 0.05	20.45 ± 0.08	$21.47^{+0.04}_{-0.05}$	-0.72 ± 0.09	0.53 ± 0.04	1
HD 1383	21.46 ± 0.05	20.49 ± 0.07	$21.54^{+0.04}_{-0.05}$	-0.75 ± 0.08	0.48 ± 0.05	1
HD 3827	20.55 ± 0.07	18.35 ± 0.25	$20.56^{+0.07}_{-0.08}$	-1.90 ± 0.25	0.41 ± 0.07	1
HD 12323	21.19 ± 0.04	20.26 ± 0.08	$21.28^{+0.04}_{-0.04}$	-0.72 ± 0.09	0.51 ± 0.05	1
HD 13268	21.34 ± 0.07	20.46 ± 0.08	$21.44^{+0.06}_{-0.07}$	-0.68 ± 0.10	0.45 ± 0.07	1
HD 13745	21.34 ± 0.05	20.53 ± 0.07	$21.46^{+0.04}_{-0.05}$	-0.63 ± 0.08	0.55 ± 0.05	1
HD 14434	21.37 ± 0.09	20.47 ± 0.07	$21.47^{+0.07}_{-0.09}$	-0.70 ± 0.10	0.52 ± 0.04	2
HD 15137	21.24 ± 0.08	20.23 ± 0.08	$21.32^{+0.07}_{-0.08}$	-0.79 ± 0.10	0.36 ± 0.06	1
HD 23478	20.71 ± 0.17	20.48 ± 0.07	$21.05^{+0.09}_{-0.12}$	-0.27 ± 0.11	0.00 ± 0.50	2
HD 24190	21.18 ± 0.06	20.38 ± 0.07	$21.30^{+0.05}_{-0.06}$	-0.62 ± 0.08	0.63 ± 0.24	2

Table 6 continued

³ For the analysis of H_2 absorption toward HD 165955, we used the IDL-based program H2GUI, which was originally created and used by Tumlinson et al. (2002).

Table 6 (continued)

Star	$\log N(\text{H I})$	$\log N(\text{H}_2)$	$\log N(\text{H}_{\text{tot}})$	$\log f(\text{H}_2)$	F_*^a	Ref.
HD 24534	20.73 ± 0.06	20.92 ± 0.04	$21.34^{+0.03}_{-0.04}$	-0.12 ± 0.05	0.90 ± 0.06	2
HD 25443	21.29 ± 0.06	20.92 ± 0.08	$21.56^{+0.05}_{-0.06}$	-0.34 ± 0.09	0.72 ± 0.05	1
HD 37903	21.12 ± 0.10	20.85 ± 0.07	$21.44^{+0.06}_{-0.07}$	-0.29 ± 0.09	1.15 ± 0.03	2
HD 41161	21.09 ± 0.05	19.99 ± 0.09	$21.15^{+0.05}_{-0.05}$	-0.86 ± 0.10	0.35 ± 0.04	1
HD 46223	21.46 ± 0.04	20.67 ± 0.06	$21.58^{+0.03}_{-0.04}$	-0.61 ± 0.07	0.86 ± 0.03	1
HD 52266	21.22 ± 0.04	20.00 ± 0.08	$21.27^{+0.04}_{-0.04}$	-0.97 ± 0.09	0.56 ± 0.05	1
HD 53975	21.08 ± 0.04	19.15 ± 0.09	$21.09^{+0.04}_{-0.04}$	-1.64 ± 0.10	0.38 ± 0.03	1
HD 63005	21.24 ± 0.03	20.17 ± 0.09	$21.31^{+0.03}_{-0.03}$	-0.84 ± 0.09	0.68 ± 0.04	1
HD 66788	21.23 ± 0.04	19.72 ± 0.14	$21.26^{+0.04}_{-0.04}$	-1.24 ± 0.14	0.55 ± 0.04	1
HD 72754	21.17 ± 0.12	20.35 ± 0.10	$21.28^{+0.10}_{-0.13}$	-0.63 ± 0.13	0.76 ± 0.10	2
HD 73882	21.11 ± 0.11	21.08 ± 0.10	$21.57^{+0.08}_{-0.09}$	-0.19 ± 0.12	0.68 ± 0.07	2
HD 75309	21.10 ± 0.03	20.16 ± 0.06	$21.19^{+0.03}_{-0.03}$	-0.73 ± 0.07	0.58 ± 0.04	1
HD 79186	21.18 ± 0.09	20.72 ± 0.09	$21.41^{+0.07}_{-0.08}$	-0.39 ± 0.11	0.69 ± 0.03	2
HD 88115	21.03 ± 0.06	19.25 ± 0.14	$21.04^{+0.06}_{-0.07}$	-1.49 ± 0.15	0.39 ± 0.08	1
HD 89137	21.03 ± 0.07	20.02 ± 0.09	$21.11^{+0.06}_{-0.07}$	-0.79 ± 0.11	0.45 ± 0.04	1
HD 90087	21.19 ± 0.05	19.88 ± 0.07	$21.23^{+0.05}_{-0.05}$	-1.05 ± 0.08	0.36 ± 0.07	1
HD 91597	21.40 ± 0.06	19.70 ± 0.05	$21.42^{+0.06}_{-0.07}$	-1.42 ± 0.07	0.44 ± 0.05	2
HD 91651	21.15 ± 0.06	19.07 ± 0.03	$21.16^{+0.06}_{-0.07}$	-1.79 ± 0.07	0.27 ± 0.04	2
HD 91824	21.12 ± 0.04	19.81 ± 0.09	$21.16^{+0.04}_{-0.04}$	-1.05 ± 0.10	0.33 ± 0.04	1
HD 91983	21.15 ± 0.06	20.10 ± 0.07	$21.22^{+0.05}_{-0.06}$	-0.82 ± 0.09	0.31 ± 0.05	1
HD 92554	21.34 ± 0.09	19.24 ± 0.07	$21.35^{+0.09}_{-0.11}$	-1.81 ± 0.11	0.15 ± 0.10	1
HD 93129	21.47 ± 0.07	20.21 ± 0.07	$21.52^{+0.06}_{-0.07}$	-1.00 ± 0.09	0.49 ± 0.05	1
HD 93205	21.36 ± 0.05	19.73 ± 0.12	$21.38^{+0.05}_{-0.05}$	-1.35 ± 0.13	0.33 ± 0.05	1
HD 93222	21.47 ± 0.03	19.77 ± 0.09	$21.49^{+0.03}_{-0.03}$	-1.42 ± 0.09	0.33 ± 0.04	1
HD 93843	21.30 ± 0.05	19.62 ± 0.10	$21.32^{+0.05}_{-0.05}$	-1.40 ± 0.11	0.50 ± 0.04	1
HD 94493	21.10 ± 0.06	20.09 ± 0.06	$21.18^{+0.05}_{-0.06}$	-0.79 ± 0.08	0.32 ± 0.05	1
HD 97175	20.96 ± 0.06	20.10 ± 0.09	$21.07^{+0.05}_{-0.06}$	-0.66 ± 0.10	0.49 ± 0.05	1
HD 99857	21.27 ± 0.07	20.30 ± 0.05	$21.35^{+0.06}_{-0.07}$	-0.75 ± 0.08	0.45 ± 0.05	1
HD 99890	21.12 ± 0.05	19.56 ± 0.09	$21.14^{+0.05}_{-0.05}$	-1.28 ± 0.10	0.16 ± 0.05	1
HD 100199	21.18 ± 0.06	20.15 ± 0.08	$21.25^{+0.05}_{-0.06}$	-0.80 ± 0.09	0.41 ± 0.09	1
HD 101190	21.24 ± 0.03	20.43 ± 0.04	$21.36^{+0.02}_{-0.03}$	-0.63 ± 0.05	0.51 ± 0.05	1
HD 103779	21.17 ± 0.05	19.90 ± 0.08	$21.21^{+0.05}_{-0.05}$	-1.01 ± 0.09	0.29 ± 0.05	1
HD 104705	21.15 ± 0.06	20.02 ± 0.07	$21.21^{+0.05}_{-0.06}$	-0.89 ± 0.09	0.40 ± 0.05	1
HD 108639	21.36 ± 0.04	20.01 ± 0.10	$21.40^{+0.04}_{-0.04}$	-1.09 ± 0.11	0.34 ± 0.04	1
HD 109399	21.11 ± 0.05	20.01 ± 0.09	$21.17^{+0.05}_{-0.05}$	-0.86 ± 0.10	0.44 ± 0.05	1
HD 114886	21.34 ± 0.06	20.30 ± 0.07	$21.41^{+0.05}_{-0.06}$	-0.81 ± 0.09	0.47 ± 0.05	1
HD 115455	21.38 ± 0.05	20.55 ± 0.07	$21.49^{+0.04}_{-0.05}$	-0.64 ± 0.08	0.41 ± 0.06	1
HD 116852	20.96 ± 0.04	19.75 ± 0.09	$21.01^{+0.04}_{-0.04}$	-0.96 ± 0.10	0.48 ± 0.04	1
HD 121968	20.58 ± 0.12	18.70 ± 0.10	$20.59^{+0.12}_{-0.16}$	-1.59 ± 0.15	0.26 ± 0.06	2
HD 122879	21.31 ± 0.06	20.33 ± 0.07	$21.39^{+0.05}_{-0.06}$	-0.76 ± 0.08	0.51 ± 0.04	1
HD 124314	21.41 ± 0.06	20.41 ± 0.09	$21.49^{+0.05}_{-0.06}$	-0.78 ± 0.10	0.47 ± 0.05	1

Table 6 continued

Table 6 (*continued*)

Star	$\log N(\text{H I})$	$\log N(\text{H}_2)$	$\log N(\text{H}_{\text{tot}})$	$\log f(\text{H}_2)$	F_*^{a}	Ref.
HD 137595	20.97 ± 0.06	20.59 ± 0.06	$21.23^{+0.04}_{-0.05}$	-0.34 ± 0.07	0.85 ± 0.05	1
HD 144965	20.97 ± 0.09	20.74 ± 0.07	$21.31^{+0.06}_{-0.07}$	-0.27 ± 0.09	1.07 ± 0.09	1
HD 147683	21.20 ± 0.15	20.68 ± 0.12	$21.41^{+0.11}_{-0.14}$	-0.42 ± 0.15	0.56 ± 0.47	2
HD 147888	21.68 ± 0.08	20.45 ± 0.05	$21.73^{+0.07}_{-0.09}$	-0.98 ± 0.09	1.15 ± 0.12	1
HD 147933	21.63 ± 0.09	20.57 ± 0.15	$21.70^{+0.08}_{-0.10}$	-0.83 ± 0.16	1.09 ± 0.08	2
HD 148422	21.24 ± 0.09	20.15 ± 0.11	$21.31^{+0.08}_{-0.10}$	-0.85 ± 0.13	0.21 ± 0.09	1
HD 148937	21.48 ± 0.06	20.68 ± 0.06	$21.60^{+0.05}_{-0.05}$	-0.62 ± 0.08	0.56 ± 0.07	1
HD 151805	21.33 ± 0.05	20.35 ± 0.07	$21.41^{+0.04}_{-0.05}$	-0.76 ± 0.08	0.54 ± 0.04	1
HD 152590	21.37 ± 0.07	20.47 ± 0.10	$21.47^{+0.06}_{-0.07}$	-0.70 ± 0.11	0.52 ± 0.05	1
HD 156359	20.80 ± 0.10	18.07 ± 0.21	$20.80^{+0.10}_{-0.13}$	-2.43 ± 0.22	0.24 ± 0.09	1
HD 157857	21.26 ± 0.09	20.68 ± 0.10	$21.44^{+0.07}_{-0.08}$	-0.46 ± 0.12	0.62 ± 0.04	2
HD 163522	21.14 ± 0.08	19.66 ± 0.19	$21.17^{+0.08}_{-0.09}$	-1.21 ± 0.20	0.34 ± 0.08	1
HD 165246	21.41 ± 0.03	20.14 ± 0.07	$21.45^{+0.03}_{-0.03}$	-1.01 ± 0.07	0.78 ± 0.04	1
HD 165955	21.10 ± 0.06	$19.09 \pm 0.07^{\text{b}}$	$21.11^{+0.06}_{-0.07}$	-1.72 ± 0.09	0.42 ± 0.04	2
HD 167402	21.13 ± 0.05	20.06 ± 0.10	$21.20^{+0.05}_{-0.05}$	-0.84 ± 0.11	0.25 ± 0.07	1
HD 168076	21.65 ± 0.23	20.68 ± 0.08	$21.73^{+0.20}_{-0.37}$	-0.75 ± 0.21	0.68 ± 0.17	2
HD 168941	21.18 ± 0.05	20.11 ± 0.08	$21.25^{+0.04}_{-0.05}$	-0.84 ± 0.09	0.68 ± 0.06	1
HD 170740	21.09 ± 0.06	20.86 ± 0.08	$21.43^{+0.05}_{-0.06}$	-0.27 ± 0.09	0.87 ± 0.09	1
HD 177989	20.99 ± 0.05	20.16 ± 0.12	$21.10^{+0.05}_{-0.05}$	-0.64 ± 0.13	0.66 ± 0.05	1
HD 178487	21.22 ± 0.04	20.51 ± 0.09	$21.36^{+0.04}_{-0.04}$	-0.55 ± 0.10	0.74 ± 0.07	1
HD 179407	21.20 ± 0.06	20.23 ± 0.09	$21.28^{+0.05}_{-0.06}$	-0.75 ± 0.10	0.63 ± 0.09	1
HD 185418	21.19 ± 0.05	20.72 ± 0.07	$21.41^{+0.04}_{-0.05}$	-0.39 ± 0.08	0.74 ± 0.04	1
HD 190918	21.38 ± 0.06	19.84 ± 0.08	$21.40^{+0.06}_{-0.07}$	-1.26 ± 0.10	0.46 ± 0.03	2
HD 191877	21.03 ± 0.05	20.00 ± 0.17	$21.10^{+0.05}_{-0.06}$	-0.80 ± 0.17	0.53 ± 0.05	1
HD 192035	21.20 ± 0.04	20.63 ± 0.09	$21.39^{+0.04}_{-0.05}$	-0.46 ± 0.10	0.74 ± 0.07	1
HD 192639	21.29 ± 0.09	20.73 ± 0.10	$21.48^{+0.07}_{-0.08}$	-0.45 ± 0.12	0.64 ± 0.04	2
HD 195455	20.61 ± 0.04	18.42 ± 0.19	$20.62^{+0.04}_{-0.04}$	-1.89 ± 0.19	0.39 ± 0.07	1
HD 195965	20.92 ± 0.05	20.28 ± 0.08	$21.08^{+0.04}_{-0.05}$	-0.50 ± 0.09	0.45 ± 0.05	1
HD 198478	21.32 ± 0.12	20.76 ± 0.33	$21.51^{+0.16}_{-0.26}$	-0.45 ± 0.35	0.75 ± 0.14	1
HD 198781	20.93 ± 0.07	20.48 ± 0.08	$21.16^{+0.05}_{-0.06}$	-0.38 ± 0.09	0.79 ± 0.05	1
HD 201345	21.00 ± 0.05	19.36 ± 0.12	$21.02^{+0.05}_{-0.05}$	-1.36 ± 0.13	0.34 ± 0.06	1
HD 202347	20.83 ± 0.08	19.98 ± 0.10	$20.94^{+0.07}_{-0.08}$	-0.66 ± 0.12	0.66 ± 0.08	1
HD 203374	21.20 ± 0.05	20.67 ± 0.07	$21.40^{+0.04}_{-0.05}$	-0.43 ± 0.08	0.66 ± 0.04	1
HD 203938	21.48 ± 0.15	21.00 ± 0.06	$21.70^{+0.10}_{-0.13}$	-0.40 ± 0.11	0.99 ± 0.64	2
HD 206267	21.22 ± 0.06	20.85 ± 0.08	$21.49^{+0.05}_{-0.06}$	-0.34 ± 0.09	0.80 ± 0.05	1
HD 206773	21.09 ± 0.07	20.41 ± 0.06	$21.24^{+0.05}_{-0.06}$	-0.53 ± 0.08	0.60 ± 0.04	1
HD 207198	21.28 ± 0.07	20.79 ± 0.05	$21.50^{+0.05}_{-0.05}$	-0.41 ± 0.07	0.80 ± 0.05	1
HD 207308	21.20 ± 0.06	20.80 ± 0.06	$21.45^{+0.04}_{-0.05}$	-0.35 ± 0.07	0.82 ± 0.05	1
HD 207538	21.27 ± 0.06	20.85 ± 0.06	$21.52^{+0.04}_{-0.05}$	-0.36 ± 0.07	0.85 ± 0.05	1
HD 208440	21.24 ± 0.06	20.28 ± 0.11	$21.33^{+0.05}_{-0.06}$	-0.75 ± 0.12	0.65 ± 0.05	1
HD 209339	21.20 ± 0.04	20.13 ± 0.06	$21.27^{+0.04}_{-0.04}$	-0.84 ± 0.07	0.50 ± 0.05	1

Table 6 continued

Table 6 (continued)

Star	$\log N(\text{H I})$	$\log N(\text{H}_2)$	$\log N(\text{H}_{\text{tot}})$	$\log f(\text{H}_2)$	F_*^a	Ref.
HD 210809	21.31 ± 0.06	19.97 ± 0.12	$21.35^{+0.06}_{-0.06}$	-1.08 ± 0.13	0.31 ± 0.06	1
HD 210839	21.24 ± 0.05	20.80 ± 0.05	$21.48^{+0.04}_{-0.04}$	-0.38 ± 0.06	0.78 ± 0.04	1
HD 212791	21.11 ± 0.12	19.42 ± 0.11	$21.13^{+0.12}_{-0.16}$	-1.41 ± 0.15	0.57 ± 0.08	2
HD 218915	21.20 ± 0.07	20.16 ± 0.06	$21.27^{+0.06}_{-0.07}$	-0.81 ± 0.08	0.39 ± 0.06	1
HD 219188	20.72 ± 0.07	19.38 ± 0.11	$20.76^{+0.07}_{-0.08}$	-1.08 ± 0.12	0.37 ± 0.06	1
HD 220057	20.95 ± 0.14	20.27 ± 0.09	$21.10^{+0.11}_{-0.14}$	-0.53 ± 0.13	0.69 ± 0.13	1
HD 224151	21.35 ± 0.05	20.55 ± 0.06	$21.47^{+0.04}_{-0.05}$	-0.62 ± 0.07	0.49 ± 0.05	1
HDE 232522	21.12 ± 0.04	20.18 ± 0.08	$21.21^{+0.04}_{-0.04}$	-0.73 ± 0.09	0.41 ± 0.04	1
HDE 303308	21.41 ± 0.03	20.20 ± 0.05	$21.46^{+0.03}_{-0.03}$	-0.96 ± 0.06	0.42 ± 0.05	1
HDE 308813	21.20 ± 0.06	20.23 ± 0.07	$21.28^{+0.05}_{-0.06}$	-0.75 ± 0.08	0.52 ± 0.06	1
BD+35 4258	21.24 ± 0.03	19.61 ± 0.11	$21.26^{+0.03}_{-0.03}$	-1.35 ± 0.11	0.38 ± 0.06	1
BD+53 2820	21.35 ± 0.05	20.10 ± 0.11	$21.40^{+0.05}_{-0.05}$	-1.00 ± 0.12	0.44 ± 0.07	1
CPD−59 2603	21.43 ± 0.04	20.02 ± 0.12	$21.46^{+0.04}_{-0.04}$	-1.14 ± 0.12	0.51 ± 0.05	1
CPD−59 4552	21.28 ± 0.05	20.45 ± 0.08	$21.39^{+0.04}_{-0.05}$	-0.64 ± 0.09	0.40 ± 0.05	1
CPD−69 1743	21.16 ± 0.04	19.85 ± 0.15	$21.20^{+0.04}_{-0.04}$	-1.05 ± 0.15	0.40 ± 0.07	1

^aSight line depletion factor.

^bThe H_2 column density derived by [Cartledge et al. \(2004\)](#), and adopted in [Jenkins \(2009\)](#), for the line of sight to HD 165955 is too low. The value listed here is from our own analysis of the H_2 data in this direction.

References—(1) [Jenkins \(2019\)](#), (2) [Jenkins \(2009\)](#).

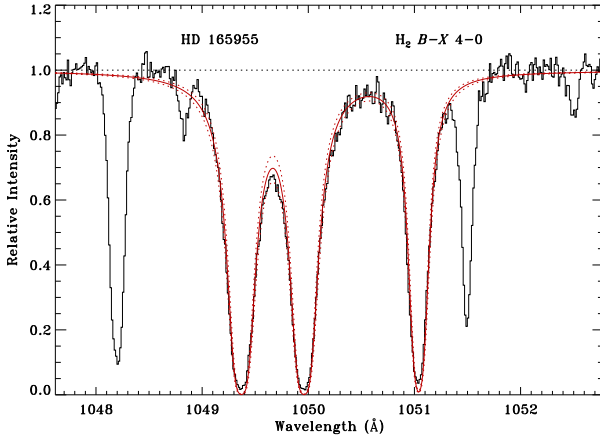


Figure 10. Determination of $N(\text{H}_2)$ toward HD 165955. A synthetic spectrum (red curve) is compared to observations of the $R(0)$, $R(1)$, and $P(1)$ lines of the $B-X$ (4–0) band. The solid red curve corresponds to a total H_2 column density of $\log N(\text{H}_2) = 19.09$, while the dashed red curves indicate variations in the column density of ± 0.07 dex.

4. ANALYSIS

4.1. Column Density Correlations

Owing to the unique chemistry that links neutral chlorine to molecular hydrogen, the column densities of

Cl I and H_2 have long been expected to be well correlated (e.g., [Jura & York 1978](#); [Harris & Bromage 1984](#); [Moomey et al. 2012](#)). Most recently, [Moomey et al. \(2012\)](#), using Cl I measurements from the Copernicus satellite, found a correlation between $N(\text{Cl I})$ and $N(\text{H}_2)$ that had a slope of 0.92 ± 0.19 (in log-log space) and a correlation coefficient greater than 0.6. [Balashev et al. \(2015\)](#) found that a similar relationship holds for high-redshift damped Lyman- α (DLA) systems where both H_2 and Cl I are detected. Other correlations, such as that between $N(\text{Cl}_{\text{tot}})$ and $N(\text{H}_{\text{tot}})$, have also been noted in the literature ([Harris & Bromage 1984](#); [Moomey et al. 2012](#)). In light of our greatly expanded sample of Cl I and Cl II column densities (Table 5), it is worthwhile to revisit these correlations.

In Figure 11, we compare our new determinations of neutral chlorine column densities (from STIS and FUSE observations) with the corresponding molecular hydrogen column densities from Table 6. Also included in Figure 11 are the Cl I measurements obtained in previous studies based on Copernicus observations ([Moomey et al. 2012](#); [Brown 2015](#))⁴ and the Cl I and

⁴ [Brown \(2015\)](#) derived Cl I and Cl II column densities from Copernicus observations for a sample of sight lines with very low

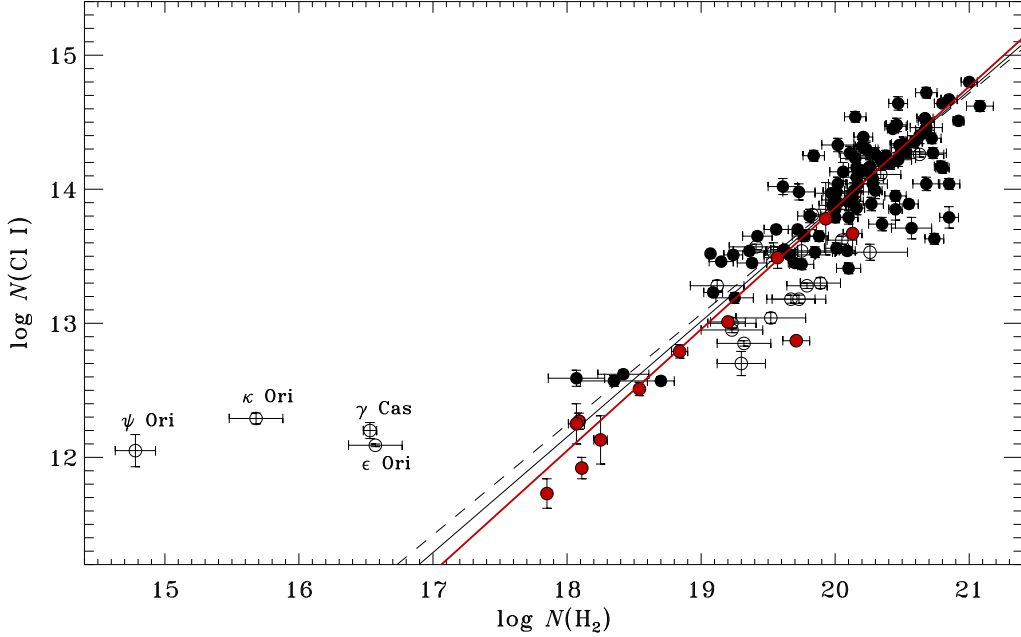


Figure 11. Correlation between $\log N(\text{Cl I})$ and $\log N(\text{H}_2)$. Solid black circles represent chlorine measurements obtained in this investigation from STIS and FUSE observations; open circles represent measurements obtained in previous studies from Copernicus observations (Moomey et al. 2012; Brown 2015). Solid red circles represent Cl I and H_2 measurements obtained for high-redshift absorption systems toward background quasars (Balashev et al. 2015). The dashed black line represents a least-squares linear fit to the STIS+FUSE sample, while the solid black line indicates a linear fit to the entire Galactic sample (excluding the four discrepant sight lines with very low H_2 column densities). The solid red line shows a least-squares linear fit to the combined Galactic and extragalactic sample (excluding the four outliers).

H_2 column densities derived for high-redshift absorption systems toward background quasars (Balashev et al. 2015). A strong correlation between $N(\text{Cl I})$ and $N(\text{H}_2)$ is found for Galactic sight lines with $\log N(\text{H}_2) \gtrsim 18$. Least-squares linear fits⁵ to the “STIS+FUSE” sample and the sample that also includes Copernicus measurements (“all Galactic”) yield linear correlation coefficients of ~ 0.8 and slopes of ~ 0.8 – 0.9 (see Figure 11 and Table 7), consistent with the results of Moomey et al. (2012). Four sight lines with $\log N(\text{H}_2) < 17$ do not follow the trend exhibited by the other Galactic sight lines and are not included in the linear fits.

As already discussed by Balashev et al. (2015), the relationship between Cl I and H_2 exhibited by high-redshift DLAs is very similar to that found for Galactic sight lines. A least-squares linear fit to the combined Galactic and extragalactic sample (“Galactic+DLAs”) yields a slope of 0.906 ± 0.012 and a linear correlation

coefficient of 0.897 (Table 7). The extragalactic measurements help to extend the trend of Cl I versus H_2 to lower neutral chlorine column densities (i.e., below $\log N(\text{Cl I}) \sim 12.5$). The only Galactic sight lines with such low values of $N(\text{Cl I})$ (i.e., γ Cas, ψ Ori, ϵ Ori, and κ Ori) have H_2 column densities that are much lower than the values that would be predicted by the linear trends. These sight lines probe molecular gas in the transition region where H_2 is not yet fully self-shielded. A similar pattern is seen when the column densities of other trace neutral species (e.g., K I and Na I) are plotted versus $N(\text{H}_2)$ (Welty & Hobbs 2001). The K I and Na I column densities examined by Welty & Hobbs (2001) exhibit a plateau for molecular hydrogen column densities in the range $15 \lesssim \log N(\text{H}_2) \lesssim 19$ (see their Figures 26 and 27).

Welty & Hobbs (2001) find nearly linear relationships for $N(\text{K I})$ versus $N(\text{H}_2)$ and $N(\text{Na I})$ versus $N(\text{H}_2)$ for $\log N(\text{H}_2) > 18.5$, very similar to our findings for Cl I. The fact that the slope of the relationship between $N(\text{Cl I})$ and $N(\text{H}_2)$ in the high column density regime is slightly less than one is most likely related to the increase in the fraction of hydrogen in molecular form in the portion of the cloud where the H_2 resides. As discussed below (see Section 4.3), the gas-phase abundance (i.e., depletion) of chlorine shows very little dependence

H_2 column densities as part of a Masters Thesis at the University of Toledo. For convenience, the Copernicus measurements of Moomey et al. (2012) and Brown (2015) are compiled in Appendix A.

⁵ The least-squares linear fits described in this paper were performed using the IDL procedure FITEXY, which accounts for uncertainties in both the x and y coordinates (Press et al. 2007).

Table 7. Column Density Correlations

Y	X	A	B	r^a	N^b	Sample
Cl I	H_2	0.824 ± 0.016	-2.59 ± 0.31	0.840	98	STIS+FUSE
		0.862 ± 0.015	-3.37 ± 0.31	0.841	118	all Galactic ^c
		0.906 ± 0.012	-4.26 ± 0.23	0.897	130	Galactic+DLAs ^c
Cl I	H_{tot}	2.862 ± 0.106	-46.96 ± 2.25	0.731	98	STIS+FUSE
		2.478 ± 0.061	-38.74 ± 1.29	0.828	119	all Galactic
Cl _{tot}	H_{tot}	1.065 ± 0.057	-8.26 ± 1.21	0.845	62	STIS+FUSE
		1.030 ± 0.022	-7.52 ± 0.45	0.931	88	all Galactic

NOTE— $\log N(Y) = B + A \times \log N(X)$

^aLinear correlation coefficient.

^bNumber of sight lines in the sample.

^cExcludes outliers: γ Cas, ψ Ori, ϵ Ori, and κ Ori.

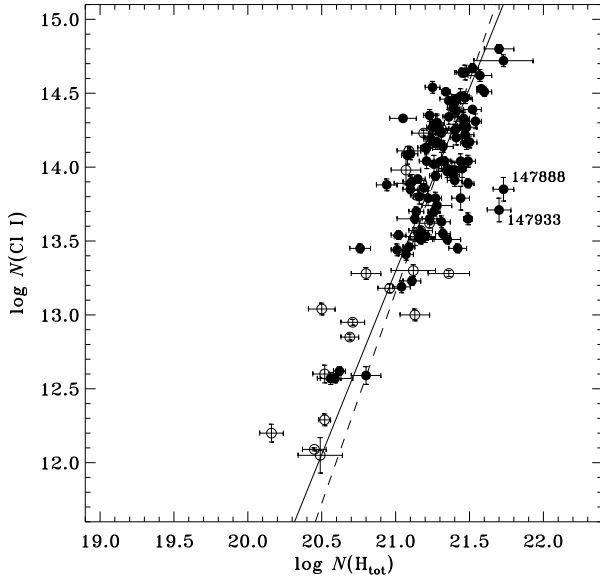


Figure 12. Correlation between $\log N(\text{Cl I})$ and $\log N(H_{\text{tot}})$. The plotting symbols have the same meaning as in Figure 11. Two sight lines with anomalously low Cl I column densities are identified. (These sight lines were not excluded from the linear fits.)

on the molecular hydrogen fraction. Thus, while the ratio of neutral chlorine to total hydrogen remains roughly constant in the molecular portion of the cloud, the fraction of molecular hydrogen increases as a function of $N(H_2)$.

Welty & Hobbs (2001) find nearly quadratic relationships between the column densities of K I and Na I and the total hydrogen column density. A quadratic dependence of $N(\text{K I})$ and $N(\text{Na I})$ on $N(H_{\text{tot}})$ is expected if the ionization equilibrium is dominated by photoioniza-

tion and radiative recombination, if the electron fraction is roughly constant, and if the individual clouds have a roughly uniform thickness (Hobbs 1974; Welty & Hobbs 2001). In Figure 12, we plot the observed trend of $N(\text{Cl I})$ versus $N(H_{\text{tot}})$. Least-squares linear fits to the “STIS+FUSE” and “all Galactic” samples yield slopes in the range 2.5–2.9 (see Table 7), much steeper than the corresponding trends involving K I and Na I. The steeper relationship for Cl I is due to the conversion of Cl^+ to Cl^0 in molecule-rich sight lines, where Cl I becomes the dominant ion. Indeed, the fraction of chlorine in neutral form, $f(\text{Cl I}) = N(\text{Cl I})/N(\text{Cl}_{\text{tot}})$, increases steeply as a function of $N(H_{\text{tot}})$.

Two sight lines are identified in Figure 12 as having anomalously low Cl I column densities relative to the total amount of hydrogen along the lines of sight. The two sight lines, HD 147933 (ρ Oph A) and HD 147888 (ρ Oph D), are part of the same stellar system and probe the same complex of diffuse molecular clouds (e.g., Snow et al. 2008). Welty & Hobbs (2001) describe these sight lines, and several others in the Sco-Oph region, as being “discrepant” because they exhibit several anomalous column density ratios. For example, both ρ Oph A and ρ Oph D have anomalously low K I and Na I column densities relative to $N(H_{\text{tot}})$ (Welty & Hobbs 2001; Snow et al. 2008). Furthermore, while both sight lines exhibit severe depletions of many different elements from the gas-phase (e.g., Ritchey et al. 2023), the molecular hydrogen fractions are unusually low. An enhanced UV radiation field may be responsible for the anomalously low column densities of Cl I, K I, Na I, and H_2 in these directions. Indeed, from an analysis of carbon ionization balance, Jenkins & Tripp (2011) find that the UV radi-

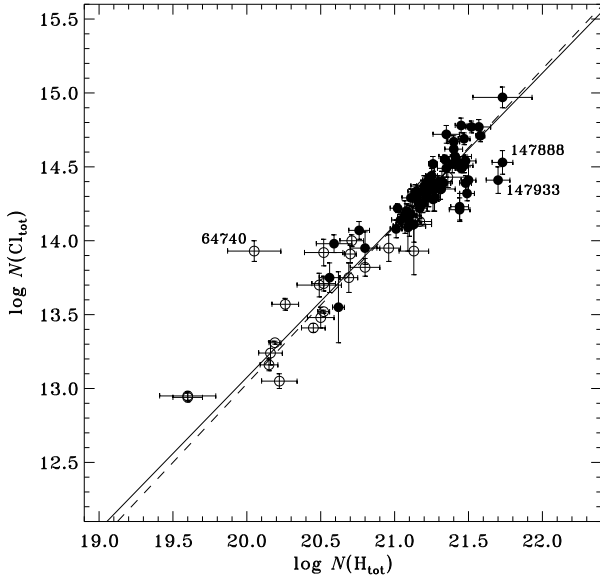


Figure 13. Correlation between $\log N(\text{Cl}_{\text{tot}})$ and $\log N(\text{H}_{\text{tot}})$. The plotting symbols have the same meaning as in Figure 11. Several outliers are indicated. (These sight lines were not excluded from the linear fits.)

ation field toward HD 147888 is enhanced by a factor of ~ 16 over the average interstellar field.

In Figure 13, we plot the observed relationship between $N(\text{Cl}_{\text{tot}})$ and $N(\text{H}_{\text{tot}})$. Least-squares linear fits to the “STIS+FUSE” and “all Galactic” samples yield slopes of ~ 1.0 – 1.1 and linear correlation coefficients of ~ 0.8 – 0.9 . The tight linear correlation between the total chlorine column density and the total hydrogen column density is an indication that the abundance and/or depletion of chlorine does not vary appreciably with $N(\text{H}_{\text{tot}})$. The weighted mean value of $\log[N(\text{Cl}_{\text{tot}})/N(\text{H}_{\text{tot}})]$ for the “all Galactic” sample is -6.893 ± 0.008 , which is consistent with (but somewhat higher than) the value of -6.99 ± 0.04 reported by Moomey et al. (2012). The sight lines to HD 147888 and HD 147933 do not appear to be significant outliers in Figure 13 like they are in Figure 12. Still, the total Cl column densities toward the ρ Oph stars are ~ 0.4 – 0.6 dex below that determined for the line of sight to HD 168076, which has a similar total hydrogen column density. The sight line to HD 64740 does appear to be an outlier in Figure 13, although the hydrogen column density is not very well determined in this direction (Bohlin et al. 1983; Jenkins 2009).

4.2. Phosphorus and Chlorine Depletion Parameters

The main objective of this investigation is the re-determination of depletion parameters for the elements phosphorus and chlorine. Previous studies of P abundances (e.g., Lebouteiller et al. 2005; Jenkins 2009) used

now outdated oscillator strengths for the important P II transitions, leading to an overestimation of P II column densities, and, consequently, an underestimation of the depletion of P onto interstellar grains. In his analysis of Cl depletion, Jenkins (2009) considered only Cl II column densities, neglecting any contribution from Cl I to the derived total Cl abundances. However, of the 68 sight lines in Table 5 with measurements (or upper limits) for both Cl I and Cl II, nearly half (32) have $N(\text{Cl I}) > N(\text{Cl II})$. Moreover, the neutral chlorine fraction, $f(\text{Cl I})$, increases systematically with $f(\text{H}_2)$ (see Section 4.3). The neglect of Cl I will therefore significantly impact the interpretation of any perceived trends involving the depletion of Cl onto interstellar grains.

As in Ritchey et al. (2018), we derive element depletion parameters following the methodology of Jenkins (2009). In this formalism, the logarithmic depletion of element X , defined as $[X/\text{H}] = \log(X/\text{H}) - \log(X/\text{H})_{\odot}$, depends on the sight-line depletion strength factor F_* according to:

$$[X/\text{H}] = B_X + A_X(F_* - z_X), \quad (1)$$

where the depletion parameters A_X , B_X , and z_X are unique to each element. The slope parameter A_X indicates how quickly a given element becomes depleted as the growth of dust grains progresses in interstellar clouds. The intercept parameter B_X indicates the expected depletion of element X at $F_* = z_X$, where z_X represents a weighted mean value of F_* for the particular set of sight lines with depletion measurements available for the element. Values of the coefficients A_X and B_X are obtained for each element through the evaluation of a least-squares linear fit, with $[X/\text{H}]$ as the dependent variable and F_* the independent variable. (The reason for the additional term involving z_X in Equation (1) is that for a particular choice of z_X there is a near zero covariance between the formal fitting errors for the solutions of A_X and B_X ; see Jenkins 2009).

Values of the depletion strength factor F_* for the sight lines in our combined P and Cl sample are obtained primarily from Jenkins (2019), although, in some cases, we use the F_* values provided by Jenkins (2009). The adopted values are listed in Table 6. The F_* values from Jenkins (2019) are preferred because they were derived solely from depletion measurements for Mg and Mn and thus are entirely independent from the elements considered in this investigation. Regardless of our preference, however, the two sets of F_* values are comparable. For the 70 sight lines in our sample that have depletion strength factors listed in both Jenkins (2019) and Jenkins (2009), the differences in the values are typically

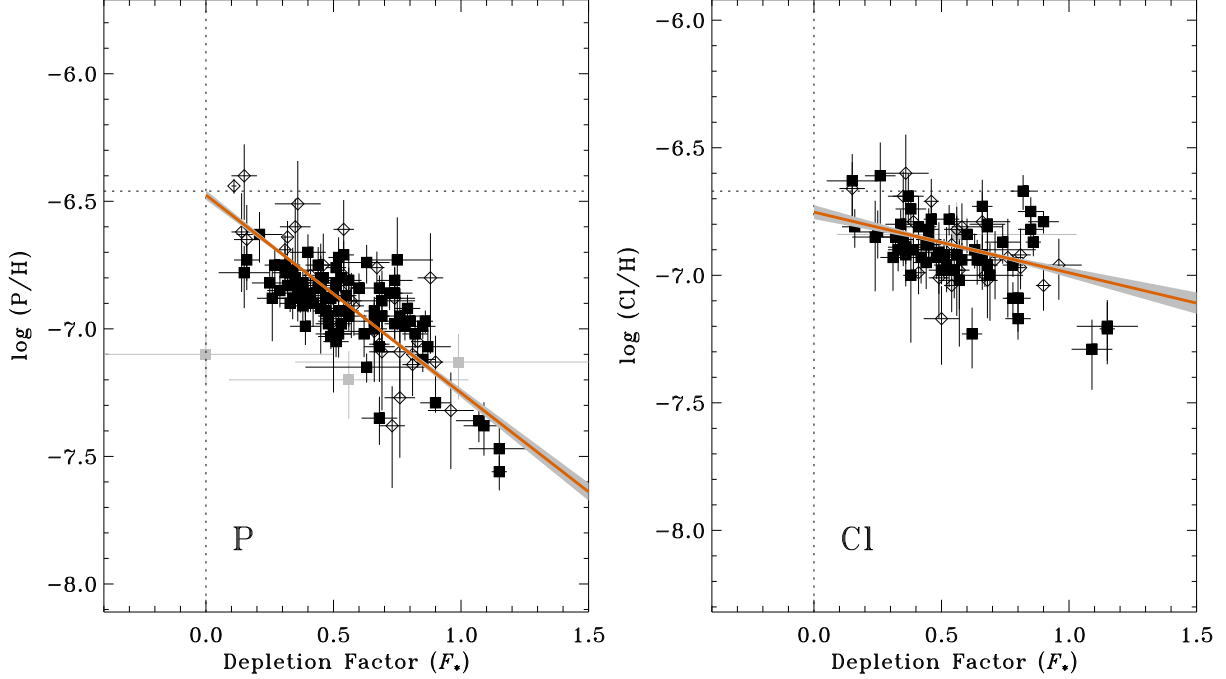


Figure 14. Gas-phase P and Cl abundances as a function of the sight line depletion factor (F_*). Solid squares represent abundances derived in this work from STIS and FUSE observations; open diamonds represent measurements obtained in previous studies from Copernicus and GHRS observations (Jenkins 2009; Mooney et al. 2012; Brown 2015). Grey symbols denote sight lines where $\sigma(F_*) \geq 0.30$. The solid orange lines represent linear fits to the data derived according to the methodology of Jenkins (2009). The shaded gray regions indicate the 1σ errors on the fit parameters. The horizontal dotted line in each panel gives the adopted solar system abundance from Lodders (2003).

at the 1σ or 2σ level. (The mean absolute difference is 1.1σ .)

In Figure 14, we plot the gas-phase P and Cl abundances⁶ as a function of F_* . Measurements obtained in this investigation (from the data presented in Tables 3, 5, and 6) are represented by solid squares, while measurements for additional sight lines examined in previous investigations are represented by open diamonds. In the case of phosphorus, we include the P II measurements tabulated by Jenkins (2009) for sight lines not included in our STIS sample. Most of these additional P II measurements were derived from Copernicus or Goddard High Resolution Spectrograph (GHRS) observations (see Jenkins 2009, and references therein). All of the P II column densities obtained from Jenkins (2009) were corrected so as to be consistent with the set of f -values adopted in this investigation (Table 2). However, many of these previously reported P abundances have large associated uncertainties. We therefore retained only those abundance measurements with logarithmic uncertainties less than or equal to 0.176 dex (corresponding to a relative uncertainty of 50% or bet-

ter). For our analysis of chlorine depletions, we include, in addition to our own measurements, the total Cl column densities reported by Mooney et al. (2012) and Brown (2015, see also Appendix A), which were based on Copernicus observations.

Depletion parameters for P and Cl were determined through least-squares linear fits to the trends of $[P/H]$ and $[Cl/H]$ versus F_* , adopting the functional form expressed in Equation (1). The resulting values of A_X , B_X , and z_X for the two elements are given in Table 8. The fits themselves are depicted by solid orange lines in Figure 14 with shaded gray regions indicating the 1σ errors on the fit parameters. The horizontal dashed lines in Figure 14 represent the adopted solar system abundances of P and Cl (Lodders 2003, see Table 8). Since the values obtained for the B_X parameters depend on the specific choice of reference abundances, the uncertainties in the solar system abundances were added in quadrature to the formal fitting errors for B_P and B_{Cl} to arrive at the uncertainties listed for these parameters in Table 8. (Note that the slope parameters A_X are entirely independent of the adopted solar reference abundances.)

The intercept parameters B_X are sensitive to the specific set of depletion measurements available for a given

⁶ Note that $\log(P/H) = \log N(P \text{ II}) - \log N(H_{\text{tot}})$, while $\log(Cl/H) = \log N(Cl_{\text{tot}}) - \log N(H_{\text{tot}})$.

Table 8. Element Depletion Parameters

Elem.	$\log (X/H)_{\odot}^a$	A_X	B_X	z_X	$[X/H]_0$	$[X/H]_1$	χ^2	ν
P	-6.46 ± 0.04	-0.776 ± 0.035	-0.418 ± 0.041	0.520	-0.015 ± 0.045	-0.791 ± 0.044	297.4	126
Cl	-6.67 ± 0.06	-0.238 ± 0.046	-0.223 ± 0.061	0.593	-0.082 ± 0.067	-0.320 ± 0.063	182.7	81

^aRecommended solar system abundance from [Lodders \(2003\)](#).

element (because they depend on z_X , which will vary from one element to the next). Thus, in order to facilitate a more straightforward comparison of the depletion results for different elements, it is important to evaluate two additional depletion parameters. The two parameters:

$$[X/H]_0 = B_X - A_X z_X \quad (2)$$

and

$$[X/H]_1 = B_X + A_X(1 - z_X), \quad (3)$$

indicate the expected depletions at $F_* = 0$ and $F_* = 1$, respectively. We interpret the $[X/H]_0$ values as representing the initial amounts of depletion present in the diffuse ISM before significant grain growth has occurred (or after the outer portions of the grains have been destroyed by the passage of an interstellar shock). The $[X/H]_1$ values represent the depletions associated with a prototypical diffuse molecular cloud. ([Jenkins \(2009\)](#) used the $v_{\odot} = -15 \text{ km s}^{-1}$ component toward $\zeta \text{ Oph}$ as the standard for a cloud with $F_* = 1$.) The values we obtain for $[P/H]_0$, $[P/H]_1$, $[Cl/H]_0$, and $[Cl/H]_1$ are provided in Table 8. (The errors in these quantities were determined according to the relations given in [Jenkins \(2009\)](#)).

The last two columns in Table 8 give the chi-squared value (χ^2) associated with each of the linear fits along with the number of degrees of freedom ν (i.e., the number of observations minus two). In each case, the reduced chi-squared value (χ^2/ν) is relatively high (i.e., 2.4 and 2.3 for the P and Cl fits, respectively). This could indicate that there is real intrinsic scatter in the gas-phase P and Cl abundances at a given value of F_* . Alternatively, the poor goodness-of-fit statistics could mean that the errors associated with the P and Cl abundances have been underestimated. The depletion trend for Cl, in particular, seems irregular. Some sight lines with moderate-to-large depletion strengths (such as HD 157857 and HD 206267) have relatively low gas-phase Cl abundances, while others with similar or even larger depletion strengths (such as X Per, HD 207308, and HD 207538) have much higher total Cl abundances.

The sight lines with the largest values of F_* (HD 37903, HD 147888, and HD 147933) all have Cl abundances that are lower than expected based on the linear trend shown in Figure 14.

An important fundamental result of our depletion analysis is that the “initial” depletions of P and Cl (i.e., the $[X/H]_0$ values) no longer indicate that the P and Cl abundances are “supersolar” at $F_* = 0$, in contrast to the results presented in [Jenkins \(2009\)](#). Both $[P/H]_0$ and $[Cl/H]_0$ are slightly less than zero (but consistent with zero at approximately the 1σ level), indicating very little (if any) P and Cl depletion in the low-density ISM. The depletion slope for P is relatively steep, however ($A_P \approx -0.8$), while the slope for Cl is rather shallow ($A_{Cl} \approx -0.2$). These results will be discussed further, and compared with the results for many other elements, in Section 5.1.

4.3. Additional Insights on Depletion

We can gain additional insight into the possible cause of the irregular depletion trend for Cl by examining separately the abundance trends for neutral and singly-ionized Cl. In Figure 15, we plot the abundances of Cl I and Cl II against the sight line depletion strength factors. In these plots, we have explicitly identified (with blue symbols) the discrepant Sco-Oph sight lines discussed in [Welty & Hobbs \(2001\)](#) (see also [Welty & Crowther 2010](#); [Welty et al. 2020](#)). These sight lines include: 1 Sco, π Sco, δ Sco, β^1 Sco, ω^1 Sco, ν Sco, σ Sco, ρ Oph A, and ρ Oph D. For most of the sight lines in our sample, we find a very steep increase in the Cl I abundance with increasing F_* (presumably due to the neutralization of Cl^+ in increasingly depleted H_2 -rich gas). However, the discrepant Sco-Oph sight lines (and several other sight lines, including κ Ori, HD 37903, HD 72754, HD 144965, HD 165246, HD 206267, HD 207198, and HD 210839) do not follow this trend, exhibiting Cl I abundances that are much lower than expected for sight lines having relatively large values of F_* .⁷

⁷ It should be noted that the sight-line depletion strength factor F_* increases systematically with increasing $f(H_2)$ for $\log f(H_2) >$

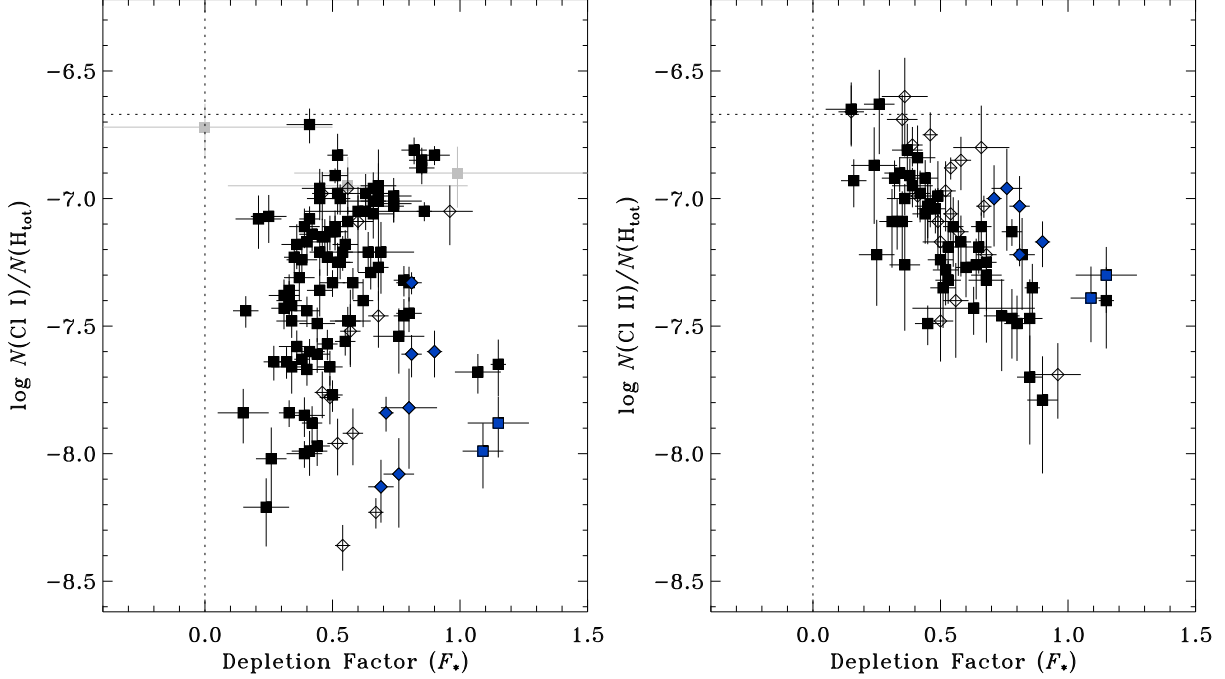


Figure 15. Abundances of Cl I (left panel) and Cl II (right panel) plotted as a function of the sight line depletion factor (F_*). Squares represent abundances derived in this work from STIS and FUSE observations; diamonds represent measurements obtained in previous studies from Copernicus and GHRS observations (Jenkins 2009; Mooney et al. 2012; Brown 2015). Grey symbols denote sight lines where $\sigma(F_*) \geq 0.30$. Blue symbols are used to identify the discrepant Sco-Oph sight lines (see Welty & Hobbs 2001; Welty & Crowther 2010). The horizontal dotted line in each panel gives the adopted solar system abundance from Lodders (2003).

As shown in the righthand panel of Figure 15, the Cl II abundance drops precipitously with increasing F_* (again, owing to the rapid neutralization of Cl^+ ions as the H_2 concentration increases). The discrepant Sco-Oph sight lines (plus several others, such as ψ Ori, κ Ori, HD 37903, and HD 165246) show enhanced Cl II abundances relative to other sight lines with similar values of F_* . The Sco-Oph sight lines, and the other discrepant sight lines, likely probe regions with enhanced UV radiation fields. This is certainly true of HD 37903, which probes the photodissociation region (PDR) associated with the reflection nebula NGC 2023. Likewise, HD 206267 is the exciting star of the H II region IC 1396 and HD 165246 probes gas in the outskirts of the Lagoon Nebula (M8). An enhanced UV radiation field would significantly reduce the neutral chlorine abundance (both through the photoionization of Cl^0 and the photodissociation of H_2), and would enhance the abundance of Cl^+ . These effects could then account for the anomalous Cl I and Cl II abundances seen along the discrepant sight lines noted above.

–1.0 if the discrepant Sco-Oph sight lines are excluded (see Welty et al. 2020).

If the Sco-Oph sight lines, and the other discrepant sight lines, are excluded from consideration, and the Cl depletion trend shown in Figure 14 is re-evaluated, the slope of the relation between the gas-phase Cl abundance and the sight line depletion factor becomes completely flat (i.e., $A_{\text{Cl}} = +0.00 \pm 0.05$). Conversely, if only the discrepant sight lines are considered, the slope of the relation is relatively steep (i.e., $A_{\text{Cl}} = -0.59 \pm 0.18$). If the same discrepant sight lines are excluded from the depletion analysis for P, the slope of the relation between the gas-phase P abundance and F_* is relatively unchanged (i.e., $A_{\text{P}} = -0.74 \pm 0.04$). However, if only the discrepant sight lines are included, the depletion slope for P becomes significantly steeper (i.e., $A_{\text{P}} = -1.49 \pm 0.18$). For both P and Cl, the gas-phase abundances are much better correlated with F_* when only the discrepant sight lines are considered. (For these fits, the χ^2/ν values are 0.7 for P and 1.1 for Cl.)

The implication is that the depletion rates are enhanced in regions with enhanced ionization. This would then point to the importance of ion-grain reactions in driving the depletion of elements from the gas phase. The accretion of atoms onto grain surfaces may be enhanced by the presence of very small negatively-charged dust grains (Weingartner & Draine 1999). Larger grains tend to be positively charged, yet most of the abun-

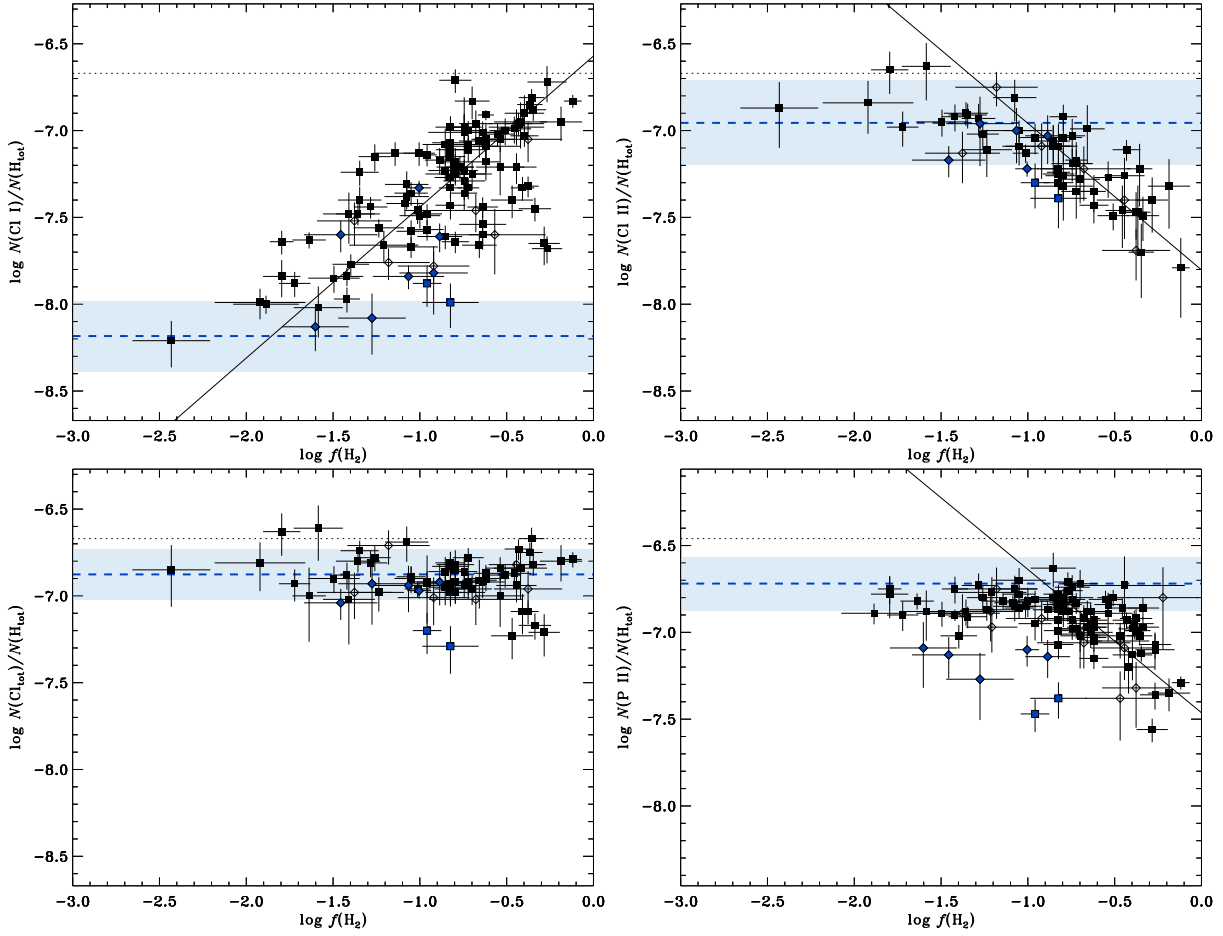


Figure 16. Gas-phase abundances of Cl I (upper left), Cl II (upper right), total Cl (lower left), and P II (lower right) plotted as a function of the line-of-sight molecular hydrogen fraction. Squares represent abundances derived in this work from STIS and FUSE observations; diamonds represent measurements obtained in previous studies from Copernicus and GHRS observations (Jenkins 2009; Mooney et al. 2012; Brown 2015). Blue symbols are used to identify the discrepant Sco-Oph sight lines (see Welty & Hobbs 2001; Welty & Crowther 2010). The black dotted line in each panel indicates the adopted solar system abundance from Lodders (2003). The blue dashed line and light blue shaded region represent the mean and standard deviation of the abundances for sight lines with $\log f(\text{H}_2) < -3.0$. Solid lines indicate linear fits with approximate slopes of $+0.9$ for Cl I (for sight lines with $\log f(\text{H}_2) > -3.0$) and -0.8 for Cl II and P II (for sight lines with $\log f(\text{H}_2) > -1.0$).

dant refractory elements in the ISM are singly ionized. The cross sections for collisions between ions and small grains are therefore enhanced, while those for larger grains are diminished (see Weingartner & Draine 1999). Our results indicate that there is no enhanced depletion of Cl in relatively dense (heavily depleted) regions where Cl is predominantly neutral (e.g., toward X Per, HD 207308, and HD 207538). However, there is enhanced Cl depletion in heavily depleted regions where Cl is mostly ionized (e.g., toward HD 37903, HD 147888, and HD 147933).

We can also examine the relationships that exist between the gas-phase P and Cl abundances and the (line-of-sight) molecular hydrogen fractions. In Figure 16, we plot the gas-phase abundances of Cl I, Cl II, total

Cl, and P II as a function of $f(\text{H}_2)$.⁸ As expected, the neutral chlorine abundance (upper left panel) increases systematically with the molecular hydrogen fraction. A linear fit indicates a slope of ~ 0.9 , similar to results for other trace neutral species, such as Na I and C I (e.g., Welty et al. 2020). There is considerable scatter in this relation, however, presumably because the total hydrogen column densities include varying amounts of atomic

⁸ Note that in all four panels of Figure 16, there are sight lines that are not shown because they have $\log f(\text{H}_2) < -3.0$. The gas-phase abundances in these directions are generally consistent with a single value for a given species such that the abundances exhibit a “plateau” at low molecular fraction. The blue dashed line and light blue shaded region in each panel represent the mean and standard deviation of the abundances for sight lines that are not shown in the figure.

hydrogen not associated with the molecular portions of the interstellar clouds (see Section 4.4). Conversely, the abundance of singly-ionized chlorine (upper right panel of Figure 16) shows a steady decrease with increasing $f(\text{H}_2)$, especially for sight lines with $\log f(\text{H}_2) \gtrsim -1.0$. The observed trends of Cl I and Cl II (relative to total H) versus $f(\text{H}_2)$ are a direct consequence of the rapid conversion of Cl^+ to Cl^0 in molecule-rich gas (Jura 1974; Neufeld & Wolfire 2009).

While the Cl I abundance increases with increasing $f(\text{H}_2)$, and the Cl II abundance decreases, the total Cl abundance (lower left panel of Figure 16) shows virtually no dependence on the line-of-sight molecular fraction. As already mentioned, there are some sight lines with unusually low total Cl abundances (such as HD 37903, HD 147888, HD 147933, HD 157857, and HD 206267), but the overall trend is exceptionally flat. In contrast, the gas-phase P abundances (lower right panel) show a relatively constant value for $\log f(\text{H}_2) \lesssim -1.0$ (with the exception of the Sco-Oph sight lines) and a sharp decline for $\log f(\text{H}_2) \gtrsim -1.0$. This behavior is typical of elements that exhibit moderate-to-strong depletions in cold interstellar clouds. For example, similar trends versus $f(\text{H}_2)$ are seen for the elements B (Ritchey et al. 2011), Mg (Cartledge et al. 2006; Jensen & Snow 2007b; Welty et al. 2020), Ti (Welty & Crowther 2010; Welty et al. 2020), and Fe (Jensen & Snow 2007a; Welty et al. 2020). Such trends are clear indications of the increase in gas-phase element depletions in increasingly dense, molecule-rich gas.

The discrepant Sco-Oph sight lines are prominent outliers in the plot showing P/H versus $f(\text{H}_2)$ (lower right panel of Figure 16). These sight lines are known to exhibit strong depletions of (for example) Mg, P, Ti, and Fe (e.g., Welty & Crowther 2010; Welty et al. 2020, this work), yet contain relatively little H_2 . An enhanced UV radiation field may be the source of these discrepancies. An enhanced flux of UV radiation (for example, if the absorbing gas is situated in close proximity to the background star) would contribute to H_2 photodissociation and would raise the ionization level of atomic species. An increase in the concentration of ionized species in the denser parts of the clouds could then lead to enhanced depletion through ion-grain reactions (e.g., Weingartner & Draine 1999). These results tend to corroborate our findings on Cl depletion, which indicate that enhanced depletion of Cl generally only occurs along sight lines with elevated levels of Cl ionization.

4.4. Neutral Chlorine Fractions

Because the first ionization potential of chlorine is less than that of hydrogen, chlorine is predominantly ionized

in low-density, diffuse atomic gas. However, in molecular gas (i.e., in regions where the H_2 molecules are optically thick), Cl^+ reacts rapidly with H_2 , yielding HCl^+ and H. The molecular ion HCl^+ then undergoes dissociative recombination or reacts further with H_2 , yielding H_2Cl^+ and H. Finally, the H_2Cl^+ is destroyed through dissociative recombination, producing HCl, Cl, and H (see Jura 1974; Neufeld & Wolfire 2009). Since the rate coefficient for the initial reaction ($k = 1.0 \times 10^{-9} \text{ cm}^3 \text{ s}^{-1}$), when combined with a typical density for neutral diffuse gas ($n_{\text{H}} \gtrsim 10 \text{ cm}^{-3}$), is considerably larger than the Cl photoionization rate for the average interstellar radiation field ($\Gamma \lesssim 4.8 \times 10^{-11} \text{ s}^{-1}$), chlorine will be predominantly neutral wherever H_2 is abundant.

With these considerations, Jura & York (1978) proposed a simple model to account for observations of Cl I and Cl II in the ISM. Their model consists of two zones: (1) a region where the H_2 molecules are optically thick, chlorine is entirely neutral, and there is some associated atomic hydrogen, and (2) a region where the H_2 molecules are optically thin, chlorine is ionized, and the hydrogen is predominantly (neutral) atomic. Following Sonnentrucker et al. (2002), Equation (A7) in Jura & York (1978) may be written

$$N_1(\text{H I}) = N(\text{H}_{\text{tot}})[f(\text{Cl I}) - f(\text{H}_2)], \quad (4)$$

where $N_1(\text{H I})$ is the column density of H I that is associated with the optically-thick H_2 region, $N(\text{H}_{\text{tot}})$ is the total column density of hydrogen along the line of sight, $f(\text{Cl I})$ is the neutral chlorine fraction for the line of sight, and $f(\text{H}_2)$ is the line-of-sight molecular hydrogen fraction. With this simple model, it is possible to use integrated line-of-sight column densities of Cl I, Cl II, H I, and H_2 to derive estimates for the total hydrogen column density and molecular hydrogen fraction associated with just the optically-thick H_2 region.

We apply Equation (4) to all of the sight lines in our chlorine sample with measurements of both Cl I and Cl II (Table 5), using values of $N(\text{H}_{\text{tot}})$ and $f(\text{H}_2)$ from Table 6. The results are presented in Table 9. Note, in particular, the last two columns of Table 9, which give $N_1(\text{H}_{\text{tot}}) = N_1(\text{H I}) + 2N(\text{H}_2)$ and $f_1(\text{H}_2) = 2N(\text{H}_2)/N_1(\text{H}_{\text{tot}})$, the total hydrogen column density and molecular hydrogen fraction, respectively, in the optically-thick H_2 region. We also include in Table 9 those sight lines with Cl I and Cl II measurements from Copernicus observations, provided that they also have measured values of $N(\text{H I})$ and $N(\text{H}_2)$ (Mooney et al. 2012; Brown 2015, Appendix A).

Table 9. Neutral Chlorine Fractions and Derived Parameters

Star	$\log N(\text{H}_{\text{tot}})$	$\log f(\text{Cl I})$	$\log f(\text{H}_2)$	$\log N_1(\text{H I})^{\text{a}}$	$\log N(\text{H}_2)$	$\log N_1(\text{H}_{\text{tot}})^{\text{b}}$	$\log f_1(\text{H}_2)^{\text{c}}$
HD 108	$21.47^{+0.04}_{-0.05}$	-0.22 ± 0.05	-0.72 ± 0.09	21.09 ± 0.09	20.45 ± 0.08	21.26 ± 0.07	-0.50 ± 0.10
HD 3827	$20.56^{+0.07}_{-0.08}$	-1.17 ± 0.11	-1.90 ± 0.25	19.29 ± 0.15	18.35 ± 0.25	19.38 ± 0.14	-0.73 ± 0.27
HD 12323	$21.28^{+0.04}_{-0.04}$	-0.20 ± 0.07	-0.72 ± 0.09	20.93 ± 0.11	20.26 ± 0.08	21.08 ± 0.09	-0.52 ± 0.11
HD 15137	$21.32^{+0.07}_{-0.08}$	-0.26 ± 0.08	-0.79 ± 0.10	20.90 ± 0.13	20.23 ± 0.08	21.06 ± 0.10	-0.53 ± 0.12
HD 24190	$21.30^{+0.05}_{-0.06}$	-0.15 ± 0.05	-0.62 ± 0.08	20.96 ± 0.10	20.38 ± 0.07	21.15 ± 0.07	-0.46 ± 0.10
HD 24534	$21.34^{+0.03}_{-0.04}$	-0.05 ± 0.03	-0.12 ± 0.05	20.51 ± 0.26	20.92 ± 0.04	21.30 ± 0.06	-0.08 ± 0.07
HD 37903	$21.44^{+0.06}_{-0.07}$	-0.45 ± 0.11	-0.29 ± 0.09	\dots^{d}	20.85 ± 0.07	20.99 ± 0.18	$+0.16 \pm 0.19$
HD 41161	$21.15^{+0.05}_{-0.05}$	-0.38 ± 0.07	-0.86 ± 0.10	20.60 ± 0.12	19.99 ± 0.09	20.78 ± 0.09	-0.49 ± 0.12
HD 46223	$21.58^{+0.03}_{-0.04}$	-0.18 ± 0.04	-0.61 ± 0.07	21.21 ± 0.08	20.67 ± 0.06	21.41 ± 0.06	-0.43 ± 0.08
HD 52266	$21.27^{+0.04}_{-0.04}$	-0.55 ± 0.15	-0.97 ± 0.09	20.51 ± 0.23	20.00 ± 0.08	20.72 ± 0.16	-0.42 ± 0.17
HD 53975	$21.09^{+0.04}_{-0.04}$	-0.63 ± 0.16	-1.64 ± 0.10	20.41 ± 0.18	19.15 ± 0.09	20.46 ± 0.16	-1.01 ± 0.18
HD 63005	$21.31^{+0.03}_{-0.03}$	-0.31 ± 0.09	-0.84 ± 0.09	20.84 ± 0.13	20.17 ± 0.09	21.00 ± 0.10	-0.52 ± 0.13
HD 66788	$21.26^{+0.04}_{-0.04}$	-0.58 ± 0.09	-1.24 ± 0.14	20.56 ± 0.12	19.72 ± 0.14	20.67 ± 0.10	-0.65 ± 0.17
HD 73882	$21.57^{+0.08}_{-0.09}$	-0.15 ± 0.07	-0.19 ± 0.12	20.28 ± 0.76	21.08 ± 0.10	21.41 ± 0.15	-0.03 ± 0.17
HD 75309	$21.19^{+0.03}_{-0.03}$	-0.39 ± 0.07	-0.73 ± 0.07	20.53 ± 0.14	20.16 ± 0.06	20.80 ± 0.09	-0.34 ± 0.10
HD 88115	$21.04^{+0.06}_{-0.07}$	-0.96 ± 0.05	-1.49 ± 0.15	19.94 ± 0.11	19.25 ± 0.14	20.09 ± 0.09	-0.54 ± 0.16
HD 89137	$21.11^{+0.06}_{-0.07}$	-0.39 ± 0.08	-0.79 ± 0.11	20.49 ± 0.15	20.02 ± 0.09	20.72 ± 0.10	-0.40 ± 0.13
HD 90087	$21.23^{+0.05}_{-0.05}$	-0.68 ± 0.05	-1.05 ± 0.08	20.31 ± 0.10	19.88 ± 0.07	20.55 ± 0.07	-0.37 ± 0.10
HD 91597	$21.42^{+0.06}_{-0.07}$	-1.09 ± 0.05	-1.42 ± 0.07	20.05 ± 0.12	19.70 ± 0.05	20.33 ± 0.07	-0.33 ± 0.09
HD 91824	$21.16^{+0.04}_{-0.04}$	-0.46 ± 0.07	-1.05 ± 0.10	20.57 ± 0.10	19.81 ± 0.09	20.70 ± 0.08	-0.59 ± 0.12
HD 91983	$21.22^{+0.05}_{-0.06}$	-0.50 ± 0.10	-0.82 ± 0.09	20.44 ± 0.19	20.10 ± 0.07	20.72 ± 0.12	-0.32 ± 0.13
HD 92554	$21.35^{+0.09}_{-0.11}$	-1.21 ± 0.07	-1.81 ± 0.11	20.01 ± 0.12	19.24 ± 0.07	20.14 ± 0.10	-0.59 ± 0.12
HD 94493	$21.18^{+0.05}_{-0.06}$	-0.79 ± 0.05	-0.79 ± 0.08	\dots^{d}	20.09 ± 0.06	20.38 ± 0.11	$+0.01 \pm 0.12$
HD 97175	$21.07^{+0.05}_{-0.06}$	-0.75 ± 0.12	-0.66 ± 0.10	\dots^{d}	20.10 ± 0.09	20.31 ± 0.18	$+0.09 \pm 0.20$
HD 99857	$21.35^{+0.06}_{-0.07}$	-0.50 ± 0.08	-0.75 ± 0.08	20.51 ± 0.19	20.30 ± 0.05	20.86 ± 0.10	-0.26 ± 0.11
HD 99890	$21.14^{+0.05}_{-0.05}$	-0.63 ± 0.06	-1.28 ± 0.10	20.41 ± 0.09	19.56 ± 0.09	20.52 ± 0.07	-0.66 ± 0.11
HD 109399	$21.17^{+0.05}_{-0.05}$	-0.66 ± 0.07	-0.86 ± 0.10	20.09 ± 0.22	20.01 ± 0.09	20.52 ± 0.11	-0.21 ± 0.14
HD 116852	$21.01^{+0.04}_{-0.04}$	-0.64 ± 0.07	-0.96 ± 0.10	20.09 ± 0.15	19.75 ± 0.09	20.37 ± 0.09	-0.32 ± 0.12
HD 121968	$20.59^{+0.12}_{-0.16}$	-1.41 ± 0.07	-1.59 ± 0.15	18.72 ± 0.29	18.70 ± 0.10	19.19 ± 0.14	-0.18 ± 0.16
HD 137595	$21.23^{+0.04}_{-0.05}$	-0.06 ± 0.06	-0.34 ± 0.07	20.85 ± 0.14	20.59 ± 0.06	21.17 ± 0.08	-0.28 ± 0.10
HD 147683	$21.41^{+0.11}_{-0.14}$	-0.11 ± 0.08	-0.42 ± 0.15	21.00 ± 0.21	20.68 ± 0.12	21.29 ± 0.13	-0.31 ± 0.17
HD 147888	$21.73^{+0.07}_{-0.09}$	-0.68 ± 0.11	-0.98 ± 0.09	20.74 ± 0.21	20.45 ± 0.05	21.05 ± 0.12	-0.30 ± 0.13
HD 147933	$21.70^{+0.08}_{-0.10}$	-0.70 ± 0.11	-0.83 ± 0.16	20.42 ± 0.44	20.57 ± 0.15	21.00 ± 0.19	-0.13 ± 0.23
HD 152590	$21.47^{+0.06}_{-0.07}$	-0.29 ± 0.08	-0.70 ± 0.11	20.96 ± 0.14	20.47 ± 0.10	21.18 ± 0.10	-0.41 ± 0.14
HD 156359	$20.80^{+0.10}_{-0.13}$	-1.36 ± 0.13	-2.43 ± 0.22	19.40 ± 0.16	18.07 ± 0.21	19.44 ± 0.15	-1.07 ± 0.24
HD 157857	$21.44^{+0.07}_{-0.08}$	-0.17 ± 0.09	-0.46 ± 0.12	20.96 ± 0.20	20.68 ± 0.10	21.27 ± 0.12	-0.29 ± 0.15
HD 165246	$21.45^{+0.03}_{-0.03}$	-0.49 ± 0.07	-1.01 ± 0.07	20.80 ± 0.10	20.14 ± 0.07	20.96 ± 0.08	-0.52 ± 0.10
HD 165955	$21.11^{+0.06}_{-0.07}$	-0.95 ± 0.07	-1.72 ± 0.09	20.08 ± 0.10	19.09 ± 0.07	20.16 ± 0.09	-0.77 ± 0.11
HD 167402	$21.20^{+0.05}_{-0.05}$	-0.23 ± 0.10	-0.84 ± 0.11	20.84 ± 0.13	20.06 ± 0.10	20.97 ± 0.11	-0.60 ± 0.14

Table 9 continued

Table 9 (continued)

Star	$\log N(\text{H}_{\text{tot}})$	$\log f(\text{Cl I})$	$\log f(\text{H}_2)$	$\log N_1(\text{H I})^{\text{a}}$	$\log N(\text{H}_2)$	$\log N_1(\text{H}_{\text{tot}})^{\text{b}}$	$\log f_1(\text{H}_2)^{\text{c}}$
HD 168076	$21.73^{+0.20}_{-0.37}$	-0.24 ± 0.08	-0.75 ± 0.21	21.33 ± 0.23	20.68 ± 0.08	21.49 ± 0.17	-0.51 ± 0.19
HD 168941	$21.25^{+0.04}_{-0.05}$	-0.17 ± 0.07	-0.84 ± 0.09	20.97 ± 0.10	20.11 ± 0.08	21.08 ± 0.08	-0.66 ± 0.11
HD 177989	$21.10^{+0.05}_{-0.05}$	-0.08 ± 0.07	-0.64 ± 0.13	20.88 ± 0.11	20.16 ± 0.12	21.02 ± 0.09	-0.56 ± 0.14
HD 190918	$21.40^{+0.06}_{-0.07}$	-0.37 ± 0.05	-1.26 ± 0.10	20.97 ± 0.08	19.84 ± 0.08	21.03 ± 0.07	-0.89 ± 0.10
HD 191877	$21.10^{+0.05}_{-0.06}$	-0.27 ± 0.05	-0.80 ± 0.17	20.69 ± 0.11	20.00 ± 0.17	20.84 ± 0.10	-0.54 ± 0.19
HD 192035	$21.39^{+0.04}_{-0.05}$	-0.13 ± 0.08	-0.46 ± 0.10	20.98 ± 0.16	20.63 ± 0.09	21.26 ± 0.10	-0.33 ± 0.13
HD 192639	$21.48^{+0.07}_{-0.08}$	-0.28 ± 0.06	-0.45 ± 0.12	20.72 ± 0.25	20.73 ± 0.10	21.20 ± 0.12	-0.17 ± 0.15
HD 195455	$20.62^{+0.04}_{-0.04}$	-0.92 ± 0.24	-1.89 ± 0.19	19.64 ± 0.27	18.42 ± 0.19	19.69 ± 0.25	-0.97 ± 0.29
HD 195965	$21.08^{+0.04}_{-0.05}$	-0.12 ± 0.07	-0.50 ± 0.09	20.73 ± 0.14	20.28 ± 0.08	20.96 ± 0.09	-0.38 ± 0.12
HD 201345	$21.02^{+0.05}_{-0.05}$	-0.69 ± 0.04	-1.36 ± 0.13	20.23 ± 0.08	19.36 ± 0.12	20.33 ± 0.07	-0.67 ± 0.13
HD 203374	$21.40^{+0.04}_{-0.05}$	-0.23 ± 0.06	-0.43 ± 0.08	20.73 ± 0.20	20.67 ± 0.07	21.17 ± 0.09	-0.20 ± 0.11
HD 206267	$21.49^{+0.05}_{-0.06}$	-0.28 ± 0.06	-0.34 ± 0.09	20.31 ± 0.49	20.85 ± 0.08	21.21 ± 0.12	-0.06 ± 0.14
HD 206773	$21.24^{+0.05}_{-0.06}$	-0.21 ± 0.05	-0.53 ± 0.08	20.76 ± 0.12	20.41 ± 0.06	21.04 ± 0.07	-0.32 ± 0.09
HD 207198	$21.50^{+0.05}_{-0.05}$	-0.24 ± 0.10	-0.41 ± 0.07	20.75 ± 0.28	20.79 ± 0.05	21.26 ± 0.11	-0.16 ± 0.12
HD 207308	$21.45^{+0.04}_{-0.05}$	-0.14 ± 0.06	-0.35 ± 0.07	20.90 ± 0.17	20.80 ± 0.06	21.31 ± 0.08	-0.21 ± 0.10
HD 207538	$21.52^{+0.04}_{-0.05}$	-0.09 ± 0.05	-0.36 ± 0.07	21.09 ± 0.14	20.85 ± 0.06	21.42 ± 0.07	-0.27 ± 0.09
HD 208440	$21.33^{+0.05}_{-0.06}$	-0.35 ± 0.05	-0.75 ± 0.12	20.75 ± 0.12	20.28 ± 0.11	20.97 ± 0.09	-0.39 ± 0.14
HD 209339	$21.27^{+0.04}_{-0.04}$	-0.35 ± 0.04	-0.84 ± 0.07	20.75 ± 0.07	20.13 ± 0.06	20.92 ± 0.05	-0.49 ± 0.08
HD 210839	$21.48^{+0.04}_{-0.04}$	-0.23 ± 0.07	-0.38 ± 0.06	20.69 ± 0.23	20.80 ± 0.05	21.24 ± 0.08	-0.14 ± 0.10
HD 212791	$21.13^{+0.12}_{-0.16}$	-0.46 ± 0.12	-1.41 ± 0.15	20.62 ± 0.17	19.42 ± 0.11	20.67 ± 0.15	-0.95 ± 0.18
HD 219188	$20.76^{+0.07}_{-0.08}$	-0.62 ± 0.07	-1.08 ± 0.12	19.96 ± 0.13	19.38 ± 0.11	20.14 ± 0.10	-0.46 ± 0.14
HD 220057	$21.10^{+0.11}_{-0.14}$	-0.21 ± 0.09	-0.53 ± 0.13	20.61 ± 0.21	20.27 ± 0.09	20.89 ± 0.13	-0.32 ± 0.15
BD+35 4258	$21.26^{+0.03}_{-0.03}$	-0.50 ± 0.08	-1.35 ± 0.11	20.69 ± 0.09	19.61 ± 0.11	20.76 ± 0.08	-0.85 ± 0.13
γ Cas	$20.16^{+0.08}_{-0.10}$	-1.03 ± 0.10	-3.33 ± 0.09	19.13 ± 0.12	16.53 ± 0.05	19.13 ± 0.12	-2.30 ± 0.13
ϵ Per	$20.50^{+0.09}_{-0.12}$	-0.44 ± 0.08	-0.68 ± 0.27	19.70 ± 0.35	19.52 ± 0.26	20.07 ± 0.23	-0.24 ± 0.32
ψ Ori	$20.49^{+0.15}_{-0.23}$	-1.65 ± 0.14	-5.41 ± 0.20	18.84 ± 0.19	14.78 ± 0.15	18.84 ± 0.19	-3.76 ± 0.23
λ Ori	$20.80^{+0.10}_{-0.12}$	-0.54 ± 0.07	-1.38 ± 0.21	20.19 ± 0.13	19.12 ± 0.20	20.26 ± 0.12	-0.84 ± 0.22
ϵ Ori	$20.45^{+0.08}_{-0.10}$	-1.32 ± 0.03	-3.58 ± 0.21	19.12 ± 0.09	16.57 ± 0.20	19.13 ± 0.08	-2.26 ± 0.21
κ Ori	$20.52^{+0.04}_{-0.04}$	-1.23 ± 0.04	-4.54 ± 0.20	19.29 ± 0.06	15.68 ± 0.20	19.29 ± 0.06	-3.31 ± 0.20
139 Tau	$20.96^{+0.08}_{-0.09}$	-0.77 ± 0.10	-0.92 ± 0.21	19.65 ± 0.43	19.73 ± 0.20	20.18 ± 0.22	-0.15 ± 0.27
1 Sco	$21.13^{+0.10}_{-0.13}$	-0.93 ± 0.16	-1.60 ± 0.20	20.10 ± 0.22	19.23 ± 0.18	20.20 ± 0.18	-0.67 ± 0.24
π Sco	$20.69^{+0.06}_{-0.07}$	-0.90 ± 0.10	-1.07 ± 0.20	19.28 ± 0.41	19.32 ± 0.20	19.79 ± 0.21	-0.16 ± 0.27
δ Sco	$21.17^{+0.08}_{-0.09}$	-0.57 ± 0.02	-1.45 ± 0.21	20.54 ± 0.09	19.41 ± 0.20	20.60 ± 0.08	-0.89 ± 0.21
β^1 Sco	$21.14^{+0.04}_{-0.04}$	-0.36 ± 0.01	-1.00 ± 0.07	20.66 ± 0.04	19.83 ± 0.06	20.78 ± 0.04	-0.64 ± 0.07
ω^1 Sco	$21.23^{+0.07}_{-0.09}$	-0.68 ± 0.08	-0.88 ± 0.13	20.11 ± 0.27	20.05 ± 0.11	20.55 ± 0.13	-0.20 ± 0.16
σ Sco	$21.36^{+0.14}_{-0.22}$	-1.15 ± 0.08	-1.27 ± 0.20	19.60 ± 0.47	19.79 ± 0.15	20.21 ± 0.20	-0.12 ± 0.23
χ Oph	$21.31^{+0.10}_{-0.13}$	-0.09 ± 0.03	-0.38 ± 0.20	20.90 ± 0.23	20.63 ± 0.18	21.22 ± 0.15	-0.28 ± 0.22
μ Nor	$21.19^{+0.08}_{-0.10}$	-0.14 ± 0.05	-0.44 ± 0.16	20.77 ± 0.19	20.45 ± 0.15	21.06 ± 0.13	-0.31 ± 0.19
γ Ara	$20.71^{+0.08}_{-0.09}$	-1.05 ± 0.04	-1.18 ± 0.24	19.07 ± 0.50	19.23 ± 0.23	19.66 ± 0.24	-0.13 ± 0.31

Table 9 continued

Table 9 (continued)

Star	$\log N(\text{H}_{\text{tot}})$	$\log f(\text{Cl I})$	$\log f(\text{H}_2)$	$\log N_1(\text{H I})^a$	$\log N(\text{H}_2)$	$\log N_1(\text{H}_{\text{tot}})^b$	$\log f_1(\text{H}_2)^c$
------	---------------------------------	-----------------------	----------------------	--------------------------	----------------------	-------------------------------------	--------------------------

^aColumn density of atomic hydrogen associated with the optically-thick H_2 region.

^bTotal hydrogen column density associated with the optically-thick H_2 region.

^cFraction of hydrogen in molecular form in the optically-thick H_2 region.

^dThe derived value of $N_1(\text{H I})$ for this sight line is negative. However, the data are consistent with $f_1(\text{H}_2) = 1$.

From the results presented in Table 9, we find that, to varying degrees, the molecular hydrogen fraction in the optically-thick H_2 region is always larger than the line-of-sight integrated value. This is illustrated in Figure 17, where the derived values of $f_1(\text{H}_2)$ are plotted against the observed line-of-sight values $f(\text{H}_2)$. All of the data points lie above the line of equality represented by the diagonal dashed line in the figure. For the median sight line in our sample, the molecular fraction in the optically-thick H_2 region is a factor of 2.8 larger than the line-of-sight value. Note that, according to Equation (4), the ratio $f_1(\text{H}_2)/f(\text{H}_2) = 1/f(\text{Cl I})$. Thus, the larger the neutral chlorine fraction, the smaller the contrast between $f_1(\text{H}_2)$ and $f(\text{H}_2)$. Another way to state this is that the neutral chlorine fraction is equivalent to the fraction of total hydrogen associated with the optically-thick H_2 region: $f(\text{Cl I}) = N(\text{Cl I})/N(\text{Cl}_{\text{tot}}) = N_1(\text{H}_{\text{tot}})/N(\text{H}_{\text{tot}})$.

The largest neutral chlorine fractions (i.e., $f(\text{Cl I}) \gtrsim 0.8$) are seen toward HD 24534 (X Per), HD 137595, HD 177989, HD 207538, and χ Oph. For these sight lines, more than 80% of the interstellar material is associated with the H_2 -bearing gas. The smallest fractions ($f(\text{Cl I}) \lesssim 0.05$) are found toward HD 121968, HD 156359, ψ Ori, and ϵ Ori. The sight line to HD 121968 is interesting because, while the molecular material constitutes only $\sim 4\%$ of the total hydrogen column, the molecular fraction in that material is high (i.e., $f_1(\text{H}_2) \approx 0.65$). Similar results are found toward σ Sco and γ Ara, where $f(\text{Cl I}) \approx 0.07$ and 0.09 , respectively, but $f_1(\text{H}_2) \approx 0.76$ and 0.74 . (The uncertainties associated with these values are relatively large, however; see Table 9) For the median sight line in our sample, $\sim 36\%$ of the total hydrogen column is associated with the optically-thick H_2 region.

An interesting pattern emerges from the data plotted in Figure 17. For sight lines with $\log f(\text{H}_2) \gtrsim -0.85$, the $f_1(\text{H}_2)$ values adhere more closely to the line of equality (the diagonal dashed line in Figure 17). If a data point lies along this line of equality, then all of the hydrogen along the line of sight is associated with the H_2 -bearing gas. (Note this does not mean that all of the hydro-

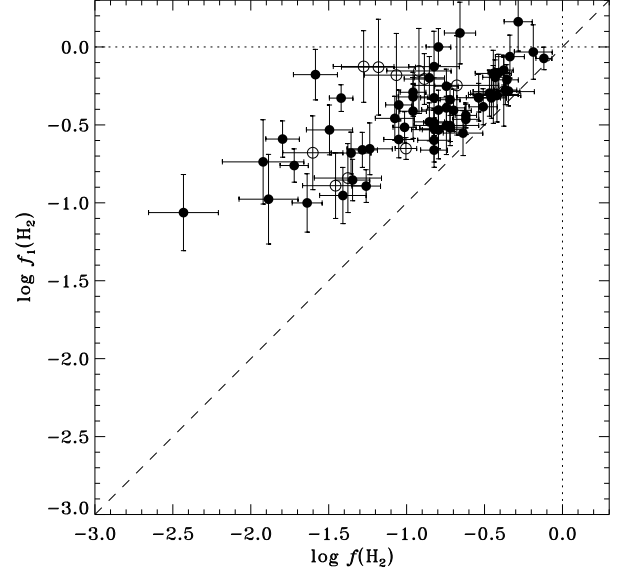


Figure 17. Molecular fraction associated with the optically-thick H_2 region, denoted $f_1(\text{H}_2)$, plotted against the line-of-sight molecular fraction, $f(\text{H}_2)$. The plotting symbols have the same meaning as in Figure 11. The diagonal dashed line indicates the line of equality between $f_1(\text{H}_2)$ and $f(\text{H}_2)$. Four sight lines with very low values of $f(\text{H}_2)$ (i.e., γ Cas, ψ Ori, ϵ Ori, and κ Ori) are not shown in this plot.

gen is in the form of H_2 .) Values of $\log f(\text{H}_2) \gtrsim -0.85$ roughly correspond to molecular hydrogen column densities of $\log N(\text{H}_2) \gtrsim 20.0$. This threshold value in $f(\text{H}_2)$ also approximately corresponds to the point at which the gas-phase abundances (of P and other depleted elements, such as Mg, Ti, and Fe) begin to fall sharply with increasing $f(\text{H}_2)$ (Figure 16; see also Figure 21 in Welty et al. 2020).

One of the motivations for the analysis of neutral chlorine fractions described here is to determine whether any of the sight lines in our sample contain “translucent” interstellar material. A translucent cloud is generally defined as having a total visual extinction $A_V \gtrsim 1$ mag, a molecular hydrogen fraction $f(\text{H}_2) \gtrsim 0.9$, and a kinetic temperature $T_k \lesssim 40$ K (van Dishoeck & Black 1988; Rachford et al. 2002). Previous H_2 surveys with FUSE (e.g., Rachford et al. 2002, 2009) have generally failed to detect true translucent clouds along any of the sight

lines surveyed. This failure may (at least partly) be due to the fact that the line-of-sight molecular fractions that are examined are lower limits to the true molecular fractions in the portions of the clouds where the H_2 molecules reside (Figure 17). Sonnentrucker et al. (2002) recognized that an analysis of neutral chlorine fractions could help to identify any translucent material along an otherwise complex line of sight.

There are several sight lines in Table 9 where the results for $f_1(\text{H}_2)$ indicate that the molecular fraction in the H_2 -bearing gas could be as high as ~ 1 . Two intriguing cases are presented by the sight lines to HD 94493 and HD 97175. In both cases, the outcome for $N_1(\text{H I})$ is negative because $f(\text{Cl I})$ is slightly smaller than $f(\text{H}_2)$. (This is an unphysical result, based on our simple model, because there cannot be more molecular hydrogen than total hydrogen in the H_2 -bearing gas.) Nevertheless, within the uncertainties, both sight lines could have a value of $f_1(\text{H}_2) \approx 1$. Neither of these sight lines would traditionally be characterized as a translucent sight line, however. The total visual extinction toward HD 94493 is $A_V = 0.82 \pm 0.18$ (Valencic et al. 2004). The extinction may be somewhat less toward HD 97175 based on a comparison of the $E(B-V)$ values (Table 1). The H_2 rotational temperatures in the two directions are $T_{01} = 79$ K and 74 K, respectively (Jenkins 2019), consistent with the average interstellar value of ~ 80 K.

The outcome for $N_1(\text{H I})$ toward HD 37903 is also negative. However, again, the result for $f_1(\text{H}_2)$ is consistent with 1 (within the uncertainties). This is an interesting sight line, which has been included in many previous surveys of “translucent clouds” (e.g., Cartledge et al. 2001; Rachford et al. 2009). The total visual extinction in this direction is $A_V = 1.28 \pm 0.15$ and the H_2 rotational temperature is $T_{01} = 68 \pm 7$ K (Rachford et al. 2009). However, this sight line shows enhanced depletion of Cl, which tends to complicate the analysis of the neutral chlorine fraction (see below). Nevertheless, the “true” molecular fraction seems to be quite high in this direction, despite the fact that only $\sim 36\%$ of the total H is associated with the H_2 -bearing gas.

Three other sight lines are worth mentioning in this context. The derived values of $f_1(\text{H}_2)$ toward HD 24534 (X Per), HD 73882, and HD 206267 are consistent (within the quoted 1σ uncertainties) with $f_1(\text{H}_2) \approx 1$. The values are $f_1(\text{H}_2) = 0.84 \pm 0.15$ toward X Per, 0.93 ± 0.46 toward HD 73882, and 0.88 ± 0.33 toward HD 206267. In all three cases, the $f_1(\text{H}_2)$ values are larger than the line-of-sight molecular fractions, which are $f(\text{H}_2) = 0.76 \pm 0.10$ toward X Per, 0.65 ± 0.21 toward HD 73882, and 0.46 ± 0.11 toward HD 206267. The values of total visual extinction are also fairly

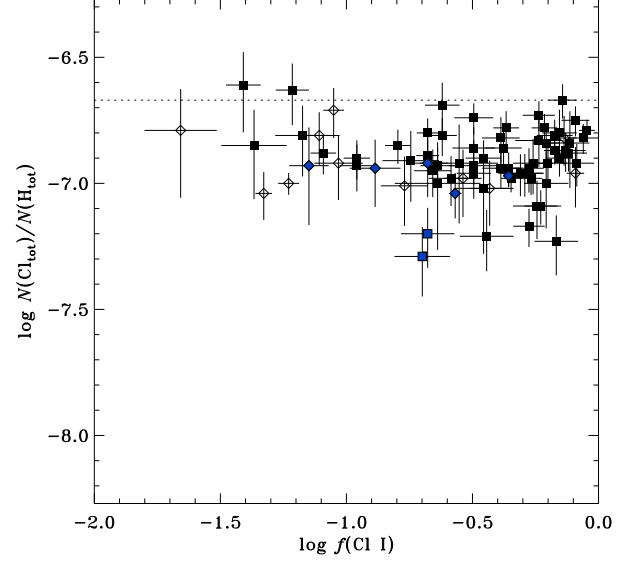


Figure 18. Total gas-phase Cl abundance plotted as a function of the fraction of neutral chlorine along the line of sight. Plotting symbols have the same meaning as in Figure 16. (Note the differences in the scales of the axes between this figure and Figure 16.)

high in these directions: $A_V = 2.05 \pm 0.18$ (X Per), 2.36 ± 0.23 (HD 73882), and 1.41 ± 0.18 (HD 206267) (Rachford et al. 2009). The H_2 rotational temperatures, however, are somewhat larger than the values expected for translucent clouds: $T_{01} = 57 \pm 4$ K (X Per), 51 ± 6 K (HD 73882), and 65 ± 5 K (HD 206267) (Rachford et al. 2002). There may be stratification in the molecular gas, however, since the kinetic temperatures derived from C_2 excitation are lower than the H_2 rotational temperatures: $T_k = 45 \pm 10$ K toward X Per, 20 ± 5 K toward HD 73882, and 35 ± 5 K toward HD 206267 (Sonnentrucker et al. 2007).

An explicit assumption in the derivation of Equation (4) is that the depletion of Cl does not vary between the zone where the H_2 is optically thick and the zone where the hydrogen is predominantly atomic (Jura & York 1978). Justification for this assumption is provided by Figure 16, where it is shown that the gas-phase Cl abundance does not vary significantly as a function of the line-of-sight molecular hydrogen fraction. As demonstrated in Figure 18, the gas-phase Cl abundance also does not vary as a function of the neutral chlorine fraction. (Recall that the neutral chlorine fraction is equivalent to the fraction of the total hydrogen column associated with the optically-thick H_2 region.) To illustrate this point, consider the line of sight toward X Per, where $\sim 90\%$ of the interstellar material is associated with the H_2 -bearing gas. This sight line has a total gas-phase Cl abundance of $\log(\text{Cl}/\text{H}) = -6.79^{+0.04}_{-0.05}$, in-

dicating a logarithmic depletion of $[\text{Cl}/\text{H}] = -0.12$. In contrast, $\sim 2\%$ of the interstellar material toward ψ Ori is associated with the H_2 component. However, the total gas-phase Cl abundance is identical to that toward X Per: $\log(\text{Cl}/\text{H}) = -6.79^{+0.16}_{-0.27}$.

If the depletion of Cl does vary between the two zones, then the analysis of the neutral chlorine fractions becomes more complicated. In general, if the depletion level is higher in the zone where Cl is predominantly neutral, then the derived values of $f_1(\text{H}_2)$ will be lower (see the discussion in [Sonnentrucker et al. 2002](#)). However, while there are a handful of sight lines that exhibit enhanced Cl depletion (see Section 4.3), these appear to be special cases. Depletion results for the vast majority of sight lines in our Cl sample indicate that Equation (4) should be generally valid.

5. DISCUSSION

5.1. Implications for Dust Formation and Evolution

The primary purpose of our reexamination of phosphorus and chlorine abundances in the diffuse ISM is to clarify the depletion behaviors of these elements. In his landmark study of gas-phase element depletions, [Jenkins \(2009\)](#) found that the depletion trends for P and Cl indicated that the abundances of these elements were supersolar at $F_* = 0$. With our new evaluation of the depletion properties of P and Cl (Figure 14 and Table 8), we have demonstrated that this is not the case. We find values of $[\text{P}/\text{H}]_0$ and $[\text{Cl}/\text{H}]_0$ that are slightly less than zero (but consistent with zero within the uncertainties), indicating very little (if any) depletion of P or Cl in the low-density diffuse ISM.

With our improved constraints on P and Cl depletions, it is worthwhile reexamining the depletion results for all of the elements that have been analyzed via the [Jenkins \(2009\)](#) formalism. In Figure 19, we plot the depletions at $F_* = 0$ and $F_* = 1$ for 24 different elements as a function of the 50% condensation temperatures (T_C) calculated by [Lodders \(2003\)](#). (This is an updated version of a similar figure presented in [Ritchey et al. \(2018\)](#). New results obtained in this investigation are indicated by orange symbols in Figure 19.) Note that, in addition to the new depletion parameters obtained for P and Cl, we also include in Figure 19 depletion results for the element F. These values are obtained from an analysis of F depletions reported in the literature ([Federman et al. 2005](#); [Snow et al. 2007](#), see Appendix B).

Our new results on P, Cl, and F depletions help to clarify the situation regarding gas-phase element depletions at $F_* = 0$. A fairly coherent trend now emerges, where the depletions at $F_* = 0$ are consistent with zero for elements with $T_C \lesssim 800$ K. For $T_C \gtrsim 800$ K, the

elements Ge, Ga, Cu, Mn, Cr, Fe, Ni, and Ti exhibit a clear trend of increasing depletion with increasing T_C , although the trend appears to flatten for $T_C \gtrsim 1200$ K. The elements P, Si, and Mg do not participate in this trend, however, as they exhibit very little depletion at $F_* = 0$ despite having large condensation temperatures. (Note that the initial depletions for the elements As and Pb are highly uncertain because these elements are detected only along sight lines with relatively high values of F_* ; see [Ritchey et al. 2018](#)).

At $F_* = 1$, another fairly regular pattern emerges. The volatile elements (i.e., C, N, O, and Kr) exhibit somewhat more depletion at $F_* = 1$ than at $F_* = 0$ (except for N, which has a depletion slope of $A_N = 0$). Meanwhile, a nearly linear trend of increasing depletion with increasing T_C is seen for most of the more refractory elements from Cd at $T_C = 650$ K to Ti at $T_C = 1580$ K. (Note that the depletion results for S are also uncertain; see [Jenkins 2009](#)). The elements Cl, As, P, Si, and Mg, however, do not follow this linear trend. These elements seem to form a second branch of the trend displaced toward higher gas-phase abundance.⁹

In the context of dust grain formation, the depletions at $F_* = 0$ are probably a good representation of the dust-phase abundances that pertain to the cores of the grains that emerge from stellar outflows and supernova ejecta. After being released into the ISM, the grains produced by stellar sources are subject to interstellar shocks, which may strip the outer portions of the grains leaving only the resilient cores. There are therefore two possibilities that might explain the elevated gas-phase abundances of P, Si, and Mg at $F_* = 0$. Either these elements are inhibited from condensing into the grains produced in some stellar sources, or these elements are primarily incorporated into grain mantles that are more easily disrupted or destroyed through sputtering in interstellar shocks.

Observations of dust shells around O-rich AGB stars (e.g., [Karovicova et al. 2013](#)) are consistent with two distinct populations of dust grains condensing at different distances from the stellar photosphere. Alumina grains (Al_2O_3) condense close to the stellar surface (at $\sim 2 R_*$), while silicate grains condense at larger distances ($\sim 4\text{--}5 R_*$) where the gas temperature is lower. [Karovicova et al. \(2013\)](#) find that some O-rich AGB stars have both an alumina shell and a silicate shell,

⁹ Recent work by [Lodders & Fegley \(2023\)](#) indicates that the 50% condensation temperature for Cl may be significantly lower than that adopted here. [Lodders & Fegley \(2023\)](#) find a value of $T_C = 427$ K for Cl, which would place it among the low-depletion elements with $T_C \lesssim 800$ K.

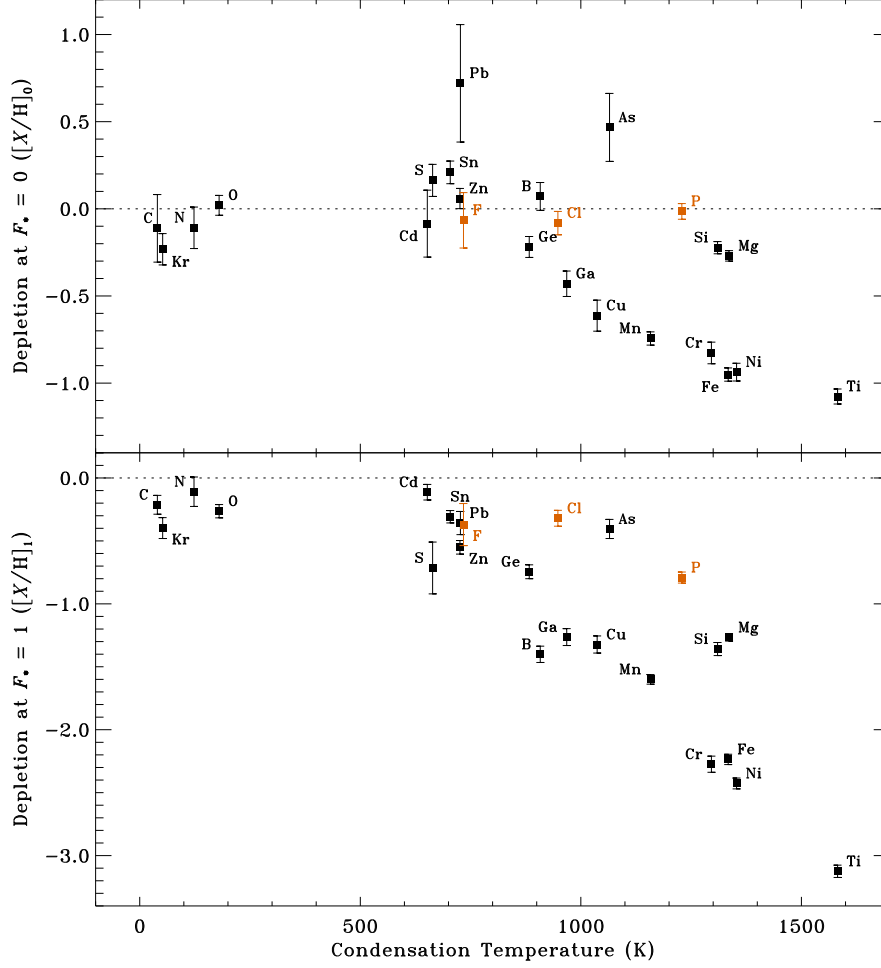


Figure 19. Element depletions (at $F_* = 0$ and $F_* = 1$) as a function of the condensation temperature (T_C) from Lodders (2003). Orange symbols are used for results obtained in this work; black symbols show results for additional elements examined in previous investigations (Jenkins 2009; Ritchey et al. 2018). Note the depletions for Mn and Cu (from Jenkins 2009) have been adjusted here by +0.165 dex and -0.016 dex, respectively, to account for updated f -values (Toner & Hibbert 2005; Brown et al. 2009).

while others have only an alumina dust shell. Furthermore, the stars with silicate shells tend to have much higher mass-loss rates. For the less-evolved stars with low mass-loss rates, the density in the cooler regions of the outflow (farther from the stellar surface) may be too low for significant SiO condensation. (SiO is thought to be the seed particle for silicate nucleation; e.g., Paquette et al. 2011; Gail et al. 2013). Since the condensation temperature for Al_2O_3 is significantly larger than that for SiO, alumina condensation takes place closer to the stellar photosphere where the gas density is higher.

The fact that some AGB stars do not form silicate dust shells may help to explain why the gas-phase abundances of Si and Mg are significantly larger than those of other refractory elements (e.g., Fe) at $F_* = 0$ (Figure 19). Karovicova et al. (2013) argue that, owing to the relatively low cosmic abundance of Al, alumina grains alone

cannot account for the observed dust-to-gas ratios in the outflows of AGB stars lacking silicate dust shells. The alumina grains that condense near the stellar surface may become seeds for further dust growth at larger radii and lower dust temperatures. Metallic Fe grains are good candidates for a dust growth species that would contribute mass but would not alter the spectral signature of Al_2O_3 . It is interesting to note that many of the elements that exhibit a clear dust condensation sequence at $F_* = 0$ (Ge, Ga, Cu, Cr, Fe, and Ni) condense into a host phase of Fe alloy (Lodders 2003).

Gobrecht et al. (2016) model dust and molecule formation in the inner wind of the O-rich AGB star IK Tau. These authors consider the effects of periodic shocks on the gas induced by stellar pulsation and follow the resulting non-equilibrium chemistry in the shocked gas layers. They find that some molecules (e.g., CO, PN, and HCl) form in the post-shock gas of the shocked

photosphere and maintain almost constant abundances in the inner wind. The near constant abundances indicate that these molecules do not participate in complex chemistries or in the formation of dust clusters in the post-shock gas. The modelled abundances of PN and HCl are comparable to (and even somewhat larger than) the cosmic abundances of P and Cl, indicating that all of the P and Cl atoms are locked up in these species. The predictions of the [Gobrecht et al. \(2016\)](#) model are in agreement with our interstellar measurements, which show that there is essentially no depletion of P and very little (if any) depletion of Cl at $F_* = 0$.

[Jones et al. \(2017\)](#) offer an alternative explanation for why the depletions of Si and Mg are different from those of the iron group elements. They postulate that the differences in depletion are a natural consequence of the composition and structure of interstellar silicate grains. In the [Jones et al. \(2017\)](#) model, the silicate group elements (O, Si, and Mg) form Mg-rich olivine and pyroxene-type amorphous silicate structures, while the iron group elements (Fe, Cr, Ni, Ti, and Mn) are present as Fe-rich nano-inclusions within the amorphous silicate matrix. [Jones et al. \(2017\)](#) argue that the iron group elements show less variation in depletion because, as nano-inclusions, they are better protected by the surrounding silicate matrix and thereby better able to withstand the effects of sputtering in interstellar shocks.

[Dwek \(2016\)](#) argues that most of the Fe missing from the gas phase in interstellar clouds must have precipitated from the ISM gas by a cold accretion onto pre-existing silicate or carbon grains. He bases this conclusion on the fact that most Fe is produced in Type Ia SNe yet observational evidence suggests that these objects do not produce significant quantities of dust (e.g., [Blair et al. 2007](#)). While some thermally-condensed Fe dust may be contributed by core-collapse SNe and AGB star winds, [Dwek \(2016\)](#) estimates that less than 35% of the Fe that is injected into the ISM is in solid form. The observed fraction of Fe in interstellar dust ranges from 89% at $F_* = 0$ to 99% at $F_* = 1$ ([Jenkins 2009](#)). Thus, if the argument advanced by [Dwek \(2016\)](#) is correct, there must be a very efficient cycling of material between the cold and warm phases of the diffuse ISM.

In a series of dust evolution models based on a hydrodynamic simulation of the ISM, [Zhukovska et al. \(2016, 2018\)](#) are able to reproduce the observed trends of increasing Si and Fe depletion with gas density by adopting a grain size distribution that includes a population of very small negatively-charged dust grains. Coulomb interactions between negatively-charged grains and ionized gas species enhance collision rates and lead to an increase in grain growth in the cold neutral medium

(CNM). The rates of dust growth in the ISM in the [Zhukovska et al. \(2016, 2018\)](#) models far exceed the rates of dust production by stellar sources.

[Priestley et al. \(2021\)](#), however, question the efficiency of grain growth in the diffuse ISM. They argue that if accretion were as efficient as in the [Zhukovska et al. \(2016, 2018\)](#) models, the small grains would grow to the point where they become positively charged, thereby halting any further accretion. [Priestley et al. \(2021\)](#) suggest that the strong depletions seen in the CNM (i.e., at $F_* = 1$) represent the dust-phase abundances of grains produced by evolved stars and supernovae. The variation in depletions (e.g., between $F_* = 1$ and $F_* = 0$) would then mostly be due to the destruction of dust grains in supernova shocks, although the dust destruction efficiency would need to be reduced.

Our results on interstellar P and Cl depletions provide evidence that grain growth in fact does occur in the diffuse ISM and that the depletion rates are enhanced by ion-grain reactions (Section 4.3). We find enhanced Cl depletions along sight lines with higher than expected levels of Cl ionization (e.g., along sight lines probing PDRs, such as HD 37903, HD 147933, and HD 147888). Moreover, if we examine the P and Cl depletion trends for just those sight lines exhibiting elevated levels of ionization, we find much steeper depletion slopes (i.e., rates of depletion) than for the general samples. Clearly, these increased depletion rates are related to the environmental conditions in the interstellar clouds and not to the injection of depleted gas from stellar sources. The elevated levels of ionization strongly suggest that efficient ion-grain reactions are the source of the enhanced depletions.

5.2. The Molecular Content of Diffuse Clouds

It is commonly assumed that the molecular hydrogen fraction in the H_2 -bearing portion of a diffuse cloud is larger than the value derived from the integrated column densities of H I and H_2 along a line of sight. However, it is not often possible to directly assess the true local value of the molecular hydrogen fraction. The analysis described in Section 4.4 involving neutral chlorine fractions allows us to obtain estimates for the molecular fractions in the H_2 -bearing gas, provided that our simple two-zone model for Cl chemistry is reasonably correct. We find that all sight lines with $\log N(\text{H}_2) \gtrsim 18$ have molecular fractions in the optically-thick H_2 region of $f_1(\text{H}_2) \gtrsim 0.1$ (Figure 20). The only sight lines with $f_1(\text{H}_2)$ values significantly less than 0.1 are those that probe molecular gas in the transition region where H_2 is not yet fully self-shielded (i.e., γ Cas, ψ Ori, ϵ Ori,

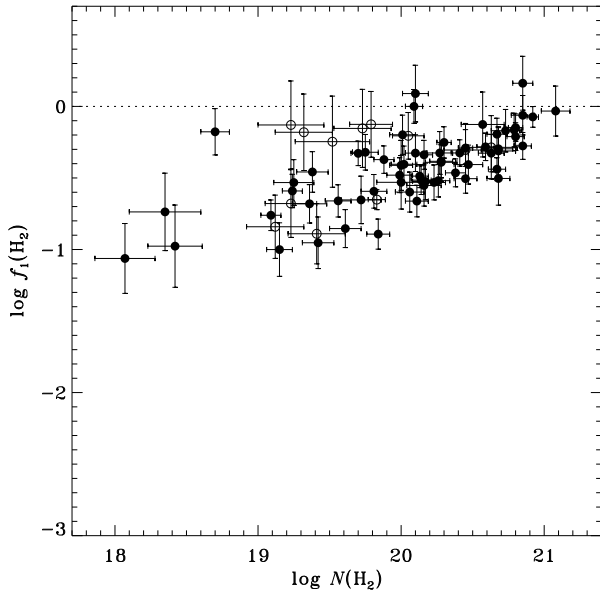


Figure 20. Molecular fraction associated with the optically-thick H_2 region, $f_1(\text{H}_2)$, plotted against the column density of molecular hydrogen, $N(\text{H}_2)$. The plotting symbols have the same meaning as in Figure 11. Four sight lines with very low values of $N(\text{H}_2)$ (i.e., γ Cas, ψ Ori, ϵ Ori, and κ Ori) are not shown in this plot.

and κ Ori). For $\log N(\text{H}_2) \gtrsim 18$, the $f_1(\text{H}_2)$ values increase only gradually until the molecular hydrogen column reaches a value of $\log N(\text{H}_2) \approx 20$, after which there is a much steeper rise. The H_2 -bearing gas is essentially fully molecular at $\log N(\text{H}_2) \approx 21$.

There are some exceptions to this general trend. For example, there is a group of sight lines (that includes HD 121968, γ Ara, π Sco, ϵ Per, 139 Tau, and σ Sco) with $\log N(\text{H}_2) \lesssim 20$ and $f_1(\text{H}_2) \gtrsim 0.5$. The most prominent outlier among these is HD 121968, which has $\log N(\text{H}_2) \approx 18.7$ and $f_1(\text{H}_2) \approx 0.65$. This sight line probes gas in the lower halo at a distance of ~ 3.3 kpc above the Galactic plane. While much of that pathlength is evidently filled with low-density neutral, atomic gas, the sight line also apparently crosses a small, moderately-dense diffuse molecular cloud. Kinematic evidence suggests that this small cloud is located close to the Galactic disk rather than near the position of the background star. The other outliers mentioned above (which are from the Copernicus sample; see Mooney et al. 2012, Appendix A) have rather large errors associated with their derived values of $f_1(\text{H}_2)$.

The median value of $f_1(\text{H}_2)$ for our sample of 78 sight lines with determinations of $f(\text{Cl I})$ is 0.40, which may be compared to the median value of $f(\text{H}_2)$ for the same sight lines, which is 0.15. A value of $f(\text{H}_2) \approx 0.4$ might then be adopted as a typical molecular hydrogen fraction for the H_2 -bearing portions of diffuse clouds.

This value is somewhat lower than the values that have been adopted in previous efforts to analyze the physical conditions in diffuse molecular gas. Jenkins & Tripp (2011), for example, adopt a value of $f(\text{H}_2) = 0.6$ for the CNM in their analysis of thermal pressures from C I fine-structure excitation. (Many of the same sight lines studied in that paper are included in our analysis.) From Figure 20, we find that values of $f_1(\text{H}_2)$ as high as 0.6 are generally only seen along sight lines with relatively high molecular hydrogen column densities (i.e., $\log N(\text{H}_2) \gtrsim 20.5$), and these sight lines represent only $\sim 13\%$ of the sample.

6. SUMMARY AND CONCLUSIONS

We have presented a comprehensive examination of interstellar P II and Cl I abundances based on an analysis of archival HST/STIS and FUSE spectra. Column densities of P II, Cl I, and Cl II were derived through detailed profile synthesis fits for a combined sample of over 100 sight lines. P II column densities were obtained from the weak P II $\lambda 1532$ line wherever possible. Measurements of P II $\lambda 1301$ were included only in cases where there was no significant blending with O I $\lambda 1302$. Cl I column densities were derived through simultaneous fits to the Cl I $\lambda 1347$ line (from STIS spectra) and either the $\lambda 1379$ line or the $\lambda 1097$, $\lambda 1094$, or $\lambda 1004$ transition (from FUSE data). Cl II column densities were obtained from the Cl II $\lambda 1071$ transition, after fitting and removing absorption from a nearby H_2 feature.

Experimentally determined oscillator strengths were used for most of the P II, Cl I, and Cl II lines included in our analysis (Table 2). However, since no recent experimental f -value is available for the P II $\lambda 1532$ transition, an empirical f -value was determined from the data for thirteen sight lines that have high-resolution STIS spectra covering both P II $\lambda 1301$ and P II $\lambda 1532$. Our empirical f -value for the $\lambda 1532$ transition, $f(1532) = 0.00737$, is very similar to the results of recent theoretical calculations (Tayal 2003; Froese Fischer et al. 2006). These theoretical results and our empirical determination indicate that a downward revision of ~ 0.4 dex is required for P II column densities obtained using the f -value for P II $\lambda 1532$ reported in Morton (2003).

We reexamined the relationships between various Cl and H species, finding significant correlations between $N(\text{Cl I})$ and $N(\text{H}_2)$ and between $N(\text{Cl}_{\text{tot}})$ and $N(\text{H}_{\text{tot}})$. The generally good correlation between Cl I and H_2 results from the neutralization of chlorine ions in regions where H_2 is abundant. The tight linear relationship between the total column densities of Cl and H indicates that the abundance and/or depletion of Cl does not vary appreciably with $N(\text{H}_{\text{tot}})$. While the relationships we

find are similar to those presented in previous investigations (e.g., [Harris & Bromage 1984](#); [Moomey et al. 2012](#)), our results apply to a much larger, more representative sample of interstellar sight lines.

We derived depletion parameters for P and Cl in accordance with the methodology of [Jenkins \(2009\)](#). For P, we find that the depletion slope is somewhat shallower than that reported in [Jenkins \(2009\)](#). This difference may be a result of our much larger sample or it may be related to our use of weak, unblended P II transitions (from high quality STIS observations). For Cl, we find that the depletion slope is much shallower compared to the slope obtained by [Jenkins \(2009\)](#). In this case, the difference in slope is almost entirely due to our inclusion of Cl I column densities in determinations of total Cl abundances. A major improvement over the [Jenkins \(2009\)](#) results is that the initial depletions of P and Cl no longer indicate that the abundances of these elements are supersolar at $F_* = 0$. In large part, this is due to improved oscillator strengths for the relevant P II (and Cl I) transitions.

In general, we find that Cl is only lightly depleted along most interstellar sight lines, regardless of the fraction of hydrogen in molecular form (or the fraction of Cl in neutral form). Indeed, the existence of a *negative* depletion slope for Cl appears to be dependent on an enhanced rate of depletion for a subset of sight lines with anomalously low Cl I abundances and higher-than-expected Cl II abundances. Many of these sight lines probe PDR-like regions where the flux of UV radiation is likely to be enhanced. The implication is that an elevated level of ionization in relatively dense gas leads to an enhanced rate of accretion of the ions onto grain surfaces. This, in turn, implies the existence of a population of small, negatively-charged grains, which accrete ionized species more efficiently through Coulomb interactions. We take this as concrete evidence of the growth of dust grains in diffuse interstellar clouds.

From an analysis of neutral chlorine fractions, we obtained estimates for the molecular hydrogen fractions that pertain to the H₂-bearing gas along the lines of sight in our survey. We find that for all sight lines with $\log N(\text{H}_2) \gtrsim 18$ (where H₂ transitions to being fully self shielded), the H₂-bearing gas has a molecular fraction of at least 10% and that the gas becomes essentially fully molecular at $\log N(\text{H}_2) \approx 21$. A typical value of the molecular fraction in the H₂-bearing portion of a diffuse cloud is 0.4. This might then be adopted as a representative value for the CNM in general for studies seeking to analyze the chemistry and physical conditions in diffuse molecular clouds.

We acknowledge the efforts of undergraduate students Jennifer Hobbs and Luke Russell, who performed a preliminary analysis of Cl abundances as part of the Pre-Major in Astronomy Program (Pre-MAP) at the University of Washington. The profile fitting routine used in this work (ISMODO), which was originally created by Yaron Sheffer, was updated by Johnathan Rice to accommodate simultaneous fits to multiple absorption features. We thank Dan Welty for providing us with the H2GUI package. Our research has made use of the SIMBAD database operated at CDS, Strasbourg, France. Support for this work was provided by the Space Telescope Science Institute through grants HST-AR-15807.001-A to Eureka Scientific and HST-AR-15807.002-A to the University of Toledo. Observations were obtained from the MAST data archive at the Space Telescope Science Institute. The specific observations analyzed can be accessed via the following DOI: [10.17909/qfnj-yt76](https://doi.org/10.17909/qfnj-yt76). STScI is operated by the Association of Universities for Research in Astronomy, Inc., under NASA contract NAS5-26555.

Facilities: HST(STIS), FUSE, Copernicus

Software: ISMOD ([Sheffer et al. 2008](#)), STSDAS, H2GUI ([Tumlinson et al. 2002](#)), LTOOLS

APPENDIX

A. CHLORINE MEASUREMENTS FROM COPERNICUS OBSERVATIONS

To supplement our sample of Cl measurements from STIS and FUSE observations, we have included in our analysis additional Cl abundance determinations based on observations made with the Copernicus satellite. The Copernicus sample consists of the results presented in [Moomey et al. \(2012\)](#), who studied sight lines probing the transition from atomic to molecular gas, and the results obtained by [Brown \(2015\)](#), who focused on sight lines with very low H₂ column densities as part of a Masters Thesis at the University of Toledo. [Brown \(2015\)](#) derived Cl I and Cl II column densities via ISMOD fits to the Cl I $\lambda 1088$, Cl I $\lambda 1347$, and Cl II $\lambda 1071$ lines, adopting component structures from high-resolution ground-based observations of K I, Ca II K, and Na I D. A detailed comparison between the Cl I and Cl II column densities derived by [Brown \(2015\)](#) and those obtained in previous Copernicus studies of the same sight lines ([Jura & York 1978](#); [Harris & Bromage 1984](#); [Jenkins et al. 1986](#)) is presented in [Brown \(2015\)](#). In general, the [Brown \(2015\)](#) results agree with those of the previous studies within the mutual uncertainties, although the uncertainties in

Brown (2015) tend to be smaller.¹⁰ For convenience, the results on $N(\text{Cl I})$ and $N(\text{Cl II})$ from both Moomey et al. (2012) and Brown (2015) are provided in Table 10. Column densities of H I and H₂ for the Copernicus sight lines, along with the sight line depletion factors, are obtained from Jenkins (2009), except in the case of 67 Oph, which is not included in Jenkins (2009). For this sight line, H I and H₂ column densities are obtained from Savage et al. (1977) and Bohlin et al. (1978). Values of $N(\text{Cl}_{\text{tot}})$ are listed in Table 10 even in cases where Cl I is not detected, provided that the upper limit on $N(\text{Cl I})$ is low enough that Cl I will not contribute meaningfully to the total Cl column density. The same is true for values of $N(\text{H}_{\text{tot}})$ in cases where H₂ is not detected.

Table 10. Chlorine Column Densities from Copernicus Observations

Star	Name	$\log N(\text{Cl I})$	$\log N(\text{Cl II})$	$\log N(\text{Cl}_{\text{tot}})$	Ref.	$\log N(\text{H I})^{\text{a}}$	$\log N(\text{H}_2)^{\text{a}}$	$\log N(\text{H}_{\text{tot}})$	F_*^{a}
HD 5394	γ Cas	12.20 ± 0.06	13.19 ± 0.09	13.24 ± 0.08	1	20.16 ± 0.08	16.53 ± 0.05	$20.16^{+0.08}_{-0.10}$	0.52 ± 0.04
HD 23408	20 Tau	13.54 ± 0.09	< 13.15	...	2	...	19.75 ± 0.26
HD 23630	η Tau	13.53 ± 0.07	< 13.18	...	2	...	19.54 ± 0.18
HD 24760	ϵ Per	13.04 ± 0.04	13.28 ± 0.10	13.48 ± 0.07	2	20.40 ± 0.08	19.52 ± 0.26	$20.50^{+0.09}_{-0.12}$	0.68 ± 0.04
HD 30614	α Cam	14.11 ± 0.03	< 13.40	...	2	20.90 ± 0.08	20.34 ± 0.15	$21.09^{+0.08}_{-0.09}$	0.46 ± 0.04
HD 35715	ψ Ori	12.05 ± 0.12	13.69 ± 0.08	13.70 ± 0.08	1	20.49 ± 0.15	14.78 ± 0.15	$20.49^{+0.15}_{-0.23}$	0.66 ± 0.11
HD 36486	δ Ori	< 11.41	13.31 ± 0.01	13.31 ± 0.01	1	20.19 ± 0.04	14.68 ± 0.26	$20.19^{+0.04}_{-0.04}$	0.54 ± 0.02
HD 36861	λ Ori	13.28 ± 0.04	13.67 ± 0.08	13.82 ± 0.06	2	20.78 ± 0.10	19.12 ± 0.20	$20.80^{+0.10}_{-0.12}$	0.57 ± 0.04
HD 37043	ι Ori	< 11.40	13.16 ± 0.04	13.16 ± 0.04	1	20.15 ± 0.06	14.69 ± 0.20	$20.15^{+0.06}_{-0.07}$	0.41 ± 0.03
HD 37128	ϵ Ori	12.09 ± 0.01	13.39 ± 0.03	13.41 ± 0.03	1	20.45 ± 0.08	16.57 ± 0.20	$20.45^{+0.08}_{-0.10}$	0.54 ± 0.03
HD 37468	σ Ori	12.60 ± 0.06	13.67 ± 0.05	13.71 ± 0.05	1	20.52 ± 0.08	< 18.30	$20.52^{+0.08}_{-0.10}$	0.58 ± 0.04
HD 38771	κ Ori	12.29 ± 0.04	13.49 ± 0.01	13.52 ± 0.01	1	20.52 ± 0.04	15.68 ± 0.20	$20.52^{+0.04}_{-0.04}$	0.67 ± 0.03
HD 40111	139 Tau	13.18 ± 0.03	13.87 ± 0.11	13.95 ± 0.09	2	20.90 ± 0.08	19.73 ± 0.20	$20.96^{+0.08}_{-0.09}$	0.49 ± 0.04
HD 57060	29 CMa	< 13.00	13.22 ± 0.09	...	1	20.70 ± 0.08	15.78 ± 0.18	$20.70^{+0.08}_{-0.10}$	0.50 ± 0.05
HD 57061	τ CMa	< 12.00	13.91 ± 0.06	13.91 ± 0.06	1	20.70 ± 0.04	15.48 ± 0.18	$20.70^{+0.04}_{-0.04}$	0.39 ± 0.04
HD 64740	...	< 12.30	13.93 ± 0.07	13.93 ± 0.07	1	20.05 ± 0.18	< 14.95	$20.05^{+0.18}_{-0.31}$	0.27 ± 0.30
HD 64760	...	< 11.89	13.57 ± 0.04	13.57 ± 0.04	1	20.26 ± 0.09	< 14.60	$20.26^{+0.09}_{-0.11}$	0.35 ± 0.06
HD 65575	χ Car	< 12.28	13.52 ± 0.05	13.52 ± 0.05	1	< 20.74	< 14.78
HD 65818	ν Pup	< 12.54	13.92 ± 0.09	13.92 ± 0.09	1	20.52 ± 0.13	15.08 ± 0.30	$20.52^{+0.13}_{-0.19}$	0.36 ± 0.09
HD 106490	δ Cru	< 11.95	13.31 ± 0.07	13.31 ± 0.07	1	< 19.69	< 14.08
HD 108248	α^1 Cru	< 11.38	12.94 ± 0.03	12.94 ± 0.03	1	19.60 ± 0.10	< 14.18	$19.60^{+0.10}_{-0.13}$	0.15 ± 0.05
HD 118716	ϵ Cen	< 11.54	12.95 ± 0.03	12.95 ± 0.03	1	19.60 ± 0.19	< 14.08	$19.60^{+0.19}_{-0.35}$	0.15 ± 0.16
HD 127972	η Cen	< 11.67	13.21 ± 0.20	13.21 ± 0.20	1	< 19.48	< 14.18
HD 136298	δ Lup	< 11.81	13.11 ± 0.07	13.11 ± 0.07	1	< 19.76	< 14.26
HD 141637	1 Sco	13.00 ± 0.04	13.88 ± 0.17	13.93 ± 0.16	2	21.12 ± 0.10	19.23 ± 0.18	$21.13^{+0.10}_{-0.13}$	0.69 ± 0.05
HD 143018	π Sco	12.85 ± 0.02	13.69 ± 0.12	13.75 ± 0.10	2	20.65 ± 0.06	19.32 ± 0.20	$20.69^{+0.06}_{-0.07}$	0.71 ± 0.03
HD 143118	η Lup	12.03 ± 0.10	12.85 ± 0.14	12.91 ± 0.13	1	< 20.12	< 14.23
HD 143275	δ Sco	13.57 ± 0.02	14.00 ± 0.01	14.13 ± 0.01	2	21.15 ± 0.08	19.41 ± 0.20	$21.17^{+0.08}_{-0.09}$	0.90 ± 0.03
HD 144217	β^1 Sco	13.81 ± 0.01	13.92 ± 0.01	14.17 ± 0.01	2	21.09 ± 0.04	19.83 ± 0.06	$21.14^{+0.04}_{-0.04}$	0.81 ± 0.02
HD 144470	ω^1 Sco	13.62 ± 0.03	14.20 ± 0.10	14.31 ± 0.08	2	21.17 ± 0.08	20.05 ± 0.11	$21.23^{+0.07}_{-0.09}$	0.81 ± 0.04

Table 10 continued

¹⁰ For further details, see Brown (2015), available at the following URL: http://rave.ohiolink.edu/etdc/view?acc_num=toledo1431040914.

Table 10 (*continued*)

Star	Name	$\log N(\text{Cl I})$	$\log N(\text{Cl II})$	$\log N(\text{Cl}_{\text{tot}})$	Ref.	$\log N(\text{H I})^a$	$\log N(\text{H}_2)^a$	$\log N(\text{H}_{\text{tot}})$	F_*^a
HD 145502	ν Sco	13.30 ± 0.04	< 13.00	...	2	21.07 ± 0.17	19.89 ± 0.15	$21.12^{+0.15}_{-0.24}$	0.80 ± 0.11
HD 147165	σ Sco	13.28 ± 0.02	14.40 ± 0.08	14.43 ± 0.07	2	21.34 ± 0.15	19.79 ± 0.15	$21.36^{+0.14}_{-0.22}$	0.76 ± 0.06
HD 148184	χ Oph	14.26 ± 0.02	13.62 ± 0.08	14.35 ± 0.03	2	21.07 ± 0.10	20.63 ± 0.18	$21.31^{+0.10}_{-0.13}$	0.96 ± 0.09
HD 149038	μ Nor	14.23 ± 0.02	13.79 ± 0.13	14.37 ± 0.04	2	21.00 ± 0.08	20.45 ± 0.15	$21.19^{+0.08}_{-0.10}$	0.56 ± 0.05
HD 151890	μ^1 Sco	< 11.78	13.20 ± 0.06	13.20 ± 0.06	1	< 20.12	< 14.26
HD 157246	γ Ara	12.95 ± 0.02	13.96 ± 0.04	14.00 ± 0.04	2	20.68 ± 0.08	19.23 ± 0.23	$20.71^{+0.08}_{-0.09}$	0.46 ± 0.03
HD 160578	κ Sco	< 11.53	13.05 ± 0.05	13.05 ± 0.05	1	20.22 ± 0.12	< 14.23	$20.22^{+0.12}_{-0.17}$	0.50 ± 0.07
HD 164353	67 Oph	13.53 ± 0.06	2	21.00 ± 0.15	20.26 ± 0.28	$21.13^{+0.14}_{-0.21}$...
HD 200120	59 Cyg	12.70 ± 0.09	< 13.40	...	2	< 20.07	19.30 ± 0.18
HD 217675	o And	13.18 ± 0.03	2	...	19.67 ± 0.18
HD 218376	1 Cas	13.98 ± 0.10	< 13.73	...	2	20.95 ± 0.12	20.15 ± 0.18	$21.07^{+0.10}_{-0.14}$	0.60 ± 0.06

^aAtomic and molecular hydrogen column densities and sight line depletion factors are obtained from Jenkins (2009), except in the case of 67 Oph. For this sight line, H I and H₂ column densities are from Savage et al. (1977) and Bohlin et al. (1978).

References—(1) Brown (2015), (2) Mooney et al. (2012).

B. FLUORINE DEPLETIONS FROM THE LITERATURE

Fluorine abundances were reported by Federman et al. (2005) and Snow et al. (2007) from analyses of the F I lines at 951 and 954 Å in FUSE spectra. However, fluorine was not included in the depletion study of Jenkins (2009) (presumably because there are relatively few published detections). From a thermochemical perspective, fluorine is very similar to chlorine. (For example, like Cl⁺, F reacts exothermically with H₂; Neufeld & Wolfire 2009). Moreover, the depletions of F and Cl are often assumed to be similar (e.g., Federman et al. 2005). Thus, in order to compare the depletion behaviors of F and Cl in a more quantitative way, we derived depletion parameters for F using the Jenkins (2009) methodol-

ogy. In Figure 21, we plot the gas-phase F abundances from Federman et al. (2005) and Snow et al. (2007) as a function of the sight line depletion factors from Jenkins (2009). (Note that Federman et al. (2005) incorporate a measurement of F I absorption toward δ Sco into their analysis. This measurement was originally obtained by Snow & York (1981) based on Copernicus observations.) A least-squares linear fit yields the following parameters: $A_F = -0.304 \pm 0.288$, $B_F = -0.213 \pm 0.077$, $z_F = 0.483$, $[\text{F}/\text{H}]_0 = -0.066 \pm 0.159$, and $[\text{F}/\text{H}]_1 = -0.370 \pm 0.167$. The χ^2 statistic is 13.6 with 7 degrees of freedom, yielding a reduced chi-squared value of 1.9. From these results, we find that the initial depletion of F is consistent with zero (as expected), and the depletion slope for F is very similar to that for Cl. The depletion results for F derived here are compared to those for many other elements in Figure 19.

REFERENCES

- Alkhayat, R. B., Irving, R. E., Federman, S. R., Ellis, D. G., & Cheng, S. 2019, *ApJ*, 887, 14
- Bailer-Jones, C. A. L., Rybizki, J., Fousneau, M., Demleitner, M., & Andrae, R. 2021, *AJ*, 161, 147
- Balashev, S. A., Noterdaeme, P., Klimenko, V. V., et al. 2015, *A&A*, 575, L8
- Blair, W. P., Ghavamian, P., Long, K. S., et al. 2007, *ApJ*, 662, 998
- Bohlin, R. C., Hill, J. K., Jenkins, E. B., et al. 1983, *ApJS*, 51, 277
- Bohlin, R. C., Savage, B. D., & Drake, J. F. 1978, *ApJ*, 224, 132
- Brown, J. M. 2015, M.S. Thesis, Univ. Toledo
- Brown, M. S., Alkhayat, R. B., Irving, R. E., et al. 2018, *ApJ*, 868, 42
- Brown, M. S., Federman, S. R., Irving, R. E., Cheng, S., & Curtis, L. J. 2009, *ApJ*, 702, 880
- Cartledge, S. I. B., Lauroesch, J. T., Meyer, D. M., & Sofia, U. J. 2004, *ApJ*, 613, 1037
- Cartledge, S. I. B., Lauroesch, J. T., Meyer, D. M., & Sofia, U. J. 2006, *ApJ*, 641, 327
- Cartledge, S. I. B., Meyer, D. M., Lauroesch, J. T., & Sofia, U. J. 2001, *ApJ*, 562, 394

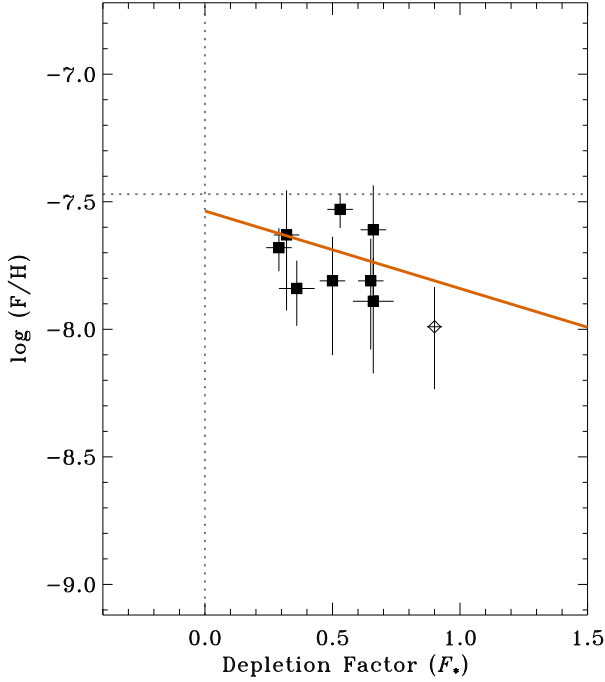


Figure 21. Gas-phase F abundances from the literature (Federman et al. 2005; Snow et al. 2007) as a function of the sight line depletion factor (F_*). Solid squares represent abundances derived from FUSE observations; the open diamond represents the F abundance toward δ Sco, which is based on Copernicus observations (Snow & York 1981; Federman et al. 2005). The solid orange line represents a linear fit to the data derived according to the methodology of Jenkins (2009). The horizontal dotted line gives the adopted solar system abundance from Lodders (2003).

Dwek, E. 2016, *ApJ*, 825, 136
Dwek, E., & Scalzo, J. M. 1980, *ApJ*, 239, 193
Federman, S. R., Brown, M., Torok, S., et al. 2007, *ApJ*, 660, 919
Federman, S. R., Sheffer, Y., Lambert, D. L., & Smith, V. V. 2005, *ApJ*, 619, 884
Froese Fischer, C., Tachiev, G., & Irimia, A. 2006, *ADNDT*, 92, 607
Gail, H.-P., Wetzell, S., Pucci, A., & Tamanai, A. 2013, *A&A*, 555, A119
Gobrecht, D., Cherchneff, I., Sarangi, A., Plane, J. M. C., & Bromley, S. T. 2016, *A&A*, 585, A6
Harris, A. W., & Bromage, G. E. 1984, *MNRAS*, 208, 941
Hibbert, A. 1988, *PhyS*, 38, 37
Hobbs, L. M. 1974, *ApJ*, 188, L107
Jenkins, E. B. 2009, *ApJ*, 700, 1299
Jenkins, E. B. 2019, *ApJ*, 872, 55
Jenkins, E. B., Savage, B. D., & Spitzer, L. 1986, *ApJ*, 301, 355
Jenkins, E. B., & Tripp, T. M. 2011, *ApJ*, 734, 65

Jensen, A. G., & Snow, T. P. 2007a, *ApJ*, 669, 378
Jensen, A. G., & Snow, T. P. 2007b, *ApJ*, 669, 401
Jones, A. P., Kohler, M., Ysard, N., Bocchio, M., & Verstraete, L. 2017, *A&A*, 602, A46
Jones, A. P., Tielens, A. G. G. M., Hollenbach, D. J., & McKee, C. F. 1994, *ApJ*, 433, 797
Jura, M. 1974, *ApJ*, 190, L33
Jura, M., & York, D. G. 1978, *ApJ*, 219, 861
Karovicova, I., Wittkowski, M., Ohnaka, K., et al. 2013, *A&A*, 560, A75
Lebouteiller, V., Kuassivi, & Ferlet, R. 2005, *A&A*, 443, 509
Lodders, K. 2003, *ApJ*, 591, 1220
Lodders, K., & Fegley, Jr., B. 2023, submitted to *Geochemistry* [arXiv:2301.03674]
Moomey, D., Federman, S. R., & Sheffer, Y. 2012, *ApJ*, 744, 174
Morton, D. C. 2003, *ApJS*, 149, 205
Neufeld, D. A., & Wolfire, M. G. 2009, *ApJ*, 706, 1594
Oliver, P., & Hibbert, A. 2013, *ADNDT*, 99, 459
Paquette, J. A., Ferguson, F. T., & Nuth, J. A. 2011, *ApJ*, 732, 62
Press, W. H., Teukolsky, S. A., Vetterling, W. T., & Flannery, B. P. 2007, *Numerical Recipes, The Art of Scientific Computing* (3rd ed.; Cambridge: Cambridge Univ. Press)
Priestley, F. D., De Looze, I., & Barlow, M. J. 2021, *MNRAS*, 502, 2438
Rachford, B. L., Snow, T. P., Destree, J. D., et al. 2009, *ApJS*, 180, 125
Rachford, B. L., Snow, T. P., Tumlinson, J., et al. 2002, *ApJ*, 577, 221
Ritchey, A. M., Federman, S. R., & Lambert, D. L. 2018, *ApJS*, 236, 36
Ritchey, A. M., Federman, S. R., Sheffer, Y., & Lambert, D. L. 2011, *ApJ*, 728, 70
Ritchey, A. M., Jenkins, E. B., Shull, J. M., et al. 2023, submitted to *ApJ* [arXiv:2301.09743]
Sarangi, A., & Cherchneff, I. 2015, *A&A*, 575, A95
Savage, B. D., Bohlin, R. C., Drake, J. F., & Budich, W. 1977, *ApJ*, 216, 291
Savage, B. D., & Sembach, K. R. 1991, *ApJ*, 379, 245
Schechtman, R. M., Federman, S. R., Beideck, D. J., & Ellis, D. J. 1993, *ApJ*, 406, 735
Schechtman, R. M., Federman, S. R., Brown, M., et al. 2005, *ApJ*, 621, 1159
Sheffer, Y., Rogers, M., Federman, S. R., et al. 2008, *ApJ*, 687, 1075
Slavin, J. D., Dwek, E., & Jones, A. P. 2015, *ApJ*, 803, 7
Snow, T. P., Destree, J. D., & Jensen, A. G. 2007, *ApJ*, 655, 285

- Snow, T. P., Destree, J. D., & Welty, D. E. 2008, *ApJ*, 679, 512
- Snow, T. P., & York, D. G. 1981, *ApJ*, 247, L39
- Sonnentrucker, P., Friedman, S. D., Welty, D. E., York, D. G., & Snow, T. P. 2002, *ApJ*, 576, 241
- Sonnentrucker, P., Friedman, S. D., & York, D. G. 2006, *ApJ*, 650, L115
- Sonnentrucker, P., Welty, D. E., Thorburn, J. A., & York, D. G. 2007, *ApJS*, 168, 58
- Tayal, S. S. 2003, *ApJS*, 146, 459
- Toner, A., & Hibbert, A. 2005, *MNRAS*, 361, 673
- Tumlinson, J., Shull, J. M., Rachford, B. L., et al. 2002, *ApJ*, 566, 857
- Valencic, L. A., Clayton, G. C., & Gordon, K. D. 2004, *ApJ*, 616, 912
- van Dishoeck, E. F., & Black, J. H. 1988, *ApJ*, 334, 771
- Weingartner, J. C., & Draine, B. T. 1999, *ApJ*, 517, 292
- Welty, D. E., & Crowther, P. A. 2010, *MNRAS*, 404, 1321
- Welty, D. E., & Hobbs, L. M. 2001, *ApJS*, 133, 345
- Welty, D. E., Sonnentrucker, P., Snow, T. P., & York, D. G. 2020, *ApJ*, 897, 36
- Zhukovska, S., Dobbs, C., Jenkins, E. B., & Klessen, R. S. 2016, *ApJ*, 831, 147
- Zhukovska, S., Henning, T., & Dobbs, C. 2018, *ApJ*, 857, 94